

Copyright

by

Kenji Furui

2004

**The Dissertation Committee for Kenji Furui
certifies that this is the approved version of the following dissertation:**

**A COMPREHENSIVE SKIN FACTOR MODEL FOR WELL COMPLETIONS
BASED ON FINITE ELEMENT SIMULATIONS**

Committee:

A. Daniel Hill, Supervisor

Ding Zhu

Kamy Sepehrnoori

Mary F. Wheeler

Michael J. Economides

Mukul M. Sharma

**A COMPREHENSIVE SKIN FACTOR MODEL FOR WELL COMPLETIONS
BASED ON FINITE ELEMENT SIMULATIONS**

by

Kenji Furui, B.S., M.S.

Dissertation

Presented to the Faculty of the Graduate School of

the University of Texas at Austin

in Partial Fulfillment

of the Requirements

for the Degree of

Doctor of Philosophy

The University of Texas at Austin

May, 2004

UMI Number: 3143749



UMI Microform 3143749

Copyright 2003 by ProQuest Information and Learning Company.

All rights reserved. This microform edition is protected against
unauthorized copying under Title 17, United States Code.

ProQuest Information and Learning Company
300 North Zeeb Road
PO Box 1346
Ann Arbor, MI 48106-1346

Dedication

This dissertation is gratefully dedicated to my parents, Shingo and Sayo, my brother, Akio, and my wife, Ayako. Without their continuous support and love, my work would never have been completed.

Acknowledgements

I would like to express my acknowledgements to my supervisor Dr. A. D. Hill and Dr. D. Zhu. They offered me great help and I will always remember their kindness. Thanks also go to Improved Well Performance (IWP) research program provided by the Center for Petroleum & Geosystems Engineering at the University of Texas at Austin, for providing the financial support for this study.

A COMPREHENSIVE SKIN FACTOR MODEL FOR WELL COMPLETIONS BASED ON FINITE ELEMENT SIMULATIONS

Publication No. _____

Kenji Furui, Ph.D.

The University of Texas at Austin, 2004

Supervisor: Alfred Daniel Hill

The additional pressure drop caused by the well completion can strongly affect the overall well performance in production and/or injection wells. Particularly in horizontal wells, where the reservoir pressure drop is low, any pressure drop through the completion can be critical. A comprehensive completion model is developed to describe the pressure and flow rate relationship (inflow performance) for different types of completions, focusing on behavior in horizontal laterals. The completion types include slotted liners, cased/perforated completions, screens, gravel packs, and pre-packed screens. Because of the complex flow geometry in the near wellbore region, finite element modeling is the most efficient means of simulating the completion inflow performance. A 2-D and 3-D finite element simulator is developed to estimate the inflow performance. The study also considers the effect of scale (precipitated solids) on the performance of screens or slotted liners and the effect of damage on a gravel pack. Based on the simulation results, semi-analytical completion inflow models are derived as skin factor models so that they can be easily coupled with reservoir inflow models. It is expected that in most cases, this will be a rate-dependent skin factor, similar to the way non-Darcy flow is represented in reservoir inflow models.

Table of Contents

Acknowledgments	v
Abstract	vi
List of Tables	ix
List of Figures	x
Chapter 1: Introduction.....	1
1.1 Background.....	1
1.2 Literature Reviews	2
1.3 Objective and Approach.....	4
1.4 Finite Element Simulator	6
Chapter 2: Near Wellbore Flow through Porous Medium and Skin Factor	8
2.1 Differential Equation for Fluid Flow through Porous Medium.....	8
2.2 Diffusivity Equation.....	10
2.3 Non-Darcy Flow	11
2.4 General Form of a Skin Equation	13
Chapter 3: Openhole Completions	19
3.1 Introduction to Openhole Completions.....	19
3.2 Development of a Skin Equation for Openhole Completions	19
3.3 Effect of Formation Damage on Openhole Completions.....	20
Chapter 4: Slotted or Perforated Liners.....	25
4.1 Introduction to Slotted or Perforated Liners.....	25
4.2 Development of a Skin Equation for Slotted Liners	25
4.3 Development of a Skin Equation for Perforated Liners.....	35
4.4 Effect of Formation Damage on Slotted or Perforated Liners	38
Chapter 5: Cased and Perforated Wells.....	48
5.1 Introduction to Cased and Perforated Wells.....	48
5.2 Development of a Skin Equation for Cased and Perforated Wells.....	48
5.3 Effect of Formation Damage on Cased and Perforated Wells	59
5.4 Effect of Crushed Zone due to Perforating Jet	64

Chapter 6: Gravel Pack Completions	83
6.1 Introduction to Gravel Pack Completions	83
6.2 Development of a Skin Equation for Openhole Gravel Packed Wells	84
6.3 Development of a Skin Equation for Cased Hole Gravel Packed Wells	85
Chapter 7: Guidelines for Horizontal Well Completions – Application of the Skin Factor Models	94
7.1 Slotted (Perforated) Liner Optimization	94
7.2 Perforating Horizontal Wells	95
7.3 Minimizing Formation Damage Effect for Perforated Wells	96
7.4 Minimizing Crushed Zone Effect for Perforated Wells	97
7.5 Diagnosis of Formation Damage Effect on Well Completions	98
Chapter 8: Conclusion	109
Appendix A: Finite Element Simulator	111
A.1 Finite Element Formulation	111
A.2 Element and Element Matrix Construction	116
A.3 Solution Procedure	126
A.4 Verification of the FEM Simulator	127
Appendix B: GiD Files	137
B.1 Interaction of GiD with IWPCOMPS	137
B.2 Materials File	138
B.3 General File	138
B.4 Conditions File	139
B.5 Data Format File	140
B.6 Execution File for the Problem Type	142
Appendix C: Example Skin Calculations	149
Nomenclature	157
Bibliography	164
Vita	169

List of Tables

Table 2.1: Summary of existing correlations for high-velocity flow.....	17
Table 3.1: Numerical data for Fig. 3.2.	23
Table 4.1: Numerical data for Fig. 4.12.	41
Table 5.1: Correlation constant, a_m	68
Table 5.2: Correlation constants, b_m and c_m	68
Table 5.3: Correlation constants, d_m , e_m , f_m and g_m	68
Table 5.4: Numerical data for Fig. 5.13.	69
Table 5.5: Comparison with FEM simulation results ($f_{t,p}$).....	69
Table 5.6: Simulation conditions for Fig. 5.21.	70
Table 5.7: Simulation conditions for Fig. 5.23.	70
Table 7.1: Data for slotted liner study.....	100
Table 7.2: Data for perforated liner study.	100
Table C.1: Data for the example problem.	156

List of Figures

Figure 2.1: An arbitrary macroscopic control volume.	18
Figure 2.2: Flowpaths for actual and ideal conditions.	18
Figure 3.1: Vertical section of a open hole well with formation damage.	24
Figure 3.2: Comparison with FEM simulation results, openhole completions.....	24
Figure 4.1: Geometric variables for slotted liner skin calculation.	42
Figure 4.2: 2D pressure contour fill of single inline slotted liners.....	42
Figure 4.3: Determination of the outer radius of slot-induced radial flow.....	43
Figure 4.4: 3D pressure contour lines of a single inline slotted liner.....	43
Figure 4.5: Approximation of the axial flow convergence.....	44
Figure 4.6: Flow geometries around a slotted liner.....	44
Figure 4.7: Pressure contour fill of slots filled by formation sand.....	45
Figure 4.8: Comparison with FEM results, single staggered slotted liners.....	45
Figure 4.9: Slotted liner skin factors in anisotropic formation.	46
Figure 4.10: 3D pressure contour lines of a perforated liner.....	46
Figure 4.11: Cross section of a liner inside a damage zone.....	47
Figure 4.12: Verification of the assumption used in Eq. 4.75.	47
Figure 5.1: Geometry of a perforated horizontal well.....	71
Figure 5.2: Effective well radius.....	71
Figure 5.3: 2D plane flow skin factor in an isotropic medium.	72
Figure 5.4: Effect of perforation orientation on s_{2D}	72
Figure 5.5: Comparison with FEM simulation database for $m_p=2$	73
Figure 5.6: Concept of wellbore blockage effect.....	73
Figure 5.7: Wellbore blockage effect in an isotropic formation.....	74

Figure 5.8: Effect of perforation orientation on s_{wb}	74
Figure 5.9: Wellbore blockage effect in anisotropic formations ($m_p=1$).	75
Figure 5.10: Wellbore blockage effect in anisotropic formations ($m_p=2$).	75
Figure 5.11: Details of the perforation in the equivalent isotropic system.....	76
Figure 5.12: Simplified flow geometry for perforated horizontal wells.	76
Figure 5.13: The effect of turbulence on perforation phasings.....	77
Figure 5.14: Perforated well with deep penetration of damage.	77
Figure 5.15: 2D pressure contour fill of perforated wells (Pseudoskin, s_x).	78
Figure 5.16: Dimensionless off-centered perforation position, r_{dc}	78
Figure 5.17: Determination of the dimensionless off-centered perforation position	79
Figure 5.18: Perforated well with shallow penetration of damage.	79
Figure 5.19: Comparison of formation damage skin with FEM simulation ($k_H/k_V=1$)...80	
Figure 5.20: Comparison of formation damage skin with FEM simulation ($k_H/k_V=4$)...80	
Figure 5.21: Verification of the perforation skin model.....	81
Figure 5.22: Crushed zone around a perforation.....	81
Figure 5.23: Verification of the perforation skin model with crushed zone.....	82
Figure 6.1: Gravel pack completions.	89
Figure 6.2: Mathematical representation of open hole gravel packed wells.	89
Figure 6.3: Mathematical representation of cased and gravel packed wells.	90
Figure 6.4: FEM simulation result for a low permeability reservoir.	90
Figure 6.5: FEM simulation result for a high permeability reservoir.	91
Figure 6.6: Pressure profile of cased and gravel packed wells.	91
Figure 6.7: Determination of the interpolation constant for the gravel pack model.....	92
Figure 6.8: Comparison and verification of the gravel pack skin model.	92
Figure 6.9: Simulation conditions for Fig. 6.8.....	93

Figure 7.1: Skin factor analysis of slotted liners (open slots).....	101
Figure 7.2: Skin factor analysis of perforated liners.	101
Figure 7.3: Skin factor analysis of slotted liners (plugged slots).....	102
Figure 7.4: Skin factor summary for liner completions.	103
Figure 7.5: Effect of perforation orientation on perforation skin factor.	104
Figure 7.6: Guidelines for perforating horizontal wells.	105
Figure 7.7: Guidelines for minimizing formation damage effect.	106
Figure 7.8: Guidelines for minimizing crushed zone effect.	107
Figure 7.9: Effect of formation damage on different well completions.	108
Figure 7.10: Diagnosis of Formation Damage Effect.	108
Figure A.1: Finite element discretization of a domain.	129
Figure A.2: Definition of area coordinates L_i used for triangular elements.	129
Figure A.3: Linear and quadratic rectangular elements.	130
Figure A.4: Linear and quadratic tetrahedral elements.	130
Figure A.5: Linear and quadratic brick elements.....	131
Figure A.6: Surface fluxes computations.	131
Figure A.7: Program flow of the FEM simulation (IWPCOMPS).	132
Figure A.8: 2D radial flow problem.....	133
Figure A.9: Element mesh plot, radial flow problem.....	133
Figure A.10: Pressure contour fill plot, radial flow problem	134
Figure A.11: Comparison with analytical solutions, radial flow problem	134
Figure A.12: 3D spherical flow problem.....	135
Figure A.13: Element mesh plot, spherical flow problem.....	135
Figure A.14: Pressure contour fill plot, spherical flow problem	136
Figure A.15: Comparison with analytical solutions, spherical flow problem	136

Figure B.1: GiD customization.	143
Figure B.2: Diagram of GiD file configurations.....	143
Figure B.3: GiD materials file.	144
Figure B.4: GiD general file.	145
Figure B.5: GiD conditions file.....	146
Figure B.6: GiD data format file.....	147
Figure B.7: Calculate option in GiD interface.....	148
Figure B.8: GiD execution file.....	148

CHAPTER 1

Introduction

1.1 BACKGROUND

Horizontal wells have become an important completion technology for oil and gas recovery. They have proven to be excellent producers for thin reservoirs or for thicker reservoirs with good vertical permeability. Advantages of horizontal wells over vertical wells include increased productivity, improved sweep efficiency, reduced coning of water and gas, and increased drainage areas (Gilman and Jargon, 1992). Larger contact areas allow lower drawdowns to recover more oil and gas. However, the much greater length of horizontal well available to contact the reservoir makes elaborate completion methods very expensive. There are considerable efforts in the industry to minimize the cost of drilling and completing horizontal wells.

Horizontal wells or laterals are completed as openhole, slotted (perforated) liners, cased/perforated completions, screens, gravel packs, or prepacked screens. The completion selection process starts with determinations of earth stresses, rock mechanical properties, and formation stability over the producing life of the well (Venkitaraman *et al.*, 2001). Preventing borehole collapse and production of formation sand through the wellbore are major issues in the completion choice. Following these analyses, details of the selected completion need to be determined. An optimal completion maintains formation integrity while minimizing pressure losses through the completion hardware and the near wellbore vicinity.

The additional pressure drop caused by the well completion can strongly affect the overall well performance in production and/or injection wells. Particularly in

horizontal wells, where the reservoir pressure drop is low, any pressure drop through the completion can be critical. These well completions may have lower productivity (as characterized by a positive skin) relative to an equivalent openhole completion because convergent flow to the perforations and slots increases fluid velocity in the near-well vicinity. In addition, the effect of scale on the performance of screens or slotted liners, the effect of crushed zone due to perforating, and the effect of damage on a gravel pack may result in a severe pressure drop and impair the completion performance. Since turbulence effects greatly depend on the fluid velocity distribution, with the presence of any flow restriction, the turbulence skin factor can significantly increase, especially for high-rate gas wells.

The optimization of well completions to improve the inflow performance of horizontal wells is a complex but very practical and challenging problem. What is needed is a means for engineers to determine the causes of high skin values occurring under various conditions and suggest techniques to minimize the problems. In particular, the interactions among damage effects and convergent flow to perforations and slots are critical issues to design optimal completions for horizontal wells or laterals.

1.2 LITERATURE REVIEWS

In the past two decades, numerous papers have reported on completion performance models of vertical and horizontal wells, which can be used to predict the productivity of the wells. These models can be categorized into two groups; the numerical models and the (semi-) analytical models.

The numerical models require advanced computer programs to solve the complex flow problem by applying the finite difference method (Dogulu, 1998), the finite element method (Ansah *et al.*, 2002), or the Green's function (source function) method (Tang,

2001). All the methods require the solution of a large matrix system and relatively higher computational time compared with analytical models although they provide accurate solutions for various conditions.

Analytical and semi-analytical models are widely accepted in field practices because they are usually easy to use and provide a better understanding of the relative role of various parameters in affecting well productivity. These models are obtained by solving the complex flow problem with simplified assumptions and are sometimes calibrated by numerical simulation results. Karakas and Tariq (1988) presented a skin equation for cased and perforated well completions using empirical correlations obtained by 2D and 3D FEM simulation results. Their model clearly states the effect of perforation parameters (i.e., wellbore radius, perforation length, perforation diameter, and perforation shot densities) on well productivity. Furui *et al.* (2002) augmented their model to be applied for horizontal wells. The modified model shows the importance of perforation orientation in anisotropic formations.

Frick and Economides (1991) derived an analytical expression for damage skin factor for a truncated elliptical cone of damage with the larger base near the vertical section of the well. Their damage model takes permeability anisotropy into account and is applicable for a horizontal well. Furui *et al.* (2001) also presented a damage skin model, which includes damage heterogeneity along the well and reservoir anisotropy. Their model is based on the pressure equation for an anisotropic medium, and is thus circular near the well and elliptical far from the well.

Kaiser *et al.* (2000) presented an application study for South Bolney sand-control completion design with slotted-liner horizontal wells. They found that inflow resistance depends much more strongly on slot density or on slot spacing than on total slot area.

They concluded that the flow loss through an open slot is negligible compared with that induced by the flow disturbance associated with slot.

Golan and Whitson (1991) presented a skin equation for inside-casing gravel packs, which is based on linear flow through perforation tunnels. Due to the simplicity with few unknown parameters, their model is widely used in field practices.

1.3 OBJECTIVE AND APPROACH

The objective of this study is the development of a theoretical skin factor model to predict the inflow performance of various types of horizontal well completions. Skin is a dimensionless factor calculated to evaluate the production efficiency of a well by comparing actual conditions with theoretical or ideal conditions. The skin concept (Van Everdingen and Hurst, 1949) was originally introduced to account for an additional pressure drop, Δp_s , due to mechanical factors using the radial flow solution as

$$\Delta p_s = \frac{q\mu}{2\pi kL} s \quad (1.1)$$

The skin concept has been interpreted in a wide sense to mathematically account for any deviations of the flow and pressure field in the near-well vicinity from the perfect radial flow to a wellbore radius r_w . A positive skin value indicates some damage or influences that are impairing well productivity. A negative skin value indicates enhanced productivity, typically resulting from well stimulation.

The development of horizontal and multilateral wells has further complicated the skin concept because the impact of skin factors on the overall well productivity greatly depends on the well configuration and the reservoir geometry. The effects of skin on vertical and horizontal well production could be significantly different even with the same skin values, depending on the reservoir anisotropy and the ratio of the reservoir

thickness to the drainage length perpendicular to the well (Furui *et al.*, 2001). Although the effects of skin factor on well productivity are influenced by the well and reservoir geometries, skin factors are independent of those factors if radial flow is obtained in the near-well vicinity. This is usually a reasonable assumption since in most cases the outer boundary of the reservoir is sufficiently distant from the wellbore to be insignificant on the near-wellbore scale (Pucknell and Clifford, 1991). Thus we can use skin factor to analyze the completion performance and identify problems in the near-wellbore vicinity.

In Chapter 2, a mathematically rigorous general form of a skin equation is presented (Furui *et al.*, 2003). The equation contains integrations of a flow area function along the flowpath for the particular flow geometry. The complex flow field induced by the perforations and slots is approximated by a series of linear, radial, and hemispherical flow geometries based on extensive finite element simulation studies. The integrations are solved along the simplified flowpath, which results in an analytical skin equation for the particular flow field. The model is validated with finite element simulation results for various conditions so that the accuracy of the model is ensured. The new completion skin factor model presented in this study accounts for the effects of formation, perforation and gravel damage, convergent flow to perforations and slots, flow through slots, and turbulence effects as well as the interactions among these effects.

To account for formation damage, the rigorous skin model of a damaged horizontal well developed by Furui *et al.*, (2001) is extended to include the presence of perforations within, or extending through, the damage zone. The formation damage model is also integrated with the models of slotted liner performance to model these completions. The slotted liner model accounts for partial plugging of the slots by grains of formation minerals or precipitates (scale). Turbulence effects are a major part of the apparent skin factor for these completion types. The model can be applied to design

optimal completions and provide guidelines to maximize the productivity for horizontal wells or laterals.

1.4 FINITE ELEMENT SIMULATOR

Due to the presence of slots, perforations and various damage zones, the boundary conditions of the differential equation and its geometry become significantly complicated. Analytical solutions to such complex flow field problems are unavailable, thus forcing researchers to use some type of approximate numerical procedure. In this study, the finite element method (FEM) is employed as a computational technique for the solution of the differential equation to be analyzed. Because of the properties of the approximation (interpolation) function, FEM is suitable for the complex geometry and flow concentration problem (Becker *et al.*, 1981).

The theoretical basis for a FEM simulator (IWPCOMPS) designed for the analysis of nonlinear porous flow (i.e., Forchheimer flow) problems is presented in APPENDIX A. The solution method used in IWPCOMPS is based on the Galerkin form of the finite element method. Such a formulation permits great generality in the type of problems that may be treated with a single program. IWPCOMPS is specifically designed to apply for Darcy flow as well as non-Darcy flow problems. Nonlinear solutions are obtained by a standard Picard method. Each of these flow types can be treated in either two-dimensional or three-dimensional coordinate systems. The FEM utilized allows complex geometries to be modeled in an efficient manner. The element library includes linear and quadratic versions of structured and unstructured elements. In order to improve the performance of the solution algorithms, an iterative method (the conjugate gradient method) is employed in IWPCOMPS as well as a direct matrix solution method (the Frontal method, Irons, 1970 and Hood, 1976). The problem types are however, restricted

to steady-state. Finally, new pre- and post- processing file formats have been developed to communicate with an automatic and adaptive mesh generator and graphic user interface, GiD (Diaz, 1999). All the template files are listed and explained in Appendix B.

CHAPTER 2

Near Wellbore Flow through Porous Medium and Skin Factor

2.1 DIFFERENTIAL EQUATION FOR FLUID FLOW THROUGH POROUS MEDIUM.

Consider an arbitrary, fixed volume (control volume) V embedded within a permeable medium. Fig. 2.1 shows that the surface area A of V is made up of elemental surface areas ΔA from the center of which is pointing a unit outward normal vector \mathbf{n} . The sum of all the surface elements ΔA is the total surface area of V . The mass conservation equation for a fluid species in volume V is

$$\left\{ \begin{array}{c} \text{Rate of} \\ \text{accumulation} \\ \text{in } V \end{array} \right\} = \left\{ \begin{array}{c} \text{Rate} \\ \text{transported} \\ \text{into } V \end{array} \right\} - \left\{ \begin{array}{c} \text{Rate} \\ \text{transported} \\ \text{from } V \end{array} \right\} \quad (2.1)$$

The equation is the rate form of the conservation equation; an equivalent form based on cumulative flow follows from integrating Eq. 2.1 with respect to time. The first two terms on the right-hand side of Eq. 2.1 can be written as

$$\left\{ \begin{array}{c} \text{Rate} \\ \text{transported} \\ \text{into } V \end{array} \right\} - \left\{ \begin{array}{c} \text{Rate} \\ \text{transported} \\ \text{from } V \end{array} \right\} = \left\{ \begin{array}{c} \text{Net rate} \\ \text{transported} \\ \text{into } V \end{array} \right\} \quad (2.2)$$

The mathematical form of these terms is given in the following paragraphs. The accumulation term is

$$\left\{ \begin{array}{c} \text{Rate of} \\ \text{accumulation} \\ \text{in } V \end{array} \right\} = \frac{\partial}{\partial t} \left\{ \begin{array}{c} \text{Total mass} \\ \text{in } V \end{array} \right\} = \frac{\partial}{\partial t} \left\{ \int_V \rho \phi dV \right\} \quad (2.3)$$

where ϕ denotes the porosity, which is percentage of the pore volume that can contain fluids. Let \mathbf{u} be the flux vector evaluated at the center of ΔA in units of mass per surface area-time. \mathbf{u} may be readily decomposed into components normal and tangential to the

unit normal vector \mathbf{n} . However, only the normal component $\mathbf{n} \cdot \mathbf{u}$ is crossing ΔA , and the rate of transport across ΔA is

$$\left\{ \begin{array}{l} \text{Net rate} \\ \text{transported} \\ \text{across } \Delta A \end{array} \right\} = -\mathbf{n} \cdot \rho \mathbf{u} \Delta A \quad (2.4)$$

The minus sign arises because \mathbf{n} and \mathbf{u} have opposing directions for transport into ΔA ($\mathbf{n} \cdot \mathbf{u} < 0$), and this term must be positive from Eq. 2.1. Summing up infinitesimal surface elements yields

$$\left\{ \begin{array}{l} \text{Net rate} \\ \text{transported} \\ \text{into } V \end{array} \right\} = -\int_A \mathbf{n} \cdot \rho \mathbf{u} dA \quad (2.5)$$

Since the surface integral is over the entire surface of V , both flow into and from V are included in Eq. 2.5. Application of the conservation of mass into this volume leads to the integral form of the continuity equation:

$$\frac{d}{dt} \int_V \rho \phi dV = \int_A \mathbf{n} \cdot \rho \mathbf{u} dA \quad (2.6)$$

The divergence theorem of Gauss states that if V is a volume bounded by a closed surface A and \mathbf{R} is a continuous vector field, then;

$$\int_V (\nabla \cdot \mathbf{R}) dV = \oint_A (\mathbf{n} \cdot \mathbf{R}) dA \quad (2.7)$$

Thus, the surface integral in Eq. 2.6 may be converted to a volume integral:

$$\frac{d}{dt} \int_V \rho \phi dV = \int_V (\nabla \cdot \rho \mathbf{u}) dV \quad (2.8)$$

Since the control volume is fixed in space, the ordinary derivative may be brought inside of the integral and changed into a partial derivative, allowing both sides of the equation to be consolidated within the integral;

$$\int_V \left(\phi \frac{\partial \rho}{\partial t} - \nabla \cdot \rho \mathbf{u} \right) dV = 0 \quad (2.9)$$

Because the above equation holds for an arbitrary volume V , the integrand must vanish, leading the application to any point within the macroscopic dimensions of the permeable medium.

$$\phi \frac{\partial \rho}{\partial t} - (\nabla \cdot \rho \mathbf{u}) = 0 \quad (2.10)$$

For a three dimensional Cartesian coordinate system,

$$\frac{\partial(\rho u_x)}{\partial x} + \frac{\partial(\rho u_y)}{\partial y} + \frac{\partial(\rho u_z)}{\partial z} = -\phi \frac{\partial \rho}{\partial t} \quad (2.11)$$

There are shorthand notations for partial differential equations. It might be written in the following manners:

$$\frac{\partial \rho u_i}{\partial x_i} = -\phi \frac{\partial \rho}{\partial t} \quad (2.12)$$

Eq. 2.12 is written for a Cartesian geometry in an Eulerian reference frame, with the indices $i=1, 2, 3$ (or $i=1, 2$ for two-dimensional problems); the Einstein summation convention on repeated indices is used.

2.2 DIFFUSIVITY EQUATION

The continuity equation contains the fluid flux vectors u_x , u_y , and u_z . We can now substitute Darcy's law in the continuity equation.

$$\frac{\partial}{\partial x_i} \left(\frac{\rho k_{ij}}{\mu} \frac{\partial \Phi}{\partial x_j} \right) = \phi \frac{\partial \rho}{\partial t} \quad (2.13)$$

This is known as the diffusivity equation, which describes the flow potential generated by the movement of a fluid through a porous medium subject only to the restrictions cited for the continuity equation and assumptions of Darcy's law – no turbulence. Various simplifying assumptions and boundary conditions are used depending upon the type of problem to be studied. Solutions to most petroleum

engineering problems which involve the flow of fluids in a porous medium are based on a solution to some form of the diffusivity equation.

We often assume that the system operates in steady-state flow, which, by definition, means that the mass (or density) of the fluid at a point does not change with time. In other words, $\partial\rho/\partial t = 0$ and:

$$\frac{\partial}{\partial x_i} \left(\rho k_{ij} \frac{\partial \Phi}{\partial x_j} \right) = 0 \quad (2.14)$$

2.3 NON-DARCY FLOW

On the macroscopic scale, flow in a porous media is generally described by Darcy's law, which is valid only for very low velocities. At higher flow velocities, in addition to the viscous force component represented by Darcy's equation, there is also an inertial force acting to convective accelerations of the fluid particles in passing through the pore spaces. Deviations from Darcy's law, observed at high velocities, can be added in mathematical terms in several ways. The most widely accepted model is Forchheimer's equation (Forchheimer, 1901):

$$-\frac{dp}{dx} = \frac{\mu}{k} u + \beta \rho u^2 \quad (2.15)$$

In this equation the first term on the right hand side is the Darcy or viscous component while the second is the non-Darcy component. In this latter term, β is the coefficient of inertial resistance and, as the following dimensional analysis shows, has the dimension $(\text{length})^{-1}$:

$$-\frac{dp}{dx} \left[\frac{ML}{T^2 L^2} \right] \left[\frac{1}{L} \right] = [\beta] \rho \left[\frac{M}{L^3} \right] u^2 \left[\frac{L^2}{T^2} \right] \quad (2.16)$$

$$[\beta] = [L^{-1}] \quad (2.17)$$

The non-Darcy component in Eq. 2.15 is negligible at low flow velocities and is generally omitted from liquid flow equations. For a given pressure drawdown, however, the velocity of gas is at least an order of magnitude greater than for oil, due to the lower viscosity of the former, and the non-Darcy component is therefore often included in equations describing the flow of a real gas through a porous medium.

Existing correlations for high-velocity flow in porous media, including the permeability range on which each correlation is based is reviewed in Table 2.1. Based on a log-log plot of the measured permeability and high-velocity coefficients, the slope a and intercept b can be derived. A common correlation is presented in the form of:

$$\beta = \frac{b}{k^a} \quad (2.18)$$

Values of a and b depend on properties of the formation (or gravel). Some laboratory measurements also include the effect of porosity such as

$$\beta = \frac{b}{k^a \phi^c} \quad (2.19)$$

Eq. 2.15 can be rewritten as

$$-\frac{dp}{dx} = (1 + F_o) \frac{\mu}{k} u \quad (2.20)$$

where F_o is the Forchheimer number, which is similar to the Reynolds number, defined by

$$F_o = \frac{\beta \rho k u}{\mu} \quad (2.21)$$

At low flow rates (e.g., $F_o < 0.01$), the pressure drop is linearly proportional to the flow rate. At high flow rates (e.g., $F_o > 0.1$), the pressure drop exceeds that predicted by Darcy's law.

2.4 GENERAL FORM OF A SKIN EQUATION

Fig. 2.2 shows flowpaths for actual and ideal conditions. The pressure drop for actual and ideal conditions can be estimated by integrating Eq. 2.15 along the flowpaths. The deviation of the flowpath between actual and ideal conditions gives the difference of the pressure drops for the two systems in which is Δp_s . In this study, we postulate that the non-Darcy effects increase the pressure gradient along the flowpath but do not change the flow direction significantly. Eq. 2.15 can be expressed in matrix form as:

$$-\nabla p = \left(\mathbf{I} + \frac{\rho}{\mu} |\mathbf{u}| \boldsymbol{\beta} \cdot \mathbf{k} \right) \cdot \mu \mathbf{k}^{-1} \mathbf{u} \quad (2.22)$$

In anisotropic formations, the permeability and the turbulence factor become anisotropic tensors. When $\boldsymbol{\beta} \propto \mathbf{k}^{-1}$, the product tensor $\boldsymbol{\beta} \cdot \mathbf{k}$ becomes isotropic so that the entire term in the first parenthesis on the right hand side of Eq. 2.22 also reduces to an isotropic tensor. As a result, the non-Darcy effects do not change the original principle directions of hydraulic conductivity of the formation. According to experimental results, the correlation constant a typically ranges between 0.5 and 1.5. Cooper *et al.* (1999) showed that $\boldsymbol{\beta} \cdot \mathbf{k}$ is less anisotropic than either the permeability or the turbulence factor tensors in both experiments and simulations.

Darcy's law in a general form can be expressed as

$$\frac{\partial p}{\partial \xi} = \frac{q\mu}{kA(\xi)} \quad (2.23)$$

where $A(\xi)$ denotes flow area as a function of the flowpath coordinate ξ . Considering the non-Darcy component, Eq. 2.23 becomes

$$\frac{\partial p}{\partial \xi} = \frac{q\mu}{kA(\xi)} + \beta \rho \left(\frac{q}{A(\xi)} \right)^2 \quad (2.24)$$

The pressure drop along the actual pathline is calculated by integrating the above equation from an arbitrary starting point, ξ_0 to an arbitrary end point, ξ_l

$$\int_{\xi_0}^{\xi_1} \frac{\partial p}{\partial \xi} d\xi = \int_{\xi_0}^{\xi_1} \left[\frac{q\mu}{kA(\xi)} + \beta\rho \left(\frac{q}{A(\xi)} \right)^2 \right] d\xi \quad (2.25)$$

In Eq. 2.25 we assume that the flowpath is not significantly distorted by the non-Darcy effect. The pressure drop for the ideal condition, which is commonly assumed to be Darcy flow in the radial coordinates, may be given by integrating Eq. 2.23 along the ideal pathline ξ'

$$\int_{\xi'_0}^{\xi'_1} \frac{\partial p}{\partial \xi'} d\xi' = \int_{\xi'_0}^{\xi'_1} \frac{q\mu}{kA(\xi')} d\xi' \quad (2.26)$$

The difference of the pressure drop between the actual and ideal conditions is then given by

$$\Delta p_s = \int_{\xi_0}^{\xi_1} \frac{q\mu}{kA(\xi)} d\xi + \int_{\xi_0}^{\xi_1} \beta\rho \left(\frac{q}{A(\xi)} \right)^2 d\xi - \int_{\xi'_0}^{\xi'_1} \frac{q\mu}{kA(\xi')} d\xi' \quad (2.27)$$

which can be simplified to

$$\Delta p_s = \frac{q\mu}{k} \left[\int_{\xi_0}^{\xi_1} A^{-1} d\xi - \int_{\xi'_0}^{\xi'_1} A^{-1} d\xi' \right] + \beta\rho q^2 \int_{\xi_0}^{\xi_1} A^{-2} d\xi \quad (2.28)$$

Using the definition of skin (Eq. 1.1) gives

$$\frac{q\mu}{2\pi kL} s = \frac{q\mu}{k} \left[\int_{\xi_0}^{\xi_1} \frac{d\xi}{A} - \int_{\xi'_0}^{\xi'_1} \frac{d\xi'}{A} \right] + \beta\rho q^2 \int_{\xi_0}^{\xi_1} \frac{d\xi}{A^2} \quad (2.29)$$

Solving for skin factor

$$s = 2\pi L \left(\int_{\xi_0}^{\xi_1} A^{-1} d\xi - \int_{\xi'_0}^{\xi'_1} A^{-1} d\xi' \right) + \frac{\beta\rho k}{\mu} (2\pi L q) \int_{\xi_0}^{\xi_1} A^{-2} d\xi \quad (2.30)$$

Introducing the Forchheimer number

$$F_{o,w} = \frac{\beta\rho k}{\mu} \left(\frac{q}{2\pi_w L} \right) \quad (2.31)$$

where the fluid velocity is evaluated at the well surface, Eq. 2.31 can be expressed in the dimensionless form

$$s = \left(\int_{\xi_{D0}}^{\xi_{D1}} A_D^{-1} d\xi_D - \int_{\xi'_{D0}}^{\xi'_{D1}} A_D^{-1} d\xi'_D \right) + \left(\int_{\xi_{D0}}^{\xi_{D1}} A_D^{-2} d\xi_D \right) F_{o,w} \quad (2.32)$$

where the dimensionless variables are defined by

$$A_D = \frac{A}{2\pi r_w L} \quad (2.33)$$

$$\xi_D = \frac{\xi}{r_w} \quad (2.34)$$

Eq. 2.32 can be rewritten by the general expression:

$$s = s^0 + f_t F_{o,w} \quad (2.35)$$

where s^0 and f_t are the rate-independent skin and the turbulence scale factor defined by

$$s^0 = \left(\int_{\xi_{D0}}^{\xi_{D1}} A_D^{-1} d\xi_D - \int_{\xi'_{D0}}^{\xi'_{D1}} A_D^{-1} d\xi'_D \right) \quad (2.36)$$

$$f_t = \int_{\xi_{D0}}^{\xi_{D1}} A_D^{-2} d\xi_D \quad (2.37)$$

If the actual permeability varies along the pathline (e.g. formation damage), Eqs. 2.36 and 2.37 become

$$s^0 = \left(\int_{\xi_{D0}}^{\xi_{D1}} k_D^{-1} A_D^{-1} d\xi_D - \int_{\xi'_{D0}}^{\xi'_{D1}} A_D^{-1} d\xi'_D \right) \quad (2.38)$$

$$f_t = \int_{\xi_{D0}}^{\xi_{D1}} \beta_D A_D^{-2} d\xi_D \quad (2.39)$$

where k_D and β_D are the dimensionless permeability and the dimensionless high-velocity coefficient relative to the original formation permeability and the original high-velocity coefficient.

$A_D(\xi_D)$ denotes the dimensionless flow area as a function of the dimensionless flowpath ξ_D . The skin equation is now presented in the dimensionless form normalized by the wellbore area. It shows that the skin factor is proportional to the Forchheimer number defined by Eq. 2.31 and can be divided into the rate-independent and the rate-dependent terms. The rate-independent skin factor, s^0 , can be explained by changes of the dimensionless flow area between actual and ideal flowpaths. The rate-dependent skin factor is denoted by $f_t F_{o,w}$. The turbulence scale factor, f_t , is extremely sensitive to flow area function $A_D(\xi_D)$. If the actual flow geometry contains narrow flow areas (e.g. flow into perforation tips and slots), f_t may be strongly dominated by those regions. In most of

literature (Economides *et al.*, 1994; Golan and Whitson, 1991; Unneland, 1999), Eq. 2.35

is presented in terms of flow rate, q to give

$$s = s^0 + Dq \quad (2.40)$$

where D is the non-Darcy flow coefficient, equivalent to

$$D = \frac{\beta \rho k}{2\pi r_w L \mu} f_t \quad (2.41)$$

Table 2.1 Summary of existing correlations for high-velocity flow (Unneland, 1999).

Reference	a	b	c	Note
Tek et al. (1962)	1.25	5.50E+09	0.75	
Geertsma from Golan (1959)	0.5	1.75E+07	1.5	
Geertsma from Norman (1959)	0.5	4.85E+04	5.5	
Cooke (1973)	1.54	3.37E+12	-	For 20/40 US mesh gravel
Firoozabadi and Katz (1979)	1.1045	2.73E+10	-	
Tessem, for small pores (1980)	0.9109	3.38E+08	0.9109	
Tessem, for large pores (1980)	1.2829	9.40E+10	1.2829	
Suman (1983)	0.95	2.24E+09	-	
McLeod et al, Cons. (1982)	1.2	2.60E+10	-	
McLeod, Unconsolidated (1982)	0.5	1.00E+07	-	
Nelson et al. (1983)	1	5.01E+08	-	
Brown (1984)	1.201	2.33E+10	-	
Brown, Unconsolidated (1985)	0.55	1.47E+07	-	
Noman et al. (1985)	1.0609	1.12E+10	-	
Beggs (1991)	1.2	2.33E+10	-	
Unneland (1999)	0.5066	4.77E+07	-	

All correlations are in ft^{-1} with permeability in mD.

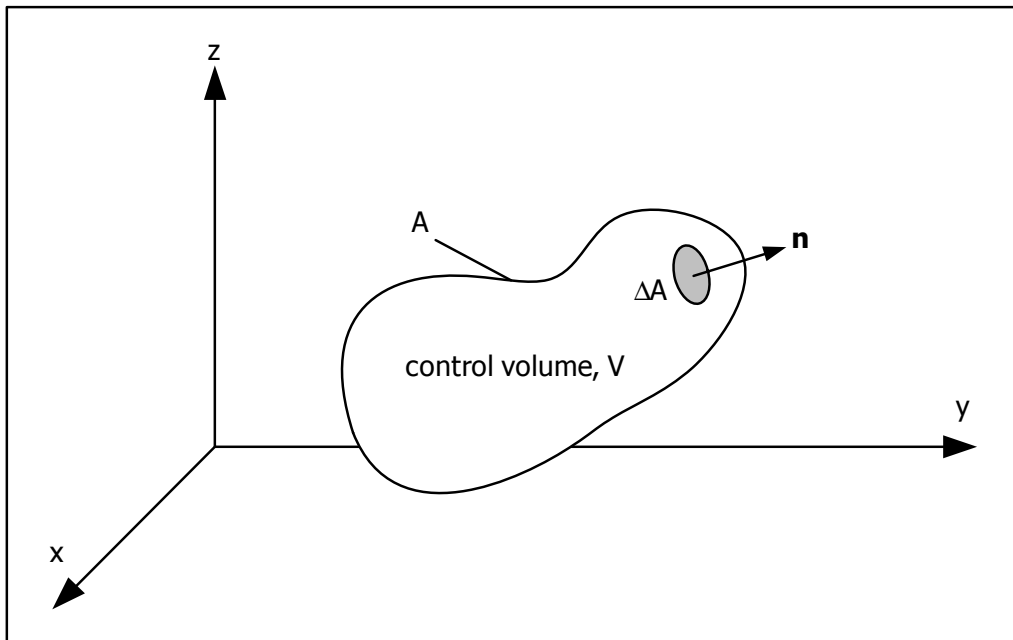


Fig. 2.1 An arbitrary macroscopic control volume.

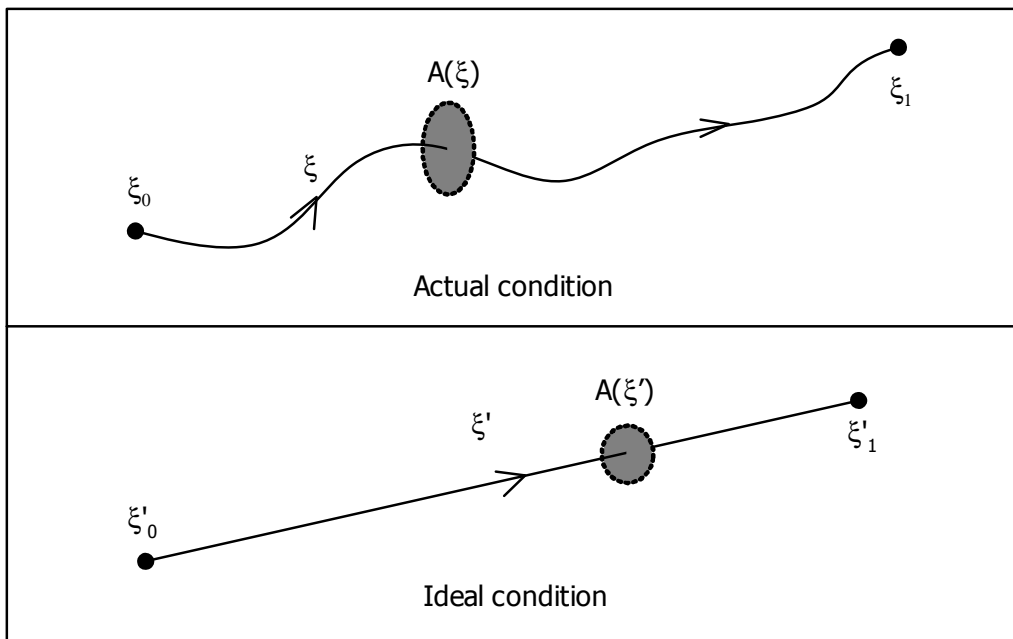


Fig. 2.2 Flowpaths for actual and ideal conditions.

CHAPTER 3

Openhole Completions

3.1 INTRODUCTION TO OPENHOLE COMPLETIONS

The openhole completions are common for horizontal wells, especially for multilateral wells. They call for production casing to be set above the zone of interest and prior to drilling same. The well is completed with the producing interval open to the wellbore. Openhole completions are the simplest and the cheapest. Their use is restricted to reservoirs formed of competent rock that is sufficiently strong to withstand collapsing stresses. Open holes, provided that near-wellbore reservoir damage is not excessive, give the maximum contact with the reservoir. Thus, for example, all transverse fractures that intersect the well will also contact the wellbore. This is not necessarily true for other completion systems. Another advantage of open holes is that they provide the maximum flexibility for future well modification. For example, it is possible, at a later stage, to insert a liner with external casing packers or even to convert an open hole well to a fully cemented completion.

3.2 DEVELOPMENT OF A SKIN EQUATION FOR OPENHOLE COMPLETIONS

Assume that no significant formation damage is present in the near-well vicinity. From the definition of our skin factors, actual and ideal flowpaths for openhole completions become identical so that the rate-independent skin factor given by Eq. 2.36 reduces to zero:

$$\begin{aligned} s_o^0 &= \int_{\xi_{D0}}^{\xi_{D1}} A_D^{-1} d\xi_D - \int_{\xi'_{D0}}^{\xi'_{D1}} A_D^{-1} d\xi_D \\ &= 0 \end{aligned} \tag{3.1}$$

where the subscript O denotes openhole completions (the completion type). The turbulence scale factor is give by

$$\begin{aligned}
 f_{t,O} &= \int_{\xi_{D0}}^{\xi_{D1}} A_D^{-2} d\xi_D \\
 &= \int_1^{r_{Db}} r_D^{-2} dr_D \\
 &= 1 - 1/r_{Db} \\
 &\approx 1
 \end{aligned} \tag{3.2}$$

In the derivation of Eq. 3.2, it is assumed that $1/r_{Db} \ll 1$ ($r_w \ll r_b$). Thus, the total skin factor for undamaged openhole completions is simply

$$s_O = F_{o,w} \tag{3.3}$$

3.3 EFFECT OF FORMATION DAMAGE ON OPEN HOLE COMPLETIONS

Formation damage caused during drilling can significantly reduce the productivity of openhole completions. In terms of reservoir flow, the formation damage can be modeled as a finite region of reduced permeability around the wellbore (Fig. 3.1). Integrating Eq. 2.38, the rate-independent skin factor is calculated by

$$\begin{aligned}
 s_O^0 &= \int_1^{r_{Ds}} k_{Ds}^{-1} A_D^{-1} dr_D - \int_1^{r_{Ds}} A_D^{-1} dr_D \\
 &= (k_{Ds}^{-1} - 1) \int_1^{r_{Ds}} r_D^{-1} dr_D \\
 &= (k_{Ds}^{-1} - 1) \ln r_{Ds}
 \end{aligned} \tag{3.4}$$

Eq. 3.4 is the dimensionless form of the well-known Hawkins' formula (Hawkins, 1956) which is

$$s_O^0 = (k/k_s - 1) \ln(r_s/r_w) \tag{3.5}$$

The turbulence scale factor can be derived by integrating Eq. 2.39

$$\begin{aligned}
 f_{t,O} &= \int_1^{r_{Ds}} \beta_{Ds} r_D^{-2} dr_D + \int_{r_{Ds}}^{r_{Db}} r_D^{-2} dr_D \\
 &= (1 - 1/r_{Ds}) \beta_{Ds} + (1/r_{Ds} - 1/r_{Db}) \\
 &\approx (1 - 1/r_{Ds}) \beta_{Ds} + 1/r_{Ds} \\
 &= \beta_{Ds} + (1 - \beta_{Ds})/r_{Ds}
 \end{aligned} \tag{3.6}$$

We presume that in anisotropic formations, the shape of the damaged region perpendicular to the wellbore (a vertical plane in Fig. 3.1) mimics the isobars given by Peaceman's solution for flow through an anisotropic permeability field (Peaceman, 1983), and is thus circular near the well and elliptical far from the well. The rate-independent skin factor is derived in terms of the mean radius, \bar{r} , which is defined in the equivalent isotropic system (Furui, *et al.*, 2002):

$$\begin{aligned} s_O^0 &= \int_1^{\bar{r}_s/\bar{r}_w} k_{Ds}^{-1} \bar{r}_D^{-1} d\bar{r}_D - \int_1^{\bar{r}_s/\bar{r}_w} \bar{r}_D^{-1} d\bar{r}_D \\ &= (k_{Ds}^{-1} - 1) \ln(\bar{r}_s / \bar{r}_w) \end{aligned} \quad (3.7)$$

Peaceman (1983) derived that the equivalent wellbore radius can be given by

$$\bar{r}_w = 0.5 r_w (I_{ani} + 1) / \sqrt{I_{ani}} \quad (3.8)$$

where I_{ani} is the index of anisotropy defined by

$$I_{ani} = \sqrt{k_H / k_V} \quad (3.9)$$

According to Furui, *et al.* (2002), the mean radius of damage can be expressed in terms of the reservoir anisotropy and the damage radius in the horizontal direction as

$$\bar{r}_s = 0.5 r_w \left(r_{DsH} + \sqrt{r_{DsH}^2 + I_{ani}^2 - 1} \right) / \sqrt{I_{ani}} \quad (3.10)$$

where r_{DsH} is the dimensionless damage radius in the horizontal direction defined by

$$r_{DsH} = r_{sH} / r_w \quad (3.11)$$

Substituting Eqs. 3.8 and 3.10 into Eq. 3.7 reduces to

$$s_O^0 = (k_{Ds}^{-1} - 1) \ln \left(\frac{r_{DsH} + \sqrt{r_{DsH}^2 + I_{ani}^2 - 1}}{I_{ani} + 1} \right) \quad (3.12)$$

and the turbulent scale factor is calculated by

$$\begin{aligned} f_{t,O} &= \int_1^{\bar{r}_s/\bar{r}_w} \beta_{Ds} \bar{r}_D^{-2} d\bar{r}_D + \int_{\bar{r}_s/\bar{r}_w}^{\bar{r}_b/\bar{r}_w} \bar{r}_D^{-2} d\bar{r}_D \\ &= (1 - \bar{r}_w / \bar{r}_s) \beta_{Ds} + (\bar{r}_w / \bar{r}_s - \bar{r}_w / \bar{r}_b) \\ &\approx (1 - \bar{r}_w / \bar{r}_s) \beta_{Ds} + \bar{r}_w / \bar{r}_s \\ &= \beta_{Ds} + (1 - \beta_{Ds}) \left(\frac{I_{ani} + 1}{r_{DsH} + \sqrt{r_{DsH}^2 + I_{ani}^2 - 1}} \right) \end{aligned} \quad (3.13)$$

Fig. 3.2 shows the comparison of the analytical equations developed here with FEM simulation results for various penetrations of damage. In this example, $r_w = 0.3$ ft, and the permeability impairment ratio, k_{Ds} , is 0.1. Overall, these results match very well.

Table 3.1 Numerical data for Fig. 3.2.

I_{ani}	r_{sH}	FEM		Analytical	
		s^0	f_t	s^0	f_t
-	ft	-	-	-	-
1	0.3	0.00	0.97	0.00	1.00
1	0.4	2.59	3.83	2.59	3.93
1	0.6	6.25	6.71	6.24	6.86
1	1.0	10.85	9.02	10.84	9.20
1	2.0	17.09	10.66	17.07	10.96
1	5.0	25.34	11.73	25.32	12.02
2	0.3	0.00	1.44	0.00	1.00
2	0.6	3.93	5.50	3.94	5.15
2	1.0	7.74	8.27	7.74	7.76
2	2.0	13.58	10.50	13.57	10.13
2	5.0	21.70	12.38	21.70	11.67
5	0.3	0.00	1.29	0.00	1.00
5	0.6	1.75	3.58	1.76	3.08
5	1.0	3.90	6.09	3.90	5.13
5	2.0	8.22	9.48	8.21	8.01
5	5.0	15.62	12.50	15.62	10.65

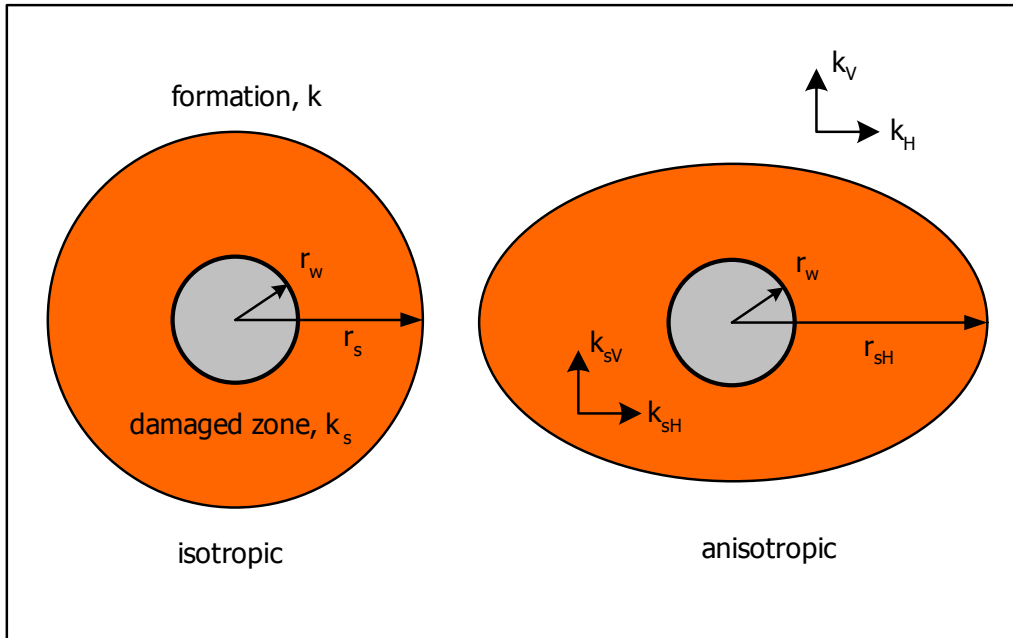


Fig. 3.1 Vertical section of a open hole well with formation damage.

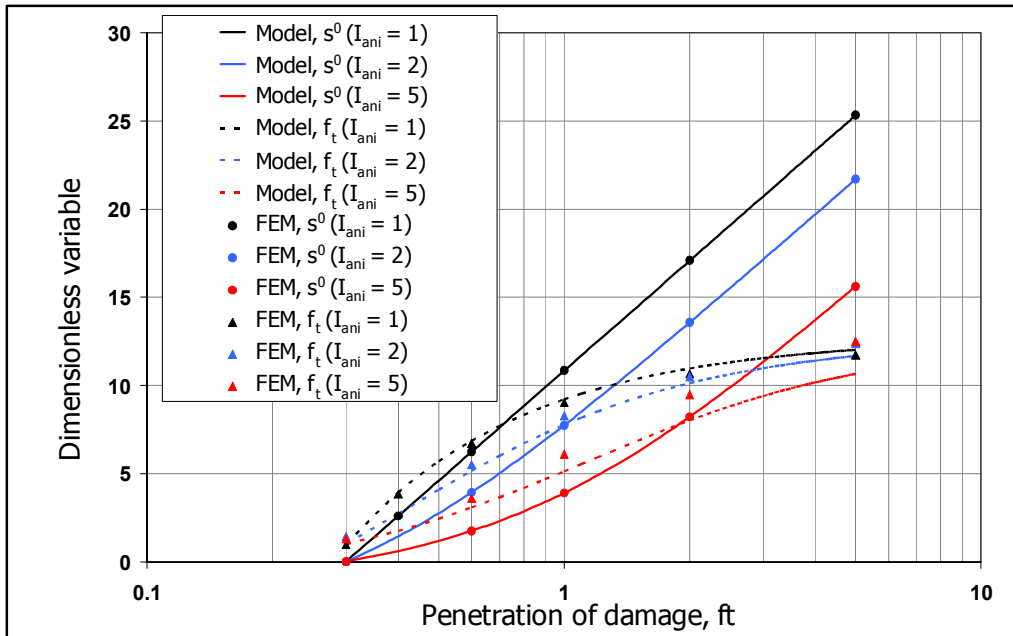


Fig. 3.2 Comparison with FEM simulation results, openhole completions.

CHAPTER 4

Slotted or Perforated Liners

4.1 INTRODUCTION TO SLOTTED LINER COMPLETIONS

Slotted liners are widely used for horizontal well completions to maintain borehole integrity and to prevent formation collapse. A slotted liner has numerous long and narrow openings (slots) which are milled into the base pipe to allow fluids to flow into the liner. Slot style is characterized by the arrangement of the slots around the circumference of the liner (Fig. 4.1). The most commonly used slot pattern is staggered slots with multiple slots in a concentrated location (multiple staggered).

A skin equation for slotted liners developed in the following section accounts mainly for the flow convergence to slots, the slot plugging, effects of formation damage and the interactions among these effects. We assume that formation has collapsed and tightly contacted with the liner. If formation is hard enough to have open space around the liner, skin is lower, especially with damage. In this case, Eqs. 3.12 and 3.13 can be applied to estimate skin factors.

4.2 DEVELOPMENT OF A SKIN EQUATION FOR SLOTTED LINERS

For single inline slotted liners, the slotted liner skin, s_{SL} , is a function of the slot width, w_s ; the slot length, l_s ; the number of slots (or slot units) around the circumference of the liner, m_s ; the slot penetration ratio, λ defined as the length of slots per unit length of pipe (Tang, 2001); and the wellbore radius, r_w . Fig. 4.2 shows the pressure distribution in the formation around single inline slotted liners obtained by FEM simulation. A constant pressure boundary condition is applied to the nodes on the slots (inlet) in the simulations.

The convergent flow field to slots can be characterized as a series of radial flow fields. The outer radius, $(1+v)r_w$, may be geometrically determined by creating the maximum radius from the slots which can separate the flow regions symmetrically (Fig. 4.3). With this observation, v can be obtained by the following relationship;

$$v = \sin(\pi / m_s) \text{ for } m_s \neq 1 \quad (4.1)$$

According to FEM simulation results, $v \approx 1.5$ for $m_s = 1$ (only one slot around the circumference of the liner is a quite unusual condition).

When the slot penetration ratio is not sufficient, the convergent flow along the liner (the axial flow convergence) needs to be considered (Fig. 4.4). We presume that the thickness of the radial flow region defined by Eq. 4.1 is also expressed by a function of a distance from the slot (Fig. 4.5). The radius of the axial convergence zone, γ_w , which is measured from the surface of the liner, is empirically determined by taking half of the slot unit length, l_u , so that

$$\gamma = l_{Ds} / (2\lambda) \quad (4.2)$$

where l_{Ds} ($=l_s/r_w$) is the dimensionless slot length. The approximate flow geometries described here give the dimensionless flow area A_d along the dimensionless flowpath ξ_d . Integrations of Eqs. 2.36 and 2.37 for the approximate flow geometries gives the rate-independent skin factor, s_{SL}^0 , and the turbulent scale factor, $f_{t,SL}$.

Fig. 4.6 shows the schematic of flow to slotted liners. The flow geometry can be divided into four components; the linear flow through slots, the radial flow induced by multiple slots, the radial flow induced by the slot unit angular distribution, and the radial flow away from the liner. In addition to the above flow transitions, the axial flow convergence into slots needs to be considered especially for low slot penetration ratio ($\lambda < 1$). We assume the thickness of the radial flow inside the convergence zone to be a function of the distance from a liner. The approximate flow geometries allow us to

express flow area as a function of the distance from a liner and integrate it along the flowpath.

Linear Flow inside Slots.

The total open area of a slotted liner is given by

$$A = n_s m_s w_s L \lambda \quad (4.3)$$

and the dimensionless form is

$$A_D = n_s m_s w_{Ds} \lambda / (2\pi) \quad (4.4)$$

where

$$w_{Ds} = w_s / r_w \quad (4.5)$$

Letting k_s be permeability inside the slots and integrating the first term of Eq. 2.38 in linear coordinates gives

$$\begin{aligned} \int_{x_{D0}}^{x_{D1}} \frac{dx_D}{k_D A_D} &= \int_0^{t_{sD}} \left[\frac{2\pi}{n_s m_s w_{Ds} \lambda k_{D\ell}} \right] dx_D \\ &= \left(\frac{2\pi}{n_s m_s w_{Ds} \lambda} \right) \frac{t_{Ds}}{k_{D\ell}} \end{aligned} \quad (4.6)$$

where $t_{Ds} (=t_s/r_w)$ is the dimensionless thickness of the liner or the depth of partial plugging. Similarly the integration of Eq. 2.39 for the linear flow region yields

$$\int_{x_{D0}}^{x_{D1}} \frac{\beta_D dx_D}{A_D^2} = \left(\frac{2\pi}{n_s m_s w_{Ds} \lambda} \right)^2 \beta_{D\ell} t_{Ds} \quad (4.7)$$

Radial Flow Induced by Multiple Slots.

The radial flow induced by multiple slots is shown in Fig. 4.6. The inner and outer radii of the radial flow geometry are denoted by r_1 and r_2 , respectively. Similarly to the equivalent well radius of a fracture (Prats, 1961), the equivalent radius of r_1 is given by $w_s/4$. r_2 is geometrically determined by r_u/n_s . Assuming $r_u \approx w_u/2$, r_2 is given by $w_u/2n_s$. The flow area for the radial flow is given by a function of the distance from a slot, r

$$A = n_s m_s (\lambda L / l_s) \pi r h \quad (4.8)$$

and in dimensionless form

$$A_D = n_s m_s (\lambda / l_{Ds}) r_D h_D / 2 \quad (4.9)$$

The dimensionless thickness of the radial flow measured from a slot is given by

$$h_D = h_1 r_D + h_2 \quad (4.10)$$

where

$$h_1 = 2(1 - \lambda) \quad (4.11)$$

$$h_2 = l_{Ds} \quad (4.12)$$

Integration of the dimensionless flow area in radial coordinates gives

$$\int_{r_{D1}}^{r_{D2}} \frac{dr_D}{A_D} = \frac{2l_{Ds}}{n_s m_s \lambda} \int_{r_{D1}}^{r_{D2}} \frac{dr_D}{r_D h_D} \quad (4.13)$$

Integration of the right hand side gives

$$\begin{aligned} \int_{r_{D1}}^{r_{D2}} \frac{dr_D}{r_D h_D} &= \int_{w_{Ds}/4}^{w_{Du}/2n_s} \frac{dr_D}{r_D (h_1 r_D + h_2)} \\ &= \frac{1}{h_2} \left| \ln \left(\frac{h_1}{h_1 + h_2 / r_D} \right) \right|_{w_{Ds}/4}^{w_{Du}/2n_s} \\ &= \frac{1}{l_{Ds}} \ln \left(\frac{1 - \lambda + 2l_{Ds} / w_{Ds}}{1 - \lambda + n_s l_{Ds} / w_{Du}} \right) \end{aligned} \quad (4.14)$$

Substituting Eq. 4.14 into Eq. 4.13 gives

$$\int_{r_{D1}}^{r_{D2}} \frac{dr_D}{A_D} = \frac{2}{n_s m_s \lambda} \ln \left(\frac{1 - \lambda + 2l_{Ds} / w_{Ds}}{1 - \lambda + n_s l_{Ds} / w_{Du}} \right) \quad (4.15)$$

Similarly, the integration of Eq. A-16 for the radial flow region is given by

$$\begin{aligned} \int_{r_{D1}}^{r_{D2}} \frac{dr_D}{A_D^2} &= \left(\frac{2}{n_s m_s \lambda} \right)^2 \left\{ -\frac{4(1 - \lambda)}{l_{Ds}} \ln \left(\frac{1 - \lambda + 2l_{Ds} / w_{Ds}}{1 - \lambda + n_s l_{Ds} / w_{Du}} \right) \right. \\ &\quad \left. + \frac{4}{w_{Ds}} - \frac{2n_s}{w_{Du}} + \frac{4(1 - \lambda)}{(1 - \lambda)w_{Ds} + 2l_{Ds}} - \frac{2(1 - \lambda)}{(1 - \lambda)w_{Du} / n_s + l_{Ds}} \right\} \end{aligned} \quad (4.16)$$

Radial Flow Induced by the Angular Distribution of Slot Units.

The inner and outer radii of the radial flow induced by the angular distribution of slot units are defined by r_2 and r_3 , respectively. The inner radius, r_2 is equal to r_u as shown in Fig. 4.6 and r_3 is $v r_w$. The parameter v is a function of the angular distribution of slot units around the circumference of the liner (Eq. 4.1). The flow area is given by a function of the distance from a slot

$$A = m_s (\lambda L / l_s) \pi r h \quad (4.17)$$

and in dimensionless form

$$A_D = m_s (\lambda / l_{Ds}) r_D h_D / 2 \quad (4.18)$$

Integration of the inverse of the dimensionless flow area gives

$$\int_{r_{D2}}^{r_{D3}} \frac{dr_D}{A_D} = \frac{2l_{Ds}}{m_s \lambda} \int_{r_{D2}}^{r_{D3}} \frac{dr_D}{r_D h_D} \quad (4.19)$$

For high slot densities along a liner ($\gamma \ll v$), the integration in the right hand side gives

$$\begin{aligned} \int_{r_{D2}}^{r_{D3}} \frac{dr_D}{r_D h_D} &= \int_{w_{Du}/2}^{\gamma} \frac{dr_D}{r_D (h_1 r_D + h_2)} + \int_{\gamma}^v \frac{dr_D}{r_D (l_{Ds} / \lambda)} \\ &= \frac{1}{l_{Ds}} \ln(1 - \lambda + l_{Ds} / w_{Du}) + \frac{\lambda}{l_{Ds}} \ln \frac{v}{\gamma} \end{aligned} \quad (4.20)$$

Substituting Eq. 4.20 into Eq. 4.19 gives

$$\int_{r_{D2}}^{r_{D3}} \frac{dr_D}{A_D} = \frac{2}{m_s} \left[\frac{1}{\lambda} \ln(1 - \lambda + l_{Ds} / w_{Du}) + \ln \left(\frac{2\lambda v}{l_{Ds}} \right) \right] \quad (4.21)$$

Similarly,

$$\begin{aligned} \int_{r_{D2}}^{r_{D3}} \frac{dr_D}{A_D^2} &= \left(\frac{2}{m_s} \right)^2 \left\{ \frac{1}{\lambda^2} \left[-\frac{4(1-\lambda)}{l_{Ds}} \ln(1 - \lambda + l_{Ds} / w_{Du}) \right. \right. \\ &\quad \left. \left. + \frac{2}{w_{Du}} - \frac{1}{v} + \frac{2(1-\lambda)}{(1-\lambda)w_{Du} + l_{Ds}} - \frac{2(1-\lambda)}{2(1-\lambda)v + l_{Ds}} \right] + \frac{1}{v} - \frac{2\lambda}{l_{Ds}} \right\} \end{aligned} \quad (4.22)$$

For low slot penetration ratio ($\gamma \gg v$), the integration is given by

$$\begin{aligned}\int_{r_{D2}}^{r_{D3}} \frac{dr_D}{r_D h_D} &= \int_{w_{Du}/2}^v \frac{dr_D}{r_D (h_1 r_D + h_2)} \\ &= \frac{1}{l_{Ds}} \ln \left[\frac{1 - \lambda + l_{Ds} / w_{Du}}{1 - \lambda + l_{Ds} / (2v)} \right]\end{aligned}\quad (4.23)$$

Substituting Eq. 4.23 into Eq. 4.19 gives

$$\int_{r_{D2}}^{r_{D3}} \frac{dr_D}{A_D} = \frac{2}{m_s \lambda} \ln \left[\frac{1 - \lambda + l_{Ds} / w_{Du}}{1 - \lambda + l_{Ds} / (2v)} \right] \quad (4.24)$$

The integration for the turbulence scale factor is

$$\begin{aligned}\int_{r_{D2}}^{r_{D3}} \frac{dr_D}{A_D^2} &= \left(\frac{2}{m_s \lambda} \right)^2 \left\{ -\frac{4(1-\lambda)}{l_{Ds}} \ln \left[\frac{1 - \lambda + l_{Ds} / w_{Du}}{1 - \lambda + l_{Ds} / (2v)} \right] \right. \\ &\quad \left. + \frac{2}{w_{Du}} - \frac{1}{v} + \frac{2(1-\lambda)}{(1-\lambda)w_{Du} + l_{Ds}} - \frac{2(1-\lambda)}{2(1-\lambda)v + l_{Ds}} \right\}\end{aligned}\quad (4.25)$$

Radial Flow Away From a Liner.

The largest radial flow region is observed where the distance from a liner is sufficient.

The inner and outer radii of the radial flow are defined by r_3 and r_4 , respectively. From Fig. 4.3, the inner radius r_3 is determined by $(1+v)r_w$ and the outer radius r_4 is set to r_b .

The flow area is given by a function of the distance from a slot

$$A = 2\pi(\lambda L / l_s) r h \quad (4.26)$$

and in dimensionless form

$$A_D = (\lambda / l_{Ds}) r_D h_D \quad (4.27)$$

The integration of the inverse of the dimensionless flow area gives

$$\int_{r_{D3}}^{r_{D4}} \frac{dr_D}{A_D} = \frac{l_{Ds}}{\lambda} \int_{r_{D3}}^{r_{D4}} \frac{dr_D}{r_D h_D} \quad (4.28)$$

For $\lambda \ll v$, Eq. the above equation becomes

$$\begin{aligned}\int_{r_{D3}}^{r_{D4}} \frac{dr_D}{A_D} &= \frac{l_{Ds}}{\lambda} \int_{1+v}^{r_{Db}} \frac{dr_D}{r_D (l_{Ds} / \lambda)} \\ &= \ln \left(\frac{r_{Db}}{1+v} \right)\end{aligned}\quad (4.29)$$

and

$$\int_{r_{D3}}^{r_{D4}} \frac{dr_D}{A_D^2} = \frac{1}{1+v} - \frac{1}{r_{Db}} \quad (4.30)$$

Assuming $1/r_{Db} \ll 1$, Eq. 4.30 becomes

$$\int_{r_{D3}}^{r_{D4}} \frac{dr_D}{A_D^2} \approx \frac{1}{1+v} \quad (4.31)$$

For $\gamma \gg v$, the dimensionless thickness of the radial flow measured from the center of the wellbore may be expressed as

$$h_D = h_1 r_D + h_2 \quad (4.32)$$

where

$$h_1 = 2(1 - \lambda) \quad (4.33)$$

$$h_2 = l_{Ds} - 2(1 - \lambda) \quad (4.34)$$

Then

$$\begin{aligned}\int_{r_{D3}}^{r_{D4}} \frac{dr_D}{r_D h_D} &= \int_{1+v}^{1+\gamma} \frac{dr_D}{r_D (h_1 r_D + h_2)} + \int_{1+\gamma}^{r_{Db}} \frac{dr_D}{r_D (l_{Ds} / \lambda)} \\ &= \frac{1}{l_{Ds} - 2(1 - \lambda)} \ln \left\{ \left(\frac{\lambda + l_{Ds} / 2}{1+v} \right) \left[1 + \frac{2v(1 - \lambda)}{l_{Ds}} \right] \right\} \\ &\quad + (\lambda / l_{Ds}) \ln [r_{Db} / (1 + \gamma)]\end{aligned}\quad (4.35)$$

Substituting Eq. 4.35 into Eq. 4.28 gives

$$\begin{aligned}\int_{r_{D3}}^{r_{D4}} \frac{dr_D}{A_D} &= \left(\frac{l_{Ds} / \lambda}{l_{Ds} - 2(1 - \lambda)} \right) \ln \left\{ \left(\frac{\lambda + l_{Ds} / 2}{1+v} \right) \right. \\ &\quad \left. \times \left[1 + \frac{2v(1 - \lambda)}{l_{Ds}} \right] \right\} + \ln \left(\frac{r_{Db}}{1 + l_{Dp} / 2\lambda} \right)\end{aligned}\quad (4.36)$$

Similarly,

$$\begin{aligned}
\int_{r_{D3}}^{r_{D4}} \frac{dr_D}{A_D^2} &= \left[\frac{l_{Ds} / \lambda}{l_{Ds} - 2(1-\lambda)} \right]^2 \left\{ \frac{1}{1+v} - \frac{1}{1+l_{Ds}/(2\lambda)} \right. \\
&\quad \left. + \frac{2(1-\lambda)}{2(1-\lambda)v+l_{Ds}} - \frac{2\lambda(1-\lambda)}{l_{Ds}} - \left[\frac{4(1-\lambda)}{l_{Ds} - 2(1-\lambda)} \right] \right. \\
&\quad \left. \times \ln \left[\left(\frac{\lambda+l_{Ds}/2}{1+v} \right) \left(1 + \frac{2v(1-\lambda)}{l_{Ds}} \right) \right] \right\} + \left(\frac{1}{1+l_{Ds}/2\lambda} \right)
\end{aligned} \tag{4.37}$$

Darcy flow in radial coordinates is chosen as the ideal condition (i.e., openhole completions and no turbulence effects) to give

$$\begin{aligned}
\int_{r'_{D0}}^{r'_{D1}} \frac{dr'_D}{A_D} &= \int_1^{r_{Db}} \frac{dr'_D}{r_D} \\
&= \ln r_{Db}
\end{aligned} \tag{4.38}$$

Consequently the slotted liner skin s_{SL} can be expressed as

$$s_{SL} = s_{SL}^0 + f_{t,SL} F_{o,w} \tag{4.39}$$

where

$$s_{SL}^0 = s_{SL,\ell}^0 + s_{SL,r}^0 \tag{4.40}$$

$$f_{t,SL} = f_{t,SL,\ell} + f_{t,SL,r} \tag{4.41}$$

The subscript, \bullet and r , denote the linear flow inside the slots and the radial flow outside the liner. The rate-independent skin and the turbulence scale factors for the linear flow geometry components are given by

$$s_{SL,\ell}^0 = \left(\frac{2\pi}{n_s m_s w_{Ds} \lambda} \right) \frac{t_{Ds}}{k_{D\ell}} \tag{4.42}$$

$$f_{t,SL,\ell} = \left(\frac{2\pi}{n_s m_s w_{Ds} \lambda} \right)^2 \beta_{D\ell} t_{Ds} \tag{4.43}$$

For unplugged slots ($k \gg k$), $s_{SL,\ell}^0$ and $f_{t,SL,\ell}$ are negligible. The radial flow components are expressed as follows:

For high slot penetration ratio ($\gamma < \nu$), adding the integration results, Eqs. 4.15, 4.21, and 4.29 and subtracting Eq. 4.38 give the rate-independent skin factor of the radial flow component;

$$s_{SL,r}^0 = \left(\frac{2}{n_s m_s \lambda} \right) \ln \left(\frac{1 - \lambda + 2l_{Ds} / w_{Ds}}{1 - \lambda + n_s l_{Ds} / w_{Du}} \right) + \left(\frac{2}{m_s} \right) \times \left[\frac{1}{\lambda} \ln(1 - \lambda + l_{Ds} / w_{Du}) + \ln \left(\frac{2\lambda \nu}{l_{Ds}} \right) \right] - \ln(1 + \nu) \quad (4.44)$$

Adding Eqs. 4.16, 4.22, and 4.31 gives

$$f_{t,SL,r} = \left(\frac{2}{n_s m_s \lambda} \right)^2 \left\{ -\frac{4(1-\lambda)}{l_{Ds}} \times \ln \left(\frac{1 - \lambda + 2l_{Ds} / w_{Ds}}{1 - \lambda + n_s l_{Ds} / w_{Du}} \right) + \frac{4}{w_{Ds}} - \frac{2n_s}{w_{Du}} + \frac{4(1-\lambda)}{(1-\lambda)w_{Ds} + 2l_{Ds}} - \frac{2(1-\lambda)}{(1-\lambda)w_{Du} / n_s + l_{Ds}} \right\} + \left(\frac{2}{m_s} \right)^2 \left\{ \frac{1}{\lambda^2} \left[-\frac{4(1-\lambda)}{l_{Ds}} \ln(1 - \lambda + l_{Ds} / w_{Du}) + \frac{2}{w_{Du}} - \frac{1}{\nu} + \frac{2(1-\lambda)}{(1-\lambda)w_{Du} + l_{Ds}} - \frac{2(1-\lambda)}{2(1-\lambda)\nu + l_{Ds}} \right] + \left(\frac{1}{\nu} - \frac{2\lambda}{l_{Ds}} \right) \right\} + \frac{1}{1+\nu} \quad (4.45)$$

For low slot penetration ratio ($\gamma > \nu$), Eqs. 4.15, 4.24, 4.36, and 4.38 are used to give

$$s_{SL,r}^0 = \left(\frac{2}{n_s m_s \lambda} \right) \ln \left(\frac{1 - \lambda + 2l_{Ds} / w_{Ds}}{1 - \lambda + n_s l_{Ds} / w_{Du}} \right) + \left(\frac{2}{m_s \lambda} \right) \ln \left[\frac{1 - \lambda + l_{Ds} / w_{Du}}{1 - \lambda + l_{Ds} / (2\nu)} \right] + \left(\frac{l_{Ds} / \lambda}{l_{Ds} - 2(1-\lambda)} \right) \ln \left\{ \left(\frac{\lambda + l_{Ds} / 2}{1 + \nu} \right) \left[1 + \frac{2\nu(1-\lambda)}{l_{Ds}} \right] \right\} - \ln \left(1 + \frac{l_{Ds}}{2\lambda} \right) \quad (4.46)$$

From Eqs. 4.16, 4.25, and 4.37,

$$\begin{aligned}
f_{t,SL,r} = & \left(\frac{2}{n_s m_s \lambda} \right)^2 \left\{ -\frac{4(1-\lambda)}{l_{Ds}} \ln \left(\frac{1-\lambda + 2l_{Ds}/w_{Ds}}{1-\lambda + n_s l_{Ds}/w_{Du}} \right) + \frac{4}{w_{Ds}} - \frac{2n_s}{w_{Du}} \right. \\
& + \frac{4(1-\lambda)}{(1-\lambda)w_{Ds} + 2l_{Ds}} - \frac{2(1-\lambda)}{(1-\lambda)w_{Du}/n_s + l_{Ds}} \left. \right\} + \left(\frac{2}{m_s \lambda} \right)^2 \left\{ -\frac{4(1-\lambda)}{l_{Ds}} \right. \\
& \times \ln \left[\frac{1-\lambda + l_{Ds}/w_{Du}}{1-\lambda + l_{Ds}/(2v)} \right] + \frac{2}{w_{Du}} - \frac{1}{v} + \frac{2(1-\lambda)}{(1-\lambda)w_{Du} + l_{Ds}} - \frac{2(1-\lambda)}{2(1-\lambda)v + l_{Ds}} \left. \right\} \quad (4.47) \\
& + \left[\frac{l_{Ds}/\lambda}{l_{Ds} - 2(1-\lambda)} \right]^2 \left\{ \frac{1}{1+v} - \frac{1}{1+l_{Ds}/(2\lambda)} + \frac{2(1-\lambda)}{2(1-\lambda)v + l_{Ds}} - \frac{2\lambda(1-\lambda)}{l_{Ds}} \right. \\
& - \left. \left[\frac{4(1-\lambda)}{l_{Ds} - 2(1-\lambda)} \right] \ln \left[\left(\frac{\lambda + l_{Ds}/2}{1+v} \right) \left[1 + \frac{2v(1-\lambda)}{l_{Ds}} \right] \right] \right\} + \left(\frac{1}{1+l_{Ds}/2\lambda} \right)
\end{aligned}$$

Fig. 4.7 shows the pressure distribution of a slotted liner with plugged slots. A severe pressure drop occurs inside the slots. If the slots are filled by formation sand (i.e., $k_s=k$), the linear flow terms given by Eqs. 4.42 and 4.43 become dominant and increase the skin factor and the turbulence effect. In such cases, $s_{SL,r}^0$ and $f_{t,SL,r}$ may be negligible.

For staggered slots, we expect slightly smaller skin factors than inline ones. Muskat (1949) discussed a line drive supplying liquid to two line arrays of wells which were mutually staggered. He showed that staggering the well arrays would have no effect on the shielding and leakage characteristics of a system unless the distances between the lines were made appreciably less than the spacing of the wells in the lines. Similarly, the staggering of slots is characterized by the distances between slots. The number of slots around the circumference of the liner may be effectively doubled as l_{Du} ($=l_{Ds}/\lambda$) approaches 0. With these observations, we introduce the following correlation equation to obtain the effective slot angular distribution m'_s as

$$m'_s = m_s (1 + e^{-m_s l_{Ds}/\lambda}) \quad (4.48)$$

The skin factors for staggered slots can be obtained by replacing m_s by m'_s in Eqs. 4.1 and 4.42-4.47. Fig. 4.8 shows the comparison of Eq. 4.48 with FEM simulation results. It shows a good match with acceptable errors.

Unlike cased and perforated wells, the effect of formation anisotropy is not significant for slotted liner completion with 4 or more slot units around the circumference of a liner. The liner orientation relative to the permeability field has no significant effect on skin factor. Using the coordinate transformation into the equivalent isotropic system, the dimensionless slot length can be obtained by a function of the formation permeabilities as

$$l_{Ds} = \frac{2l_s / r_w}{\sqrt{k_x / k_z} + \sqrt{k_x / k_y}} \quad (4.49)$$

where a liner is assumed to be placed along the x -direction. Substituting Eq. 4.49 into the skin model gives skin factors in anisotropic formations. Fig. 4.9 shows an example of slotted liner skin factors in anisotropic formations. The effect of formation anisotropy is not significant.

4.3 DEVELOPMENT OF A SKIN EQUATION FOR PERFORATED LINERS

The flow geometry of perforated liners is similar to that of slotted liners (Fig. 4.10). The convergent flow to perforations milled through the liner is more likely to be hemispherical flow rather than radial flow. Replacing l_s with a perforation diameter, $2r_p$, in Eq. 4.2 γ for perforated liners can be given by

$$\gamma = r_{Dp} / \lambda \quad (4.50)$$

The flow area of the hemispherical flow region is given by

$$A = (m_p L \lambda / 2r_p)(2\pi r^2) \quad (4.51)$$

and in dimensionless form

$$A_D = m_p \lambda r_D^2 / (2r_{Dp}) \quad (4.52)$$

The inner and outer radii of the spherical flow region are defined by r_0 and r_i , respectively. The equivalent inner radius of the spherical flow created by a perforation is estimated in a similar manner to the equivalent well radius of the wellbore in an anisotropic formation. Taking the arithmetic average of three radii in the orthogonal directions gives

$$r_0 = 2r_p / 3 \quad (4.53)$$

(FEM simulation results shows that the equivalent radius of a sphere is $0.64 \sim 0.65 r_p$)

For high perforation shot densities ($\gamma < v$), the outer radius r_i is equal to γr_w .

$$\begin{aligned} \int_{r_{D0}}^{r_{D1}} A_D^{-1} dr_D &= 2r_{Dp} / (m_p \lambda) \int_{2r_{Dp}/3}^{\gamma} r_D^{-2} dr_D \\ &= 2 / (m_p \lambda) (3/2 - \lambda) \end{aligned} \quad (4.54)$$

and

$$\begin{aligned} \int_{r_{D0}}^{r_{D1}} A_D^{-2} dr_D &= (2r_{Dp} / m_p \lambda)^2 \int_{2r_{Dp}/3}^{\gamma} r_D^{-4} dr_D \\ &= (2 / m_p \lambda)^2 [27 / (8r_{Dp}) - \lambda^3 / r_{Dp}] \end{aligned} \quad (4.55)$$

For low perforation shot densities ($\gamma > v$), the outer radius r_i is equal to $v r_w$.

$$\begin{aligned} \int_{r_{D0}}^{r_{D1}} \frac{dr_D}{A_D} &= \frac{2r_{Dp}}{m_p \lambda} \int_{2r_{Dp}/3}^v \frac{dr_D}{r_D^2} \\ &= (2 / m_p \lambda) (3/2 - r_{Dp} / v) \end{aligned} \quad (4.56)$$

and

$$\begin{aligned} \int_{r_{D0}}^{r_{D1}} A_D^{-2} dr_D &= (2r_{Dp} / m_p \lambda)^2 \int_{2r_{Dp}/3}^v r_D^{-4} dr_D \\ &= (2 / m_p \lambda)^2 (27 / 8r_{Dp} - r_{Dp}^2 / v^3) \end{aligned} \quad (4.57)$$

For the radial flow region induced by the perforation angular distribution, the dimensionless flow area is given by

$$A_D = m_p r_D / 2 \quad (4.58)$$

For $\gamma < v$

$$\begin{aligned}\int_{r_{D1}}^{r_{D2}} A_D^{-1} dr_D &= (2/m_p) \int_{\gamma}^v r_D^{-1} dr_D \\ &= (2/m_p) \ln(v\lambda/r_{Dp})\end{aligned}\quad (4.59)$$

and

$$\begin{aligned}\int_{r_{D1}}^{r_{D2}} A_D^{-2} dr_D &= (2/m_p)^2 \int_{\gamma}^v r_D^{-2} dr_D \\ &= (2/m_p)^2 (\lambda/r_{Dp} - 1/v)\end{aligned}\quad (4.60)$$

The rest of equations are similar to Eqs. B-27, B-29, B-34, and B-35. Changing the notation gives

For $\kappa < v$

$$\int_{r_{D2}}^{r_{D3}} A_D^{-1} dr_D = \ln[r_{Db}/(1+v)] \quad (4.61)$$

$$\int_{r_{D2}}^{r_{D3}} A_D^{-2} dr_D = 1/(1+v) \quad (4.62)$$

For $\kappa > v$

$$\int_{r_{D1}}^{r_{D2}} A_D^{-1} dr_D = \left(\frac{r_{Dp}/\lambda}{r_{Dp} + \lambda - 1} \right) \ln \left[\left(\frac{\lambda + r_{Dp}}{1+v} \right) \left(1 + \frac{v(1-\lambda)}{r_{Dp}} \right) \right] + \ln \left(\frac{r_{Db}}{1 + r_{Dp}/\lambda} \right) \quad (4.63)$$

$$\begin{aligned}\int_{r_{D1}}^{r_{D2}} A_D^{-2} dr_D &= \left[\frac{r_{Dp}/\lambda}{r_{Dp} + \lambda - 1} \right]^2 \left\{ \frac{1}{1+v} - \frac{1}{1 + r_{Dp}/\lambda} + \frac{1-\lambda}{(1-\lambda)v + r_{Dp}} - \frac{\lambda(1-\lambda)}{r_{Dp}} \right. \\ &\quad \left. - \left[\frac{2(1-\lambda)}{r_{Dp} + \lambda - 1} \right] \ln \left[\left(\frac{\lambda + r_{Dp}}{1+v} \right) \left(1 + \frac{v(1-\lambda)}{r_{Dp}} \right) \right] \right\} + \left(\frac{1}{1 + r_{Dp}/\lambda} \right)\end{aligned}\quad (4.64)$$

Consequently, a skin equation for perforated liner completions is obtained by

$$s_{PL} = s_{PL}^0 + f_{t,PL} F_{o,w} \quad (4.65)$$

where

For $\kappa < v$

$$s_{PL}^0 = \left(\frac{2}{m_p \lambda} \right) \left(\frac{3}{2} - \lambda \right) + \left(\frac{2}{m_p} \right) \ln \left(\frac{v\lambda}{r_{Dp}} \right) - \ln(1+v) \quad (4.66)$$

$$f_{t,PL} = \left(\frac{2}{m_p \lambda} \right)^2 \left(\frac{27}{8r_{Dp}} \right) + \left(\frac{2}{m_p} \right)^2 \left(\frac{1}{v} \right) + \frac{1}{1+v} \quad (4.67)$$

For $\gamma \gg v$

$$s_{PL}^0 = \left(\frac{2}{m_p \lambda} \right) \left(\frac{3}{2} - \frac{r_{Dp}}{v} \right) + \left(\frac{r_{Dp} / \lambda}{r_{Dp} + \lambda - 1} \right) \ln \left\{ \left(\frac{\lambda + r_{Dp}}{1 + v} \right) \left(1 + \frac{v(1 - \lambda)}{r_{Dp}} \right) \right\} - \ln \left(1 + \frac{r_{Dp}}{\lambda} \right) \quad (4.68)$$

$$f_{t,PL} = \left(\frac{2}{m_p \lambda} \right)^2 \left(\frac{27}{8r_{Dp}} - \frac{r_{Dp}^2}{v^3} \right) + \left(\frac{r_{Dp} / \lambda}{r_{Dp} + \lambda - 1} \right)^2 \left\{ \frac{1}{1 + v} - \frac{1}{1 + r_{Dp} / \lambda} + \frac{1 - \lambda}{(1 - \lambda)v + r_{Dp}} - \frac{\lambda(1 - \lambda)}{r_{Dp}} - \left[\frac{2(1 - \lambda)}{r_{Dp} + \lambda - 1} \right] \ln \left[\left(\frac{\lambda + r_{Dp}}{1 + v} \right) \left(1 + \frac{v(1 - \lambda)}{r_{Dp}} \right) \right] \right\} + \left(\frac{1}{1 + r_{Dp} / \lambda} \right) \quad (4.69)$$

4.4 EFFECT OF FORMATION DAMAGE ON SLOTTED OR PERFORATED LINERS

In openhole completions, the effect of damage, s_{fo} is classically given by the Hawkins' formula;

$$s_{fo} = (k / k_s - 1) \ln(r_s / r_w) \quad (4.70)$$

where k_s is the permeability in a damage zone and r_s is the radius of this zone. A skin equation which combines the effects of convergent flow and damage is required. Karakas and Tariq (1991) derived a model of the interactions of these effects for cased and perforated wells. Following their work, a skin equation for slotted liner completions inside a damaged zone can be obtained. In the following analysis, we assume two concentric annular regions of permeabilities k_s and k (Fig. 4.11). We presume that radial flow occurs at the boundary between the damaged and undamaged region. With this assumption, the total pressure drop can be separated into

$$\Delta p = \Delta p_1 + \Delta p_2 \quad (4.71)$$

Assuming Darcy flow, the pressure drop inside the damage zone is given by

$$\Delta p_1 = \frac{q\mu}{2\pi k_s L} \left(\ln \frac{r_s}{r_w} + s_{L,r}^0 \right) \quad \text{for } r_w < r < r_s \quad (4.72)$$

where $s_{L,r}^0$ is the rate-independent skin factor for a slotted or perforated liner (excluding a plugging skin factor). For outside the damage zone,

$$\Delta p_2 = \frac{q\mu}{2\pi k L} \ln \frac{r_b}{r_s} \quad \text{for } r_s < r < r_b \quad (4.73)$$

From the definition of skin, the total pressure drop can be also written by

$$\Delta p = \frac{q\mu}{2\pi k L} \left(\ln \frac{r_b}{r_w} + s \right) \quad (4.74)$$

Substituting Eqs. 4.72, 4.73 and 4.74 into Eq. 4.71 and simplifying the equation give

$$s = s_{fo} + s_{L,r}^0 / k_{Ds} \quad (4.75)$$

Eq. 4.75 show that the flow convergence skin and formation damage skin factors can not be explicitly separated. Formation damage around a liner causes the conventional damage skin factor, s_{fo} , (characterized by the Hawkins' formula) but also amplifies the liner geometry skin. Fig. 4.12 shows the verification of the assumption made in the derivation of the skin model (Eq. 4.75). The model gives very good matches with FEM simulation results except for extremely shallow penetration damage ($r_s \approx r_w$).

For an elliptic damage region in an anisotropic formation,

$$s_{fo} = (k_{Ds}^{-1} - 1) \ln \left\{ \frac{1}{I_{ani} + 1} \left[\frac{r_{sH}}{r_s} + \sqrt{\left(\frac{r_{sH}}{r_s} \right)^2 + I_{ani}^2 - 1} \right] \right\} \quad (4.76)$$

where r_{sH} is the damage penetration in the horizontal direction (y-direction).

The rate-dependent skin factor is also affected by formation damage. According to Eq. 2.39, integration along the flowpath with a changing dimensionless high-velocity coefficient will give an accurate turbulence scale factor. But for simplicity, we presume that the entire turbulent scale factor in the region will be simply amplified by β_{Ds} ($=\beta_s/\beta$) as follows:

$$f_t = \beta_{Ds} f_{t,L} \quad (4.77)$$

Since the turbulence scale factor is dominated around the narrowest flow area, it becomes more important closer to slots or perforations. Consequently, Eq. 4.77 will provide a good approximation. A skin equation for slotted or perforated liners within a damaged zone can be presented in the form of

$$s_L = s_{fo} + s_L^0 / k_{Ds} + \beta_{Ds} f_{t,L} F_{o,w} \quad (4.78)$$

for slots plugged by formation sand so that $k_s = k$,

$$s_{SL} = s_{fo} + s_{SL,\ell}^0 + s_{SL,r}^0 / k_{Ds} + (f_{t,SL,\ell} + \beta_{Ds} f_{t,SL,r}) F_{o,w} \quad (4.79)$$

The important fact is that the effect of formation damage on slotted liner completions is even worse than openhole completions. The reduced permeability region magnifies the skin due to the convergent flow inside the damaged zone. For example, with $s_{SL,r}^0 = 2.0$ inside the damage zone where the permeability is 10% of the original formation, the resultant skin factor is 20 larger than one obtained by Eq. 4.70. In addition, since the third term of Eq. 4.79 is independent of the damage radius, the effect of formation damage on slotted liner completions is substantial even for shallow penetration of damage.

Table. 4.1 Numerical data for Fig. 4.12.

r_s	FEM			Model		
ft	$m_s=4$	$m_s=8$	$m_s=12$	$m_s=4$	$m_s=8$	$m_s=12$
0.300	2.5	1.1	0.7	25.0	10.8	6.5
0.305	14.2	6.9	4.5	25.2	10.9	6.7
0.310	17.2	8.4	5.5	25.3	11.1	6.8
0.320	20.2	9.9	6.5	25.6	11.4	7.1
0.330	21.9	10.8	7.1	25.9	11.6	7.4
0.360	24.8	12.2	8.1	26.7	12.4	8.2
0.400	26.8	13.3	9.1	27.6	13.4	9.1
0.500	29.5	15.4	11.1	29.6	15.4	11.1
0.700	32.6	18.4	14.1	32.6	18.4	14.1
1.000	35.8	21.6	17.3	35.8	21.6	17.3

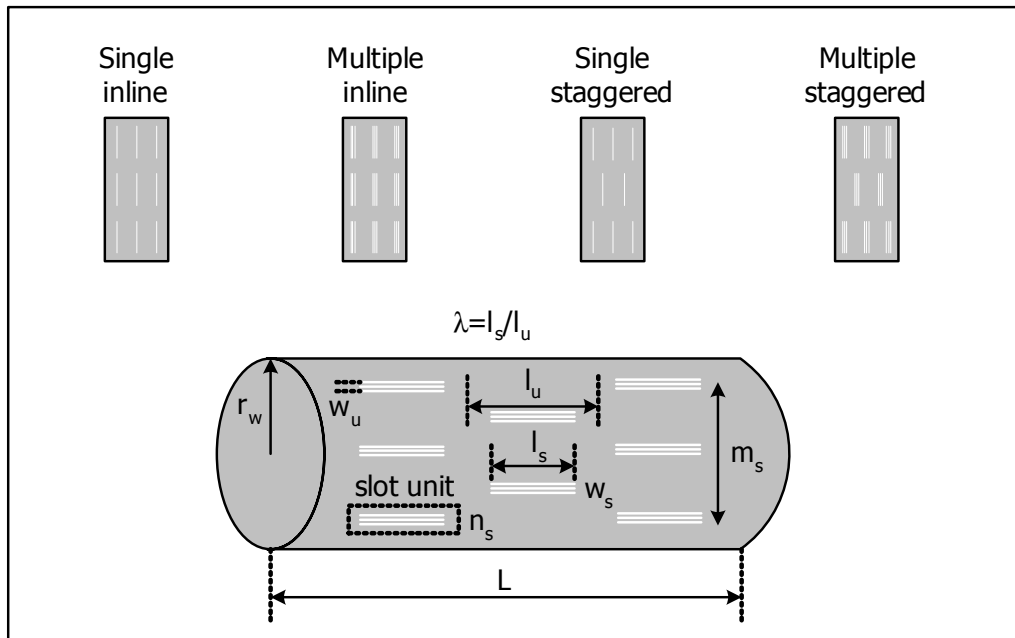


Fig. 4.1 Geometric variables for slotted liner skin calculation.

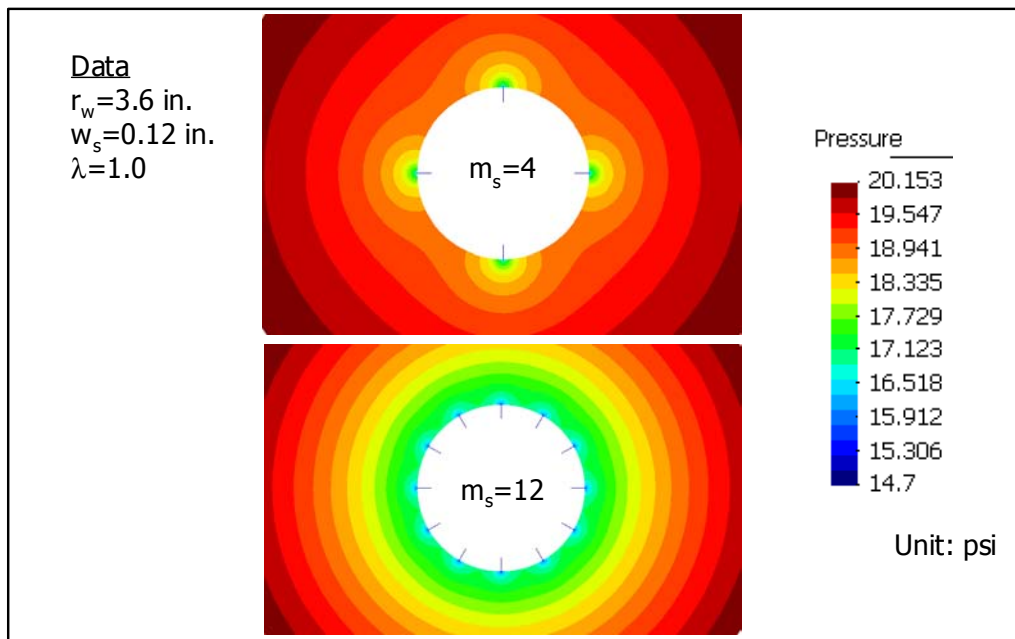


Fig. 4.2 2D pressure contour fill of single inline slotted liners.

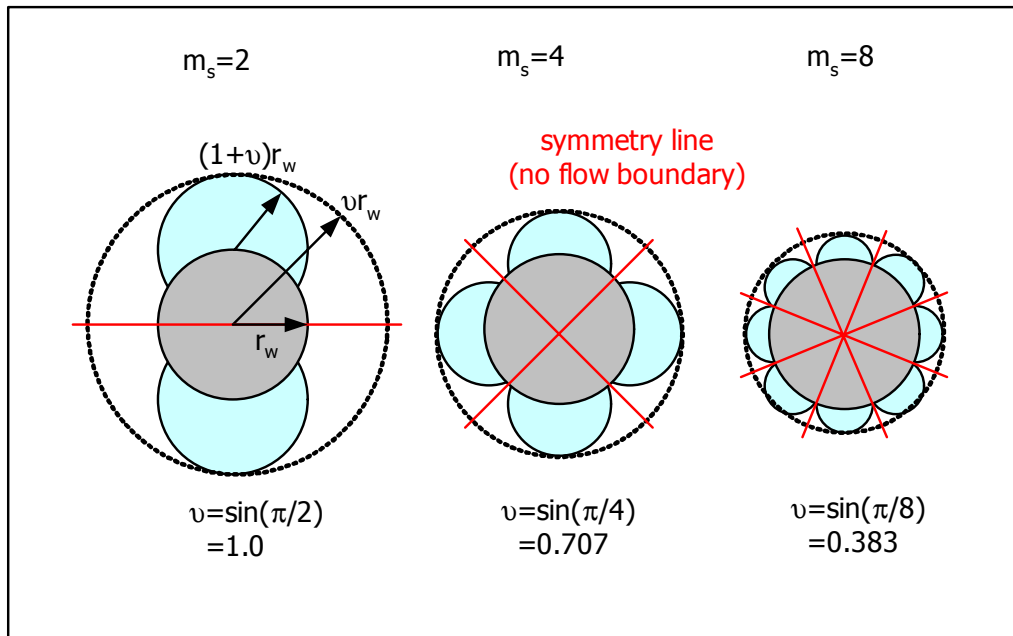


Fig. 4.3 Determination of the outer radius of slot-induced radial flow.

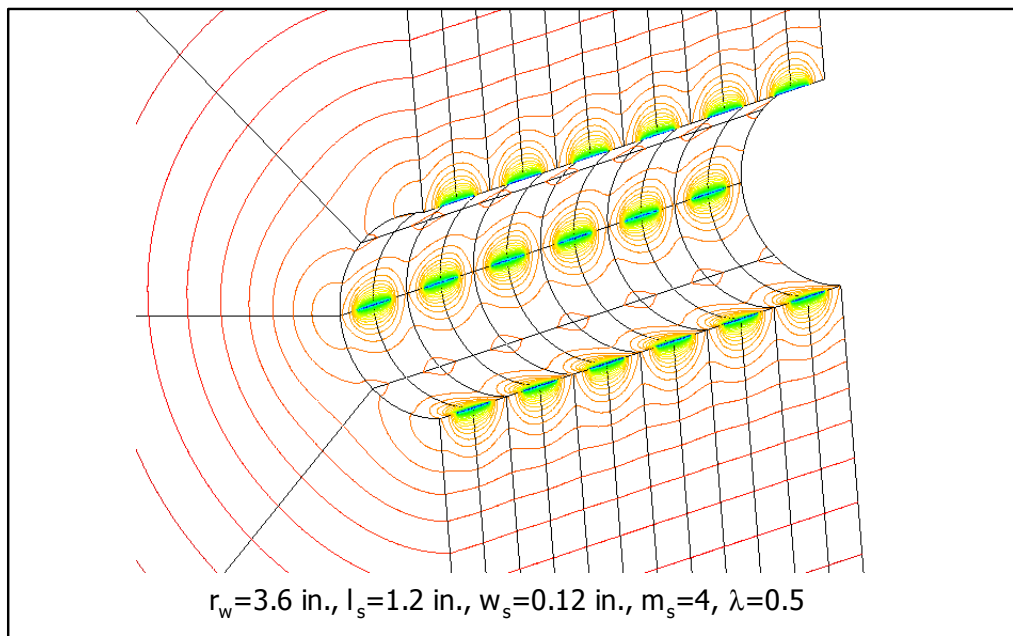


Fig. 4.4 3D pressure contour lines of a single inline slotted liner.

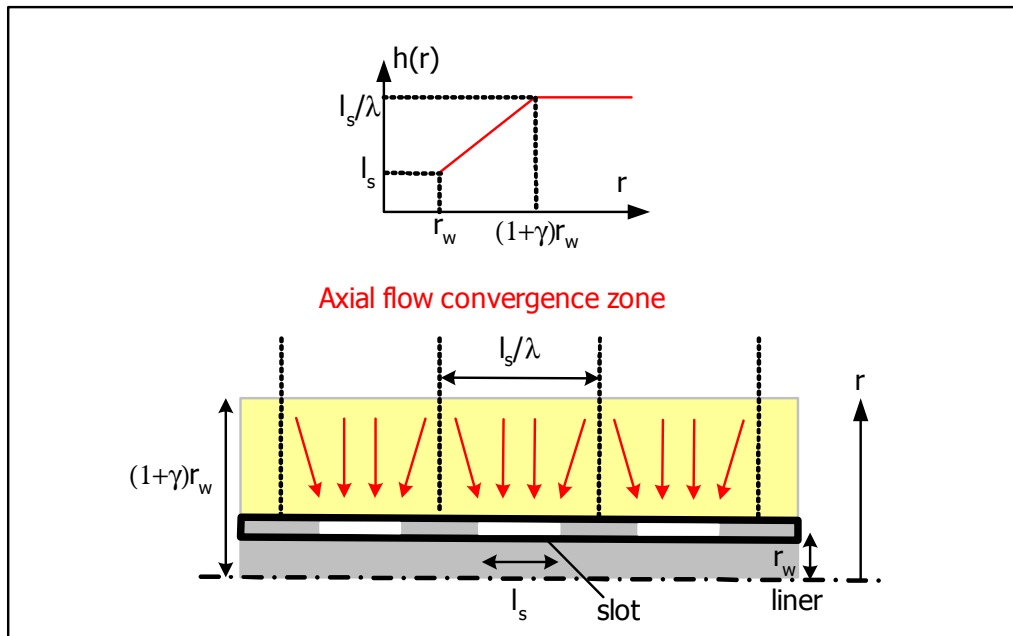


Fig. 4.5 Approximation of the axial flow convergence.

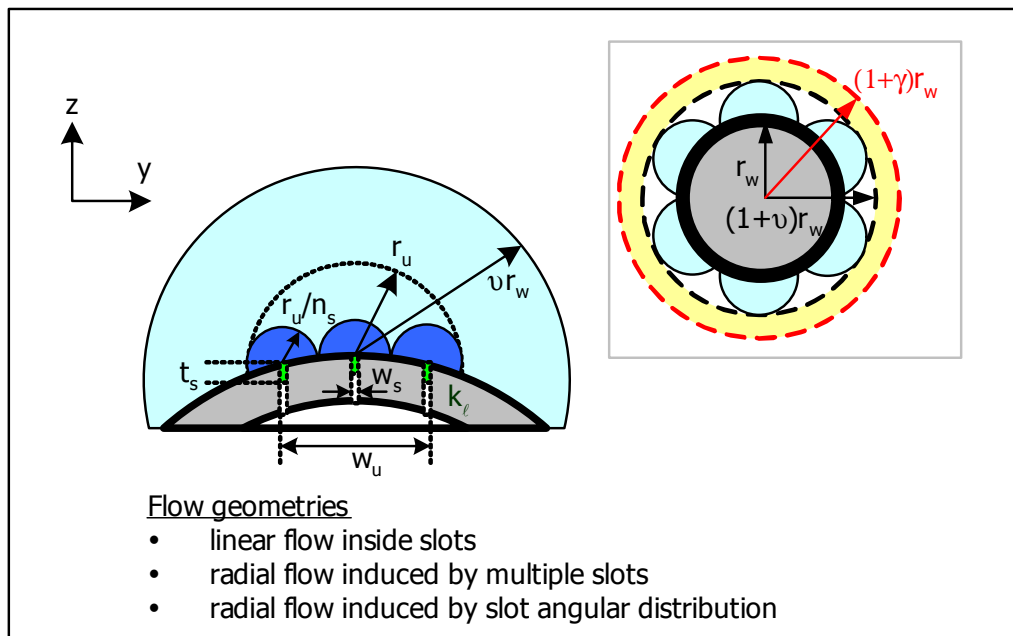


Fig. 4.6 Flow geometries around a slotted liner.

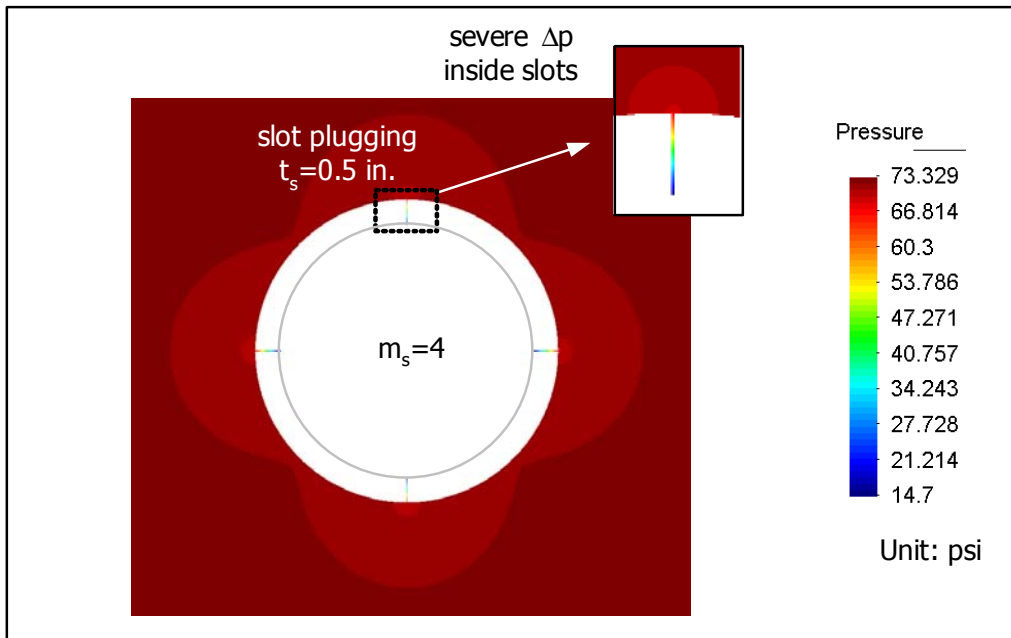


Fig. 4.7 Pressure contour fill of slots filled by formation sand.

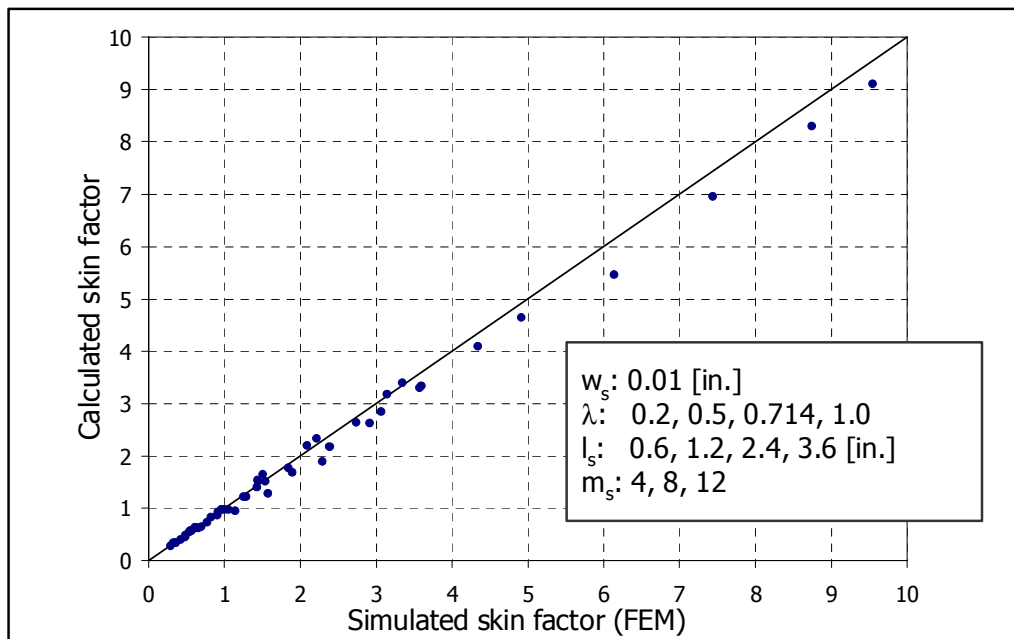


Fig. 4.8 Comparison with FEM simulation results, single staggered slotted liners.

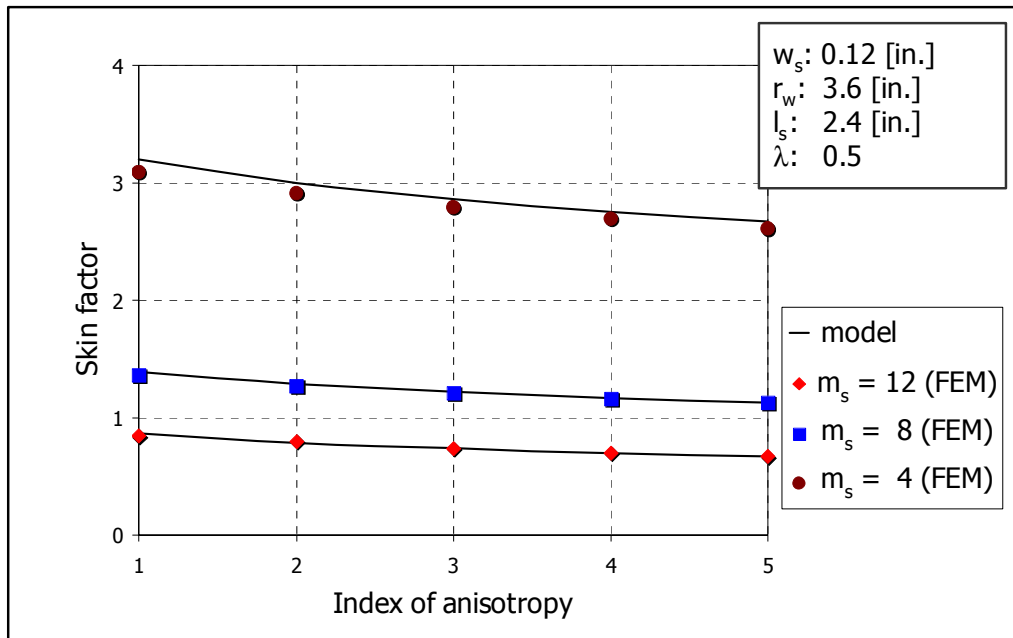


Fig. 4.9 Slotted liner skin factors in anisotropic formation.

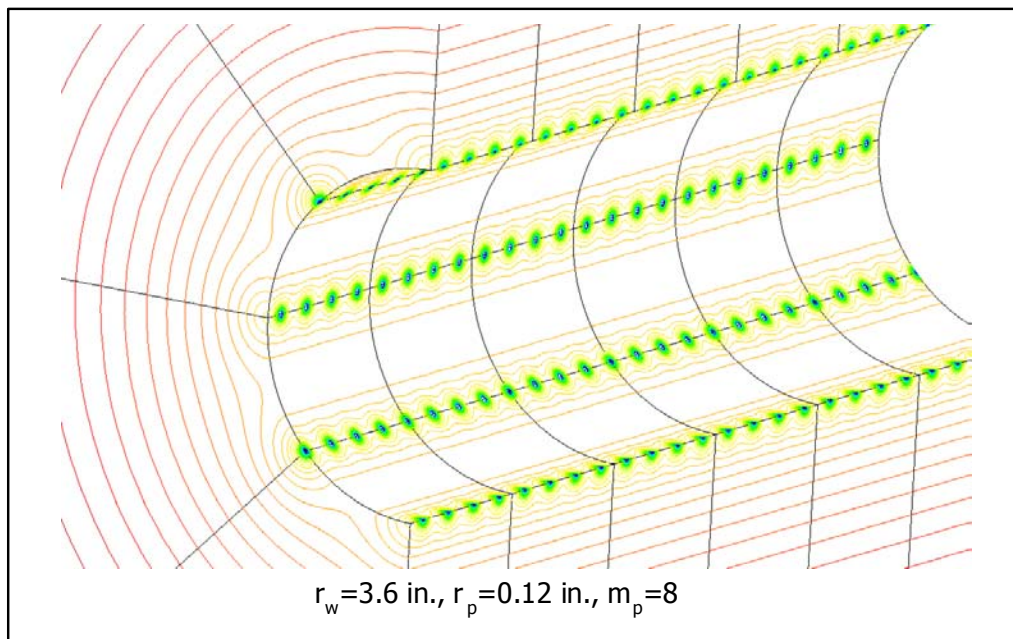


Fig. 4.10 3D pressure contour lines of a perforated liner.

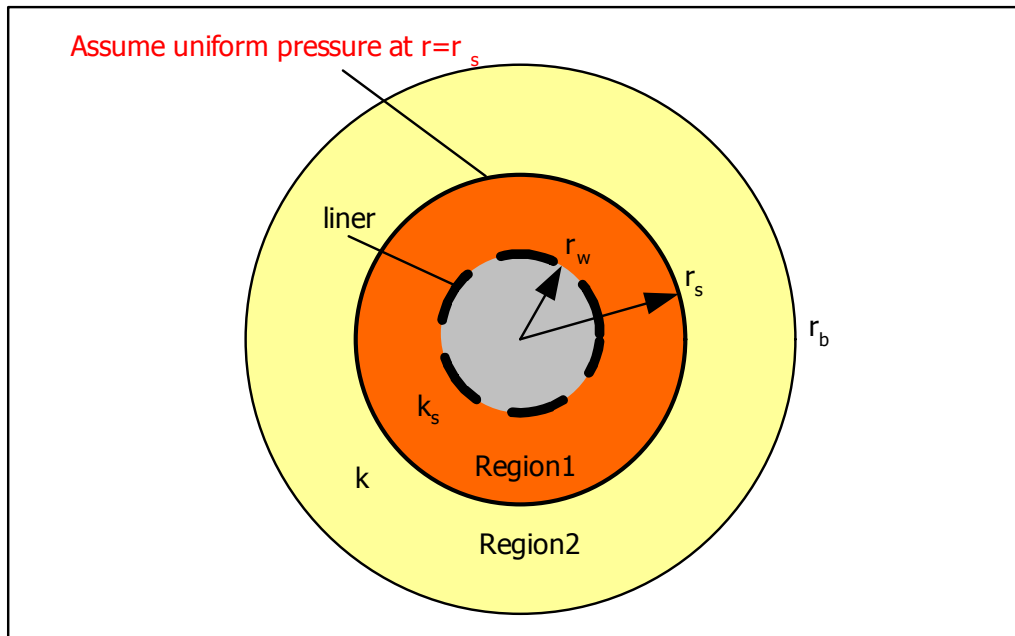


Fig. 4.11 Cross section of a liner inside a damage zone.

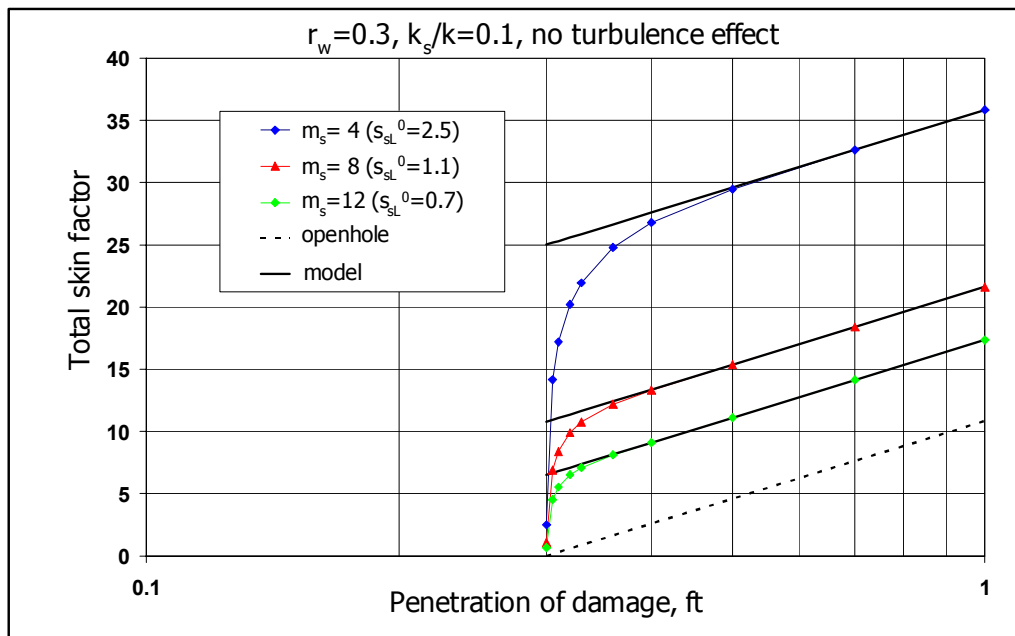


Fig. 4.12 Verification of the assumption used in Eq. 4.75.

CHAPTER 5

Cased and Perforated Wells

5.1 INTRODUCTION TO CASED AND PERFORATED WELLS

Perforating is also a commonly practiced method for horizontal well completion. Perforation is the communication tunnel extending beyond the casing or liner into the reservoir formation, through which oil or gas is produced. In most cases, a high penetration is desirable to create effective flow communication to the part of the formation that has not been damaged by the drilling or completion processes. The perforation shot densities are the number of perforations per liner foot, which is often referred to spf (shots per foot). In general, productivity is improved with increasing shot density. Perforation phasing is the radial distribution of successive perforating charges around the circumference of the casing or liner. Perforating gun assemblies are commonly available in 0-, 180-, 120-, 90- and 60- degree phasing. Perforating processes produces a crushed zone around the perforation in which permeability may be reduced substantially below that of the original formation. Estimates based on flow calculations suggest that the permeability of the compacted zone is about 20% of the original formation permeability and can be a very serious impediment to productivity (Locke, 1981).

5.2 DEVELOPMENT OF A SKIN EQUATION FOR CASED AND PERFORATED WELLS

Fig. 5.1 shows the key parameters of a perforated completion presumed in this study. The horizontal well is assumed to be on the x -axis and perpendicular to the y - and z - axis. In formations with no significant formation damage or perforation damage, the perforation

skin is a function of the number of perforations per plane, m_p , analogous to angular phasing, θ , in Karakas and Tariq's model (Karakas and Tariq, 1991); perforation length, l_p ; perforation radius, r_p ; perforation shot density, n_p (or spacing between perforations along a well, h_p); wellbore radius, r_w ; the principal permeabilities, k_x , k_y , k_z ; and perforation orientation, α , defined by the angle between the perforation direction and the maximum permeability direction.

The most important and significant difference between perforation skin models for vertical and horizontal wells is the effect of perforation orientation. For a horizontal well completed in a highly anisotropic reservoir, the perforation skin factor is greatly influenced by α .

Following Karakas and Tariq's model, we divided the perforation skin into three components; the 2D plane flow skin factor, s_{2D} ; the wellbore blockage skin factor, s_{wb} ; and the 3D convergence skin factor s_{3D} . The total (rate-independent) perforation skin factor is then given by

$$s_P^0 = s_{2D} + s_{wb} + s_{3D} \quad (5.1)$$

2D plane flow skin. s_{2D} is a skin factor that accounts for flow in the y-z plane without the existence of the wellbore. The plane flow problem is considered as infinite perforation shot density along the well, and under most practical perforation lengths and well radii ($l_p > 3$ in. and $r_w < 10$ in.) any convergence effect in the direction along the wellbore (x-direction in this work) can be neglected (This effect is included in 3D convergence flow skin). With this consideration, the 2D plane flow behavior into perforations is quite similar to that of an infinite conductivity fractured well. This skin factor can be negative or positive depending on the perforation conditions and the reservoir anisotropy. Under plane flow conditions and assuming negligible wellbore effects, we can introduce the

effective-well-radius concept (Fig. 5.2), developed by Prats (1961) for vertically fractured wells. According to his work, the effective well radius is given by the quarter of the total fracture length for a single fracture without a pressure drop inside fracture. Due to the geometric similarity between a unidirectional perforation ($m_p=1$) and a fracture, the perforation skin factor can be analytically derived by

$$\begin{aligned} s_{2D} &= \ln(4r_w/l_p) \\ &= \ln(4/l_{Dp}) \quad \text{for } m_p=1 \end{aligned} \quad (5.2)$$

where l_{Dp} is the dimensionless perforation length.

$$l_{Dp} = l_p / r_w \quad (5.3)$$

As m_p approaches infinity (Fig. 5.2), the effective well radius approaches r_w+l_p . The 2D plane flow skin factor is then analytically given by

$$\begin{aligned} s_{2D} &= \ln\left(\frac{r_w}{r_w+l_p}\right) \\ &= \ln\left(\frac{1}{1+l_{Dp}}\right) \quad \text{for } m_p=\infty \end{aligned} \quad (5.4)$$

For other values of m_p such as $m_p=2, 3, 4, 6$, and 8 , the skin factors should range between those given by Eqs. 5.2 and 5.4. Fig. 5.3 shows FEM simulation results for different perforation phasings. According to these plots, s_{2D} can be approximately given by the following interpolation;

$$s_{2D} = a_m \ln\left(\frac{4}{l_{Dp}}\right) + (1-a_m) \ln\left(\frac{1}{1+l_{Dp}}\right) \quad (5.5)$$

where a_m is a constant given in Table 1 for different values of m_p . In this study, the numerical values for a_m were obtained through FEM simulations for all the phasings except for $m_p=1$ and ∞ . As shown in Fig. 5.3, the interpolation function given by Eq. 5.5 matches the FEM results almost exactly.

The performance of perforated completions in anisotropic reservoirs is greatly influenced by the azimuth of the perforation (the angle between the perforation tunnel and the maximum permeability direction, usually thought to be the horizontal direction). Fig. 5.4 shows the impact of perforation orientation, α , on s_{2D} . For particular conditions ($l_{dp} = 1.0$ and $\sqrt{k_y/k_z} = 5$), the perforation skin factor was reduced from 2.48 to 0.88 for $m_p = 1$ and from 1.17 to -0.56 for $m_p = 2$ by changing the orientation from horizontal ($\alpha = 0^\circ$) to vertical ($\alpha = 90^\circ$). The contrast of skin factor will increase for a higher anisotropy ratio.

For $m_p = 1$, we can analytically calculate skin factor by using a coordinate transformation into the equivalent isotropic space. The effective perforation length and the equivalent wellbore radius are given by

$$l_{p,eff} = l_p (\sqrt{k_y/k_z} \sin^2 \alpha + \sqrt{k_z/k_y} \cos^2 \alpha)^{0.5} \quad (5.6)$$

$$r_{w,eq} = r_w [\sqrt[4]{k_y/k_z} + \sqrt[4]{k_z/k_y}] / 2 \quad (5.7)$$

Substituting the above equations into Eq. 5.2 gives

$$s_{2D} = \ln \left(\frac{4}{l_{dp}} \right) + \ln \left[\frac{\sqrt{k_y/k_z} + 1}{2(\cos^2 \alpha + (k_y/k_z) \sin^2 \alpha)^{0.5}} \right] \quad (5.8)$$

where the second term represents the effect of the reservoir anisotropy and perforation orientation. For a fixed perforation orientation (constant α), the reservoir anisotropy makes the skin factor simply move up or down, depending on the orientation. As α approaches zero degrees (the direction of the maximum permeability), the perforation skin increases. On the other hand, as α approaches 90° (the direction of the minimum permeability), the perforation skin decreases.

Similarly to $m_p = 1$, the 2D plane flow skin equation for $m_p = 2$ in an anisotropic medium is approximately given by

$$s_{2D} = a_2 \ln\left(\frac{4}{l_{Dp}}\right) + (1-a_2) \ln\left(\frac{1}{1+l_{Dp}}\right) + \ln\left[\frac{\sqrt{k_y/k_z} + 1}{2(\cos^2 \alpha + (k_y/k_z) \sin^2 \alpha)^{0.5}}\right] \quad (5.9)$$

As shown in Fig. 5.5, Eq. 5.9 shows good agreement with the FEM simulation results.

For multidirectional perforation phasings ($m_p \geq 3$), the estimation of the effective well radius is not simple because the coordinate transformation into an equivalent isotropic system gives different effective perforation lengths for each direction. According to the FEM simulation results (Fig. 5.4), the influence of permeability anisotropy and hence the orientation for $m_p \geq 3$ is not as significant as those for $m_p = 1$ and 2. Therefore we can conclude that the effect of the reservoir anisotropy and the perforation orientation for $m_p \geq 3$ are negligible and Eq. 5.5 is directly applied even for an anisotropic medium.

Consequently, the 2D plane flow skin equation can be summarized as

For $m_p < 3$

$$s_{2D} = a_m \ln\left(\frac{4}{l_{Dp}}\right) + (1-a_m) \ln\left(\frac{1}{1+l_{Dp}}\right) + \ln\left[\frac{\sqrt{k_y/k_z} + 1}{2(\cos^2 \alpha + (k_y/k_z) \sin^2 \alpha)^{0.5}}\right] \quad (5.10)$$

For $m_p \geq 3$

$$s_{2D} = a_m \ln\left(\frac{4}{l_{Dp}}\right) + (1-a_m) \ln\left(\frac{1}{1+l_{Dp}}\right) \quad (5.11)$$

Wellbore blockage skin. s_{wb} is also estimated for the 2D plane flow geometry. Due to the distortion of the flow into the perforation by the presence of the wellbore (Fig. 5.6), perforation skin factors with the wellbore included will be greater than those given by s_{2D} . This wellbore blockage effect can be quite significant, especially for $m_p = 1$. As a result of the additional pressure drop, well productivity would be less than that estimated only

with s_{2D} . Thus, this effect can be quantified in terms of a wellbore pseudoskin, s_{wb} , which is always positive:

$$s_P = s_{2D} + s_{wb} \quad (5.12)$$

Similarly to s_{2D} , the wellbore blockage effect will depend on the dimensionless perforation length, l_{Dp} , the perforation orientation, α , and the anisotropy ratio, $\sqrt{k_y/k_z}$.

For isotropic reservoirs, s_{wb} is assumed to depend only on the dimensionless perforation length. Fig. 5.7 illustrates this dependency for the case of $m_p=1, 2, 3$ and 4. Wellbore blockage skin factors for a given dimensionless perforation length is significantly larger for $m_p=1$ than those for other cases ($m_p=2, 3$, and 4). By comparing with the FEM simulation results, we find that the wellbore blockage skin, s_{wb} , can be closely approximated by

$$s_{wb} = b_m \ln\{c_m / l_{Dp} + \exp[-c_m / l_{Dp}]\} \quad (5.13)$$

where b_m and c_m are empirical constants given in Table 2.

For anisotropic reservoirs (Fig. 5.8), s_{wb} depends also on the perforation orientation and the reservoir anisotropy. To derive a wellbore blockage skin equation taking into account the effect of perforation orientation, a coordinate transformation into the equivalent isotropic space is applied. The effective perforation length is now given by Eq. 5.6. We concluded that the effective wellbore radius (the barrier height) would be a key parameter, which can be transformed as

$$\begin{aligned} r_{w,eff} &= r_w [\sqrt{k_y/k_z} \sin^2(\alpha + \pi/2) + \sqrt{k_z/k_y} \cos^2(\alpha + \pi/2)]^{0.5} \\ &= r_w [\sqrt{k_z/k_y} \sin^2 \alpha + \sqrt{k_y/k_z} \cos^2 \alpha]^{0.5} \end{aligned} \quad (5.14)$$

From Eqs. 5.6 and 5.14, the ratio of the effective perforation length to the effective well radius can be calculated by

$$l_{p,eff} / r_{w,eff} = l_{Dp} \mathcal{X} \quad (5.15)$$

in which

$$\chi = \sqrt{\frac{(k_y / k_z) \sin^2 \alpha + \cos^2 \alpha}{(k_y / k_z) \cos^2 \alpha + \sin^2 \alpha}} \quad (5.16)$$

where χ is a empirical parameter to account for the effect of the reservoir anisotropy and perforation orientation. Compared with the simulation results, a good agreement (Fig. 5.9) was obtained by setting the effective dimensionless perforation length as

$$l_{Dp,eff} = l_{Dp} \chi^{1.35} \quad \text{for } m_p=1 \quad (5.17)$$

The wellbore blockage skin is calculated by inserting Eq. 5.17 into Eq. 5.13. Fig. 5.10 shows FEM simulation results for $m_p=2$. χ is empirically set as

$$\chi = [(k_y / k_z) \cos^2 \alpha + \sin^2 \alpha]^{-0.5} \quad (5.18)$$

and the effective dimensionless perforation length is empirically estimated by

$$l_{Dp,eff} = l_{Dp} \chi^{1.25} \quad \text{for } m_p=2 \quad (5.19)$$

As shown in Fig. 5.8, the effect of perforation orientation for $m_p \geq 3$ is comparatively small, that is, the effect of anisotropy is not significant. We can conclude that the wellbore skin equation for $m_p \geq 3$ is independent of the reservoir anisotropy and α . Consequently, the wellbore blockage skin correlation equation can be summarized by

$$s_{wb} = b_m \ln \{c_m / l_{Dp,eff} + \exp[-c_m / l_{Dp,eff}]\} \quad (5.20)$$

For $m_p=1$,

$$l_{Dp,eff} = l_{Dp} \left[\frac{(k_y / k_z) \sin^2 \alpha + \cos^2 \alpha}{(k_y / k_z) \cos^2 \alpha + \sin^2 \alpha} \right]^{0.675} \quad (5.21)$$

For $m_p=2$,

$$l_{Dp,eff} = l_{Dp} \left[\frac{1}{(k_y / k_z) \cos^2 \alpha + \sin^2 \alpha} \right]^{0.625} \quad (5.22)$$

For $m_p \geq 3$,

$$l_{Dp,eff} = l_{Dp} \quad (5.23)$$

3D convergence flow skin. According to Karakas and Tariq's correlation equations, an additional 3D convergence flow skin factor is estimated based on the following two dimensionless parameters;

$$h_{De} = h_{eff} / l_{p,eff} \quad (5.24)$$

$$r_{De} = r_{p,eff} / h_{eff} \quad (5.25)$$

Appropriate coordinate transformations give the effective perforation spacing, perforation length and perforation radius.

$$h_{eff} = h \sqrt{\bar{k} / k_x} \quad (5.26)$$

$$l_{p,eff} = l_p \sqrt{(\bar{k} / k_y) \cos^2 \alpha + (\bar{k} / k_z) \sin^2 \alpha} \quad (5.27)$$

where

$$\bar{k} = \sqrt[3]{k_x k_y k_z} \quad (5.28)$$

An additional consideration is needed to estimate the effective perforation radius. Fig. 5.11 shows a perforation in an anisotropic reservoir. The circular perforation is assumed to lie at an arbitrary azimuth with respect to the maximum and minimum principle axes of permeability. The axis of the perforation lies at an angle α to the y-axis. To specify the problem completely in the equivalent isotropic system, we must also transform the perforation cylinder. The perforation in the anisotropic system is considered as a right circular cylinder. In the equivalent isotropic system, the cylinder becomes an elliptical cylinder, with the base no longer perpendicular to the axis. We approximate this ellipse by a right ellipse that has the same perpendicular cross section, but whose length is given by Eq. 5.27. The vertical semi-axis of the elliptical cross section, a_w , is given by

$$a_w = r_p \sqrt{\bar{k} / k_x} \quad (5.29)$$

If we transform the original circular cross section, the horizontal semi-axis becomes

$$w = r_p \sqrt{(\bar{k} / k_y) \sin^2 \alpha + (\bar{k} / k_z) \cos^2 \alpha} \quad (5.30)$$

However, this is not the horizontal semi-axis of the transformed elliptical cylinder, because after the transformation the original circular cross section is no longer perpendicular to the axis of the cylinder. Thus, we must find the projection of the distance given in Eq. 5.30 along a direction perpendicular to the axis of the transformed perforation. The axis of the transformed perforation lying at an angle α' to the y' axis is given by

$$\alpha' = \arctan[\sqrt{k_y/k_z} \tan \alpha] \quad (5.31)$$

The transform of the original circular cross section lies at an angle α'' to the z' axis, where α'' is given by

$$\alpha'' = \arctan[\sqrt{k_z/k_y} \tan \alpha] \quad (5.32)$$

The desired cross section of the transformed perforation lies at an angle α' to the z' axis. Thus, we must project the distance given in Eq. 5.30 through an angle $\alpha'' - \alpha'$. Finally, we obtain the required semi-axis of the elliptical cross section of the transformed perforation from

$$b_w = r_p \cos(\alpha'' - \alpha') \sqrt{[(\bar{k}/k_y) \sin^2 \alpha + (\bar{k}/k_z) \cos^2 \alpha]} \quad (5.33)$$

Kucuk and Brigham (1979) showed that the equivalent wellbore radius for an elliptical wellbore having semi-axis a_w and b_w is given by the arithmetic mean. Similarly, the perforation radius is given by

$$r_{p,eff} = \frac{r_p}{2} \left[\sqrt{\left(\frac{\bar{k}}{k_y} \sin^2 \alpha + \frac{\bar{k}}{k_z} \cos^2 \alpha \right)} \cos(\alpha'' - \alpha') + \sqrt{\frac{\bar{k}}{k_x}} \right] \quad (5.34)$$

Then Eqs. 5.24 and 5.25 for anisotropic media are given by

$$h_{De} = \frac{h}{l_p \sqrt{(k_x/k_z) \sin^2 \alpha + (k_x/k_y) \cos^2 \alpha}} \quad (5.35)$$

$$r_{De} = \frac{r_p}{2h} \left[\sqrt{\left(\frac{k_x}{k_y} \sin^2 \alpha + \frac{k_x}{k_z} \cos^2 \alpha \right)} \cos(\alpha'' - \alpha') + 1 \right] \quad (5.36)$$

From Karakas and Tariq's correlation equations, s_{3D} is given by

$$s_{3D} = 10^{\beta_1} h_{De}^{\beta_2-1} r_{De}^{\beta_2} \quad (5.37)$$

with

$$\beta_1 = d_m \log r_{De} + e_m \quad (5.38)$$

$$\beta_2 = f_m r_{De} + g_m \quad (5.39)$$

The numerical values of d_m , e_m , f_m , and g_m are obtained from Table 3 developed by Karakas and Tariq (1991). As we discussed in the 2D perforation skin analysis, the effect of perforation orientation and the reservoir anisotropy for $m_p \geq 3$ is not significant and can be neglected. Hence Eq. 5.35 and 5.36 can be simplified to

$$h_{De} = \frac{h}{l_p} \left(\frac{\sqrt{k_y k_z}}{k_x} \right)^{0.5} \quad (5.40)$$

$$r_{De} = \frac{r_p}{2h} \left[\left(\frac{k_x}{\sqrt{k_y k_z}} \right)^{0.5} + 1 \right] \quad (5.41)$$

These equations can be used to estimate the perforation skin factor for most practical ranges of system parameters ($h_{De} \leq 10$ and $r_{De} \geq 0.01$).

The turbulence scale factor for cased and perforated wells is estimated by introducing the approximated flow geometry shown in Fig. 5.12. From the definition of skin factor, $f_{t,p}$ is given by the integration form of:

$$\begin{aligned} f_{t,p} &= \int_{\xi_{D0}}^{\xi_{D1}} A_D^{-2} d\xi_D \\ &= \int_{r_{D1}} A_D^{-2} dr_D + \int_{r_{D2}} A_D^{-2} dr_D \end{aligned} \quad (5.42)$$

The integration interval is now divided into two parts. r_{D1} and r_{D2} denote the radial flow in the near-perforation vicinity and the radial flow away from the well. The flow area function, $A(r)$ in the near-perforation vicinity is given by a function of a distance from a perforation

$$A(r) = (2\pi r l_p) N_p \quad (5.43)$$

where N_p is the total number of perforations. The dimensionless flow area A_D becomes

$$\begin{aligned} A_D &= A / (2\pi r_w L) \\ &= r l_p N_p / r_w L \\ &= r_D l_{Dp} / h_{Dp} \end{aligned} \quad (5.44)$$

The integration for r_{D1} can be solved by

$$\begin{aligned} \int_{r_{Dp}}^{h_{Dp}/2} A_D^{-2} dr_D &= (h_{Dp} / l_{Dp})^2 \int_{r_{Dp}}^{h_{Dp}/2} r_D^{-2} dr_D \\ &= (h_{Dp} / l_{Dp})^2 (1 / r_{Dp} - 2 / h_{Dp}) \\ &= (h_{De} / l_{Dp}) (1 / r_{De} - 2) \end{aligned} \quad (5.45)$$

The flow geometry away from the well reduces to radial flow toward to the wellbore.

Similarly to Eq. 3.2 the integration can be written as

$$\int_{r_{D2}} A_D^{-2} dr_D = \int_{r_{D2}} r_D^{-2} dr_D \quad (5.46)$$

It is assumed that the turbulence scale factor is similar to that of an openhole completion (i.e., $f_{t,o}=1$).

$$\int_{r_{D2}} A_D^{-2} dr_D \approx 1 \quad (5.47)$$

From Eqs. 5.42, 5.45, and 5.47, the turbulence scale factor can be approximately given by

$$f_{t,p} = 1 + (h_{De} / l_{Dp}) (1 / r_{De} - 2) \quad (5.48)$$

The approximated flow geometry, where Eq. 5.48 is derived, neglects the effect of perforation phasing and the wellbore blockage effect. Fig. 5.13 shows the comparison with FEM simulation results. For lower perforation shot densities (1 SPF), $f_{t,p}$ for $m_p=1$ is higher than one obtained by Eq. 5.48 due to the wellbore blockage effect. For higher perforation shot densities, the variation of $f_{t,p}$ for different perforation phasings is not significant. Some other cases are also compared in Table 5.5 for $m_p=1$.

For anisotropic formations, the dimensionless parameters, h_{De} and r_{De} are given by Eqs. 5.35, 5.36, 5.40 and 5.41 depending on m_p . l_{Dp} is also evaluated in the equivalent isotropic system. Eq. 5.48 becomes

For $m_p=1$ and 2,

$$f_{t,P} = 1 + \left[\frac{h_{De} (1 + \sqrt{k_y / k_z})}{2l_{Dp} \sqrt{\cos^2 \alpha + (k_y / k_z) \sin^2 \alpha}} \right] \left(\frac{1}{r_{De}} - 2 \right) \quad (5.49)$$

and for $m_p \geq 3$,

$$f_{t,P} = 1 + (h_{De} / l_{Dp}) (1 / r_{De} - 2) \quad (5.50)$$

5.3 EFFECT OF FORMATION DAMAGE ON CASED AND PERFORATED WELLS.

In this section, we extend the model to account for formation damage effects. A skin equation for cased and perforated wells without formation damage can be presented by

$$s_P = s_P^0 + f_{t,P} F_{o,w} \quad (5.51)$$

where s_P^0 can be obtained by the skin equation presented in the previous section. When the perforations terminate inside the damage zone (Fig. 5.14), the reduced permeability magnifies the perforation skin factor and its effect is similar to that of slotted liners, which can be expressed as

$$s_P = s_{f0} + (k / k_s) s_P^0 + (\beta_s / \beta) f_{t,P} F_{o,w} \quad (5.52)$$

where s_{f0} is defined in Eq. 4.70. As Klotz (1974) and Hong (1975) discussed, the influence of a damaged zone on skin in perforated completions depends greatly on the relative position of the perforations with respect to the damaged-zone radius, which can be taken into account for:

$$s_P = s_{f0} + (k / k_s) (s_P^0 + s_x) + (\beta_s / \beta) f_{t,P} F_{o,w} \quad (5.53)$$

where s_x is pseudoskin to account for boundary effects for perforations terminating close to the damaged-zone boundary. s_x is usually negligible unless $m_p=1$ because of the symmetries of the particular flow geometries (Fig. 5.15) so that we can consider $s_x=0$ for $m_p > 1$. This observation may not be true at high dimensionless perforation spacings, h_{De} (low perforation shot densities and short perforation lengths) since each perforation

becomes independent and can be considered as a series of unidirectional phased ($m_p=1$) perforations. Similarly to Muskat's off-centered-well solutions (Muskat, 1949), s_x may be approximated by

$$s_x \cong \ln[1 - r_{Dc}^2] \quad (5.54)$$

where r_{Dc} is the dimensionless off-centered perforation position. In Karakas & Tariq's work, r_{Dc} is defined by

$$r_{Dc} = \frac{1}{r_s} \left(r_w + \frac{L_p}{2} \right) \quad (5.55)$$

As shown in Fig. 5.16, the application of Eq. 5.55 may result in inconsistent skin values (negative skin for formation damage) for some cases ($r_s \approx r_w + l_p$ and $k_s \approx k$).

To differentiate the contribution of the formation damage, s_{fd} is mathematically defined by (neglecting the turbulence effect),

$$\begin{aligned} s'_{fd} &= s_p - s_p^0 \\ &= (k/k_s - 1) [\ln(r_s/r_w) + s_p^0] + (k/k_s) s_x \end{aligned} \quad (5.56)$$

To ensure a positive s'_{fd} for any perforation conditions, we derive a new correlation equation for s_x . For $k_s < k$, s'_{fd} must be greater than zero;

$$s_x \geq (k_{Ds} - 1) [\ln(r_s/r_w) + s_p^0] \quad (5.57)$$

Introducing the effective well radius, $r_{w,eff}$

$$r_{w,eff} = r_w \exp(-s_p) \quad (5.58)$$

Substituting this into Eq. 5.57 gives

$$s_x \geq (k_{Ds} - 1) \ln(r_s/r_{w,eff}) \quad (5.59)$$

Using Eq. 5.54

$$\ln(1 - r_{Dc}^2) \geq (k_{Ds} - 1) \ln(r_s/r_{w,eff}) \quad (5.60)$$

Simplifying for r_{Dc}

$$r_{Dc} \leq \sqrt{1 - \left(\frac{r_{w,eff}}{r_s} \right)^{(1-k_{Ds})}} \quad (5.61)$$

As shown in Fig. 5.16, we can find the boundary curve between positive and negative damage skin factors. At $r_s = l_p + r_w$, Eq. 5.61 must satisfies the following inequality;

$$r_{Dc} \leq \sqrt{1 - \left(\frac{r_{w,eff}}{l_p + r_w} \right)^{(1-k_{Ds})}} \quad (5.62)$$

The above equation defines the region of r_{Dc} where we can obtain a positive s_{fd} . From FEM simulation results (Fig. 5.16), we can approximate r_{Dc} using the linear interpolation (i.e., a straight line) for k_{Ds} to give

$$\begin{aligned} r_{Dc} &= (1 - k_{Ds}) \sqrt{1 - \left(\frac{r_{w,eff}}{l_p + r_w} \right)} \\ &= (1 - k_{Ds}) \sqrt{1 - \frac{r_w \exp(-s_p)}{l_p + r_w}} \end{aligned} \quad (5.63)$$

Also from Fig. 5.17, the dependence of r_s may be included by

$$r_{Dc} = (1 - k_{Ds}) \left(\frac{l_p + r_w}{r_s} \right) \sqrt{1 - \frac{\exp(-s_p)}{l_{Dp} + 1}} \quad (5.64)$$

In anisotropic formations, the equivalent coordinate system gives

For $m_p=1$,

$$r_{Dc} = (1 - k_{Ds}) \left(\frac{l_p + r_w}{r_{sH}} \right) \sqrt{1 - \frac{2 \exp(-s_p)}{(l_{Dp} + 1)(\sqrt[4]{k_H / k_V} + \sqrt[4]{k_V / k_H})}} \quad (5.65)$$

Due to the symmetry of the location of perforations, s_x for multidirectional perforation phasings may be insignificant and hence negligible. This observation is only true for very high perforation shot densities. As a perforation shot density decreases, s_x for multidirectional perforation phasings approaches to one for $m_p=1$ since each perforation becomes independent and has the off-centered effect. With this observation, the r_{Dc} may be given by a function of the dimensionless perforation spacing h_{De} ;

For $m_p \neq 1$,

$$r_{Dc} = (1 - k_{Ds}) \left(\frac{l_p + r_w}{r_{sH}} \right) (1 - e^{-h_{De}}) \sqrt{1 - \frac{2 \exp(-s_p)}{(l_{Dp} + 1) (\sqrt[4]{k_H / k_V} + \sqrt[4]{k_V / k_H})}} \quad (5.66)$$

At high h_{De} , Eqs. 5.66 approaches to Eq. 5.65. Substituting Eq. 5.65 or 5.66 (depending on m_p) into Eq. 5.54 gives the off-centered skin factor.

For perforations extending beyond the damage zone (Fig. 5.18), the effect of formation damage is relatively smaller than that obtained by Eq. 5.52. The perforations create flowpaths through the damaged zone for flow to reach the wellbore without substantial pressure drop. However, the flow concentration around the tip of the perforations will increase and results in additional pressure drop. As Karakas and Tariq (1991) proposed, the equivalent flow system can be obtained by simply replacing the perforation length and the wellbore radius by $l_{p,mod}$ and $r_{w,mod}$

$$l_{p,mod} = l_p - [1 - (k_s / k)] l_{ps}(\alpha) \quad (5.67)$$

$$r_{w,mod} = r_w + [1 - (k_s / k)] l_{ps}(\alpha) \quad (5.68)$$

where l_{ps} is the damage length covering over a perforation which is a function of the perforation orientation, α , relative to the permeability field. Assuming that the damage is distributed similar to the pressure field, $l_{ps}(\alpha)$ can be determined by the following procedures.

An original 2D coordinate system (y, z) is transformed into the following coordinate system (y', z') by

$$y' = y \sqrt[4]{k_z / k_y} \quad (5.69)$$

$$z' = z \sqrt[4]{k_y / k_z} \quad (5.70)$$

Using Eq. 5.69, the horizontal damage radius, r_{sH} is transformed into the equivalent isotropic system as

$$r'_{sH} = r_{sH} \sqrt[4]{k_z / k_y} \quad (5.71)$$

The perforation orientation becomes

$$\alpha' = \tan^{-1}(\sqrt{k_y/k_z} \tan \alpha) \quad (5.72)$$

Conformal mapping to an elliptical coordinate system gives

$$y' = b \sinh \rho \cos \theta \quad (5.73)$$

$$z' = b \cosh \rho \sin \theta \quad (5.74)$$

where b is a constant of conformal mapping defined by

$$b = r_w \sqrt[4]{k_z/k_y} \sqrt{k_y/k_z - 1} \quad (5.75)$$

On the damage boundary, the mapping parameter, ρ_s can be determined by

$$\begin{aligned} \rho_s &= \sinh^{-1}(r'_{sH}/b) \\ &= \ln \left(\frac{r_{sH}}{r_w \sqrt{k_y/k_z - 1}} + \sqrt{\left(\frac{r_{sH}}{r_w \sqrt{k_y/k_z - 1}} \right)^2 + 1} \right) \end{aligned} \quad (5.76)$$

Using Eqs. 5.72-5.74, the other mapping parameter, θ_α can be obtained by

$$\theta_\alpha = \tan^{-1}[\tanh \rho_s \tan \alpha'] \quad (5.77)$$

Substituting Eqs. 5.76 and 5.77 into Eqs. 5.73 and 5.74 gives the perforation position in the equivalent isotropic system;

$$l'_{eH} = b \sinh \rho_s \cos \theta_\alpha \quad (5.78)$$

$$l'_{eV} = b \cosh \rho_s \sin \theta_\alpha \quad (5.79)$$

Applying the inverse transformation into the original anisotropic system gives

$$l_{eH} = l'_{eH} \sqrt[4]{k_y/k_z} \quad (5.80)$$

$$l_{eV} = l'_{eV} \sqrt[4]{k_z/k_y} \quad (5.81)$$

Finally, l_{ps} can be calculated by

$$l_{ps} = \sqrt{l_{eH}^2 + l_{eV}^2} - r_w \quad (5.82)$$

The total skin would correspond to the perforation skin, s_p , obtained with the modified perforation length, $l_{p,mod}$, and the modified well radius, $r_{w,mod}$. The relations provided by Eqs. 5.67 and 5.68 are based on heuristic grounds and are strictly valid for the two

limiting conditions ($k_s=0$ and $k_s=k$). For s_{2D} calculations, l_{Dp} in the first term of the right hand side in Eqs. 5.10 and 5.11 will be given by

$$l_{Dp} = l_{p,mod} / r_w \quad (5.83)$$

and no modification is required in the second term. For s_{wb} and s_{3D} , the following replacement will be required;

$$l_{Dp} = l_{p,mod} / r_{w,mod} \quad \text{for Eqs. 5.21, 5.22, and 5.23} \quad (5.84)$$

$$l_p = l_{p,mod} \quad \text{for Eqs. 5.35 and 5.40} \quad (5.85)$$

For $m_p \geq 3$, some of the perforations may be outside the damaged-zone and the others may not be. In such cases, the skin factor can be estimated by taking the arithmetic average of skin values calculated for each perforation direction. Fig. 5.19 shows the comparison of formation damage skin factors with FEM simulation results ($l_p=0.5$ ft, $r_p=0.02$ ft, $r_w=0.3$ ft, 20 SPF, $k_H/k_V=1$). Clearly perforating beyond the damage zone is very important to minimize the skin factor and obtain favorable production from a perforated well. In Fig. 5.20, $l_p=1.0$ ft, 1 SPF, $k_H/k_V=4$, $\alpha=90^\circ$ and $k_{sH}/k_H=0.1$ are assumed. For the most cases, $m_p=2$ will be the best since the perforation skin is the minimum under these condition. (0.958 for $m_p=1$, 0.081 for $m_p=2$, and 0.529 for $m_p=4$). Fig. 5.21 shows the comparison with FEM simulation results for the various perforation conditions (Table 5.6). For those perforation conditions, the skin model presented in this study give a good match.

5.4 EFFECT OF CRUSHED ZONE DUE TO PERFORATING JET

As discussed by many authors (McLeod, 1983; Karakas *et al.*, 1991; Behrmann, 1996), the permeability damage around the perforations from rock compaction can significantly impair well productivity (Fig. 5.22). Assuming radial flow around the perforations and

negligible wellbore effects, the additional pressure drop caused by the crushed zone can be taken into account. The rate-independent skin factor s^0 can be given by

$$\begin{aligned} s^0 &= \int_{\xi_{D0}}^{\xi_{D1}} k_D^{-1} A_D^{-1} d\xi_D - \int_{\xi'_{D0}}^{\xi'_{D1}} A_D^{-1} d\xi'_D \\ &= \left[\int_{\xi_{Dcz}} (k/k_{cz}) A_D^{-1} d\xi_D - \int_{\xi'_{Dcz}} A_D^{-1} d\xi'_D \right] + \left[\int_{\xi_{Dp}} (k/k_s) A_D^{-1} d\xi_D - \int_{\xi'_{Dp}} A_D^{-1} d\xi'_D \right] \end{aligned} \quad (5.86)$$

where ξ_{Dcz} and ξ_{Dp} stand for the flowpaths inside and outside of the crushed zone. From Eq. 5.52,

$$s^0 = \left[\int_{\xi_{Dcz}} (k/k_{cz}) A_D^{-1} d\xi_D - \int_{\xi'_{Dcz}} A_D^{-1} d\xi'_D \right] + s_{fo} + \frac{k}{k_s} s_p^0(r_{cz}) \quad (5.87)$$

where $s_p^0(r_{cz})$ is a perforation skin factor with $r_p=r_{cz}$. Assuming radial flow inside the crushed zone gives

$$\begin{aligned} A(r) &= 2\pi l_p N_p \\ &= 2\pi l_p L / h_p \end{aligned} \quad (5.88)$$

and

$$\begin{aligned} A_D(r_D) &= A / (2\pi r_w L) \\ &= r_D / h_{De} \end{aligned} \quad (5.89)$$

where h_{De} is given by Eq. 5.35 or 5.40 depending on the perforation phasing. Substituting Eq. 5.89 into Eq. 5.87 and solving the integration give

$$s^0 = h_{De} \left(\frac{k}{k_{cz}} - 1 \right) \ln \frac{r_{cz}}{r_p} + s_{fo} + \frac{k}{k_s} s_p^0(r_{cz}) \quad (5.90)$$

if $k_{cz}=k_s$, Eq. 5.90 reduces to

$$s^0 = s_{fo} + \frac{k}{k_s} s_p^0 \quad (5.91)$$

with this observation, we can obtain

$$\begin{aligned} h_{De} \left(\frac{k}{k_s} - 1 \right) \ln \frac{r_{cz}}{r_p} + s_{fo} + \frac{k}{k_s} s_p^0(r_{cz}) &= s_{fo} + \frac{k}{k_s} s_p^0 \\ s_p^0(r_{cz}) &= s_p^0 + h_{De} \left(\frac{k_s}{k} - 1 \right) \ln \frac{r_{cz}}{r_p} \end{aligned} \quad (5.92)$$

Substituting Eq. 5.90 into Eq. 5.88 gives

$$s^0 = s_{fo} + \frac{k}{k_s} s_p^0 + h_{De} \left(\frac{k}{k_{cz}} - \frac{k}{k_s} \right) \ln \frac{r_{cz}}{r_p} \quad (5.93)$$

The additional skin factor presented in the third term in Eq. 5.93 is proportional to h_{De} . A similar expression for the compaction skin component was shown in McLeod's work. With good perforation shot densities and deep perforation lengths (i.e., $h_{De} \approx 0$), the effect of the compaction zone is negligible. On the other hand, it may be substantial for cased and perforated wells with poor perforation shot densities and short perforation lengths (i.e., $h_{De} \gg 0$).

The turbulence scale factor is also calculated as follows:

$$\begin{aligned} f_t &= \int_{\xi_{D0}}^{\xi_{D1}} \beta_D A_D^{-2} d\xi_D \\ &= \int_{\xi_{Dcz}}^{\xi_{D1}} (\beta_{cz} / \beta) A_D^{-2} d\xi_D + \int_{\xi_{Dp}}^{\xi_{D1}} (\beta_s / \beta) A_D^{-2} d\xi_D \\ &= \beta_{Dcz} \int_{\xi_{Dcz}}^{\xi_{D1}} A_D^{-2} d\xi_D + \beta_{Ds} \int_{\xi_{Dp}}^{\xi_{D1}} A_D^{-2} d\xi_D \end{aligned} \quad (5.94)$$

From Eq. 5.47, the second term of the right hand side is

$$f_t = \beta_{Dcz} \int_{\xi_{Dcz}}^{\xi_{D1}} A_D^{-2} d\xi_D + \beta_{Ds} \left[1 + \left(h_{De} / l_{Dp} \right) \left(1 / r_{De,cz} - 2 \right) \right] \quad (5.95)$$

where

$$r_{De,cz} = r_{cz} / h_{Dp} \quad (5.96)$$

Assuming radial flow within the crushed zone gives

$$f_t = \beta_{Dcz} \left(\frac{h_{De}}{l_{Dp}} \right) \left(\frac{1}{r_{De}} - \frac{1}{r_{De,cz}} \right) + \beta_{Ds} \left[1 + \left(\frac{h_{De}}{l_{Dp}} \right) \left(\frac{1}{r_{De,cz}} - 2 \right) \right] \quad (5.97)$$

From Eqs. 5.93 and 5.97, the perforation skin factor including the effects of formation damage and a crushed zone is given by

$$\begin{aligned} s_p &= s_{fo} + s_p^0 / k_{Ds} + h_{De} (k_{Dcz}^{-1} - k_{Ds}^{-1}) \ln(r_{cz} / r_p) \\ &+ \left\{ \beta_{Dcz} \left(\frac{h_{De}}{l_{Dp}} \right) \left(\frac{1}{r_{De}} - \frac{1}{r_{De,cz}} \right) + \beta_{Ds} \left[1 + \left(\frac{h_{De}}{l_{Dp}} \right) \left(\frac{1}{r_{De,cz}} - 2 \right) \right] \right\} F_{o,w} \end{aligned} \quad (5.98)$$

The above equation is applicable for perforations terminating inside the damage zone ($r_s > l_p + r_w$). For perforations extending beyond the damage zone ($r_s < l_p + r_w$),

$$s_p = s_p^0 + h_{De} (k_{Dcz}^{-1} - 1) \ln(r_{cz} / r_p) + \left\{ 1 + \left(\frac{h_{De}}{l_{Dp}} \right) \left[\beta_{Dcz} \left(\frac{1}{r_{De}} - \frac{1}{r_{De,cz}} \right) + \left(\frac{1}{r_{De,cz}} - 2 \right) \right] \right\} F_{o,w} \quad (5.99)$$

The additional rate-independent skin factor due to a crushed zone is now presented in the second term, which can be obtained by replacing k_s by k in Eq. 5.98. The same expression was presented in Karakas & Tariq's model. Fig. 5.23 shows the verification of the skin equations compared with FEM simulation results for various conditions (Table 5.7). The overall comparison with FEM simulation results shows good agreement.

Table 5.1 Correlation constant, a_m .

m_p	a_m
1	1.00
2	0.45
3	0.29
4	0.19
6	0.10
8	0.08
infinite	0.00

Table 5.2 Correlation constants, b_m and c_m .

m_p	b_m	c_m
1	0.90	2.00
2	0.45	0.60
3	0.20	0.50
4	0.19	0.30
6	0.17	0.20
8	0.15	0.15
infinite	0.00	0.00

Table 5.3 Correlation constants, d_m , e_m , f_m and g_m .

m_p	d_m	e_m	f_m	g_m
1	-2.091	0.0453	5.1313	1.8672
2	-2.025	0.0943	3.0373	1.8115
3	-2.018	0.0634	1.6136	1.7770
4	-1.905	0.1038	1.5674	1.6935
6	-1.898	0.1023	1.3654	1.6490
8	-1.788	0.2398	1.1915	1.6392

Table 5.4 Numerical data for Fig. 5.13.

m_p	n_p	$f_{t,p}$	
		FEM	Analytical
	SPF	-	-
1	10	3.13	1.36
2	10	1.35	1.36
4	10	1.29	1.36
12	10	1.11	1.36
1	1	51.00	58.60
2	1	51.00	58.60
4	1	50.70	58.60
12	1	50.80	58.60

Table 5.5 Comparison with FEM simulation results ($f_{t,p}$).

l_p	r_p	n_p	$f_{t,p}$	
			FEM	Analytical
ft	ft	SPF	-	-
0.5	0.01	5.0	6.83	5.32
0.5	0.02	5.0	4.35	2.92
0.5	0.04	5.0	3.08	1.72
0.5	0.01	2.0	28.81	29.80
0.5	0.02	2.0	14.20	14.80
0.5	0.04	2.0	6.98	7.30
0.5	0.01	0.5	432.92	476.20
0.5	0.02	0.5	201.01	236.20
0.5	0.04	0.5	87.89	116.20
0.3	0.02	2.0	35.49	39.33
1.0	0.02	2.0	4.47	4.45
1.5	0.02	2.0	2.33	2.53
2.0	0.02	2.0	1.48	1.86

Table 5.6 Simulation conditions for Fig. 5.21.

Entry	Unit	Value
r_w	ft	0.3
l_p	ft	0.5~1.5
r_p	ft	0.02
m_p	-	1, 2, 4
n_p	SPF	0.5~24
k_H/k_V	-	1, 4, 25
α	deg.	0, 90
k_s/k	-	0.05~0.9
r_{SH}	ft	0.3~10

Table 5.7 Simulation conditions for Fig. 5.23.

Entry	Unit	Value
r_w	ft	0.3
l_p	ft	0.5, 1.0, 1.5
r_p	ft	0.02
r_{cz}	ft	0.04, 0.07, 0.1
n_p	SPF	0.5, 1, 2, 2.5, 5
k_{cz}/k	-	0.05-0.9

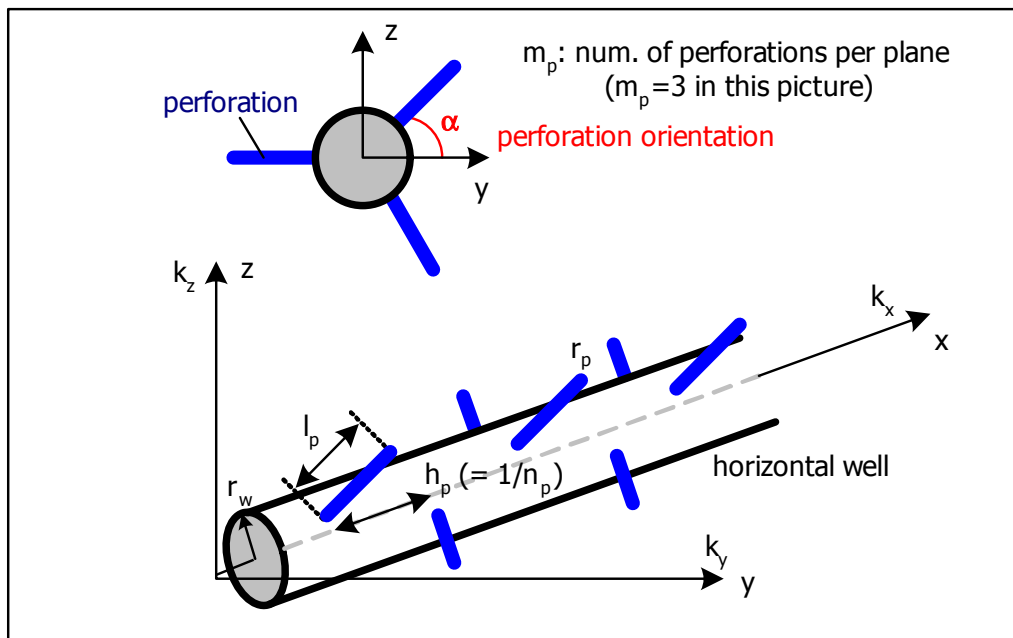


Fig. 5.1 Geometry of a perforated horizontal well.

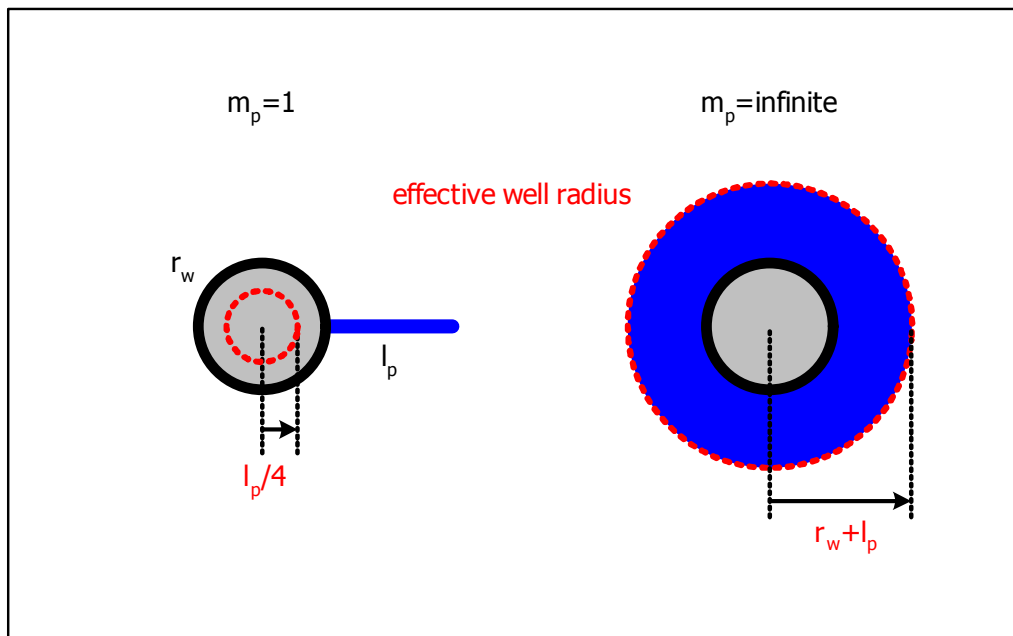


Fig. 5.2 Effective well radius.

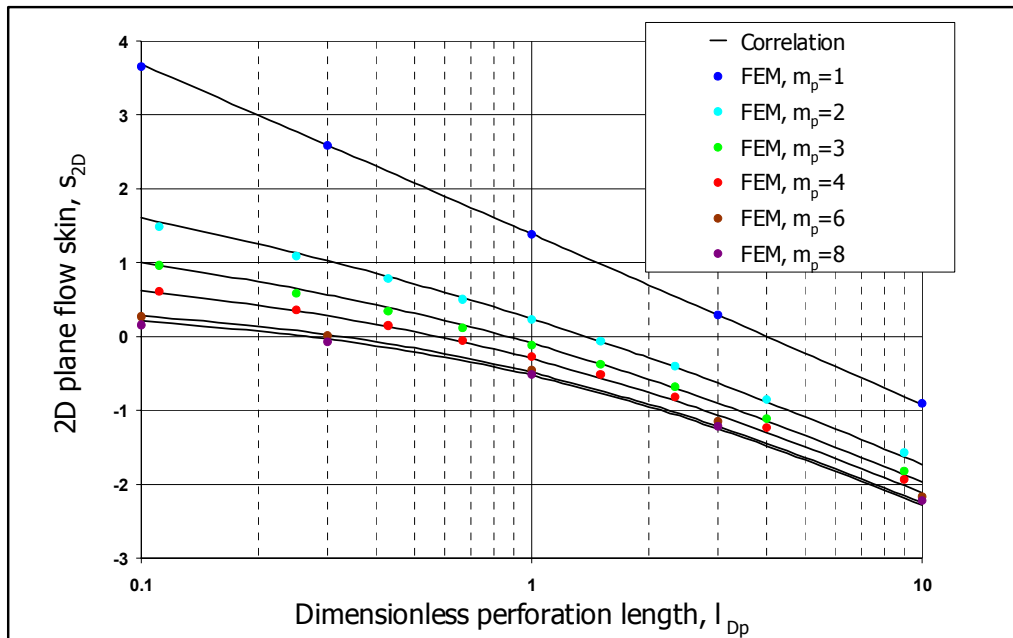


Fig. 5.3 2D plane flow skin factor in an isotropic medium.

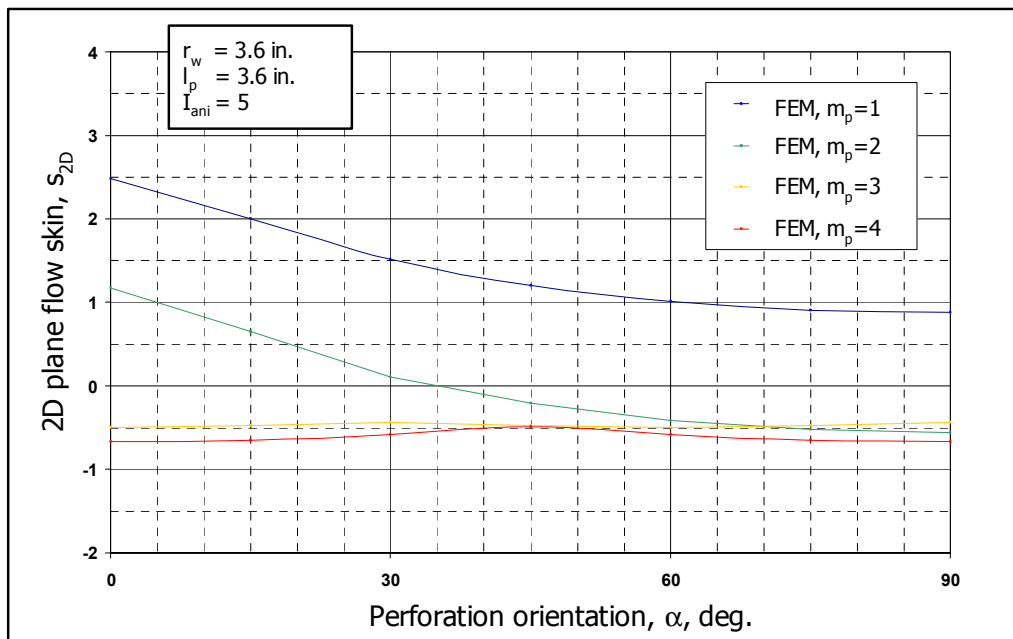


Fig. 5.4 Effect of perforation orientation on s_{2D} .

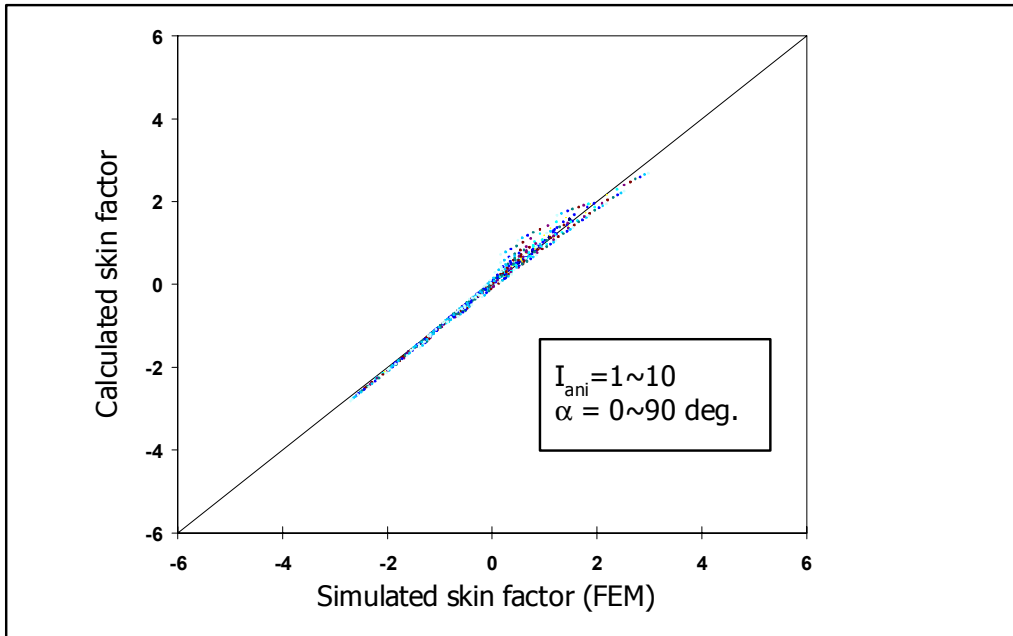


Fig. 5.5 Comparison with FEM simulation database for $m_p=2$.

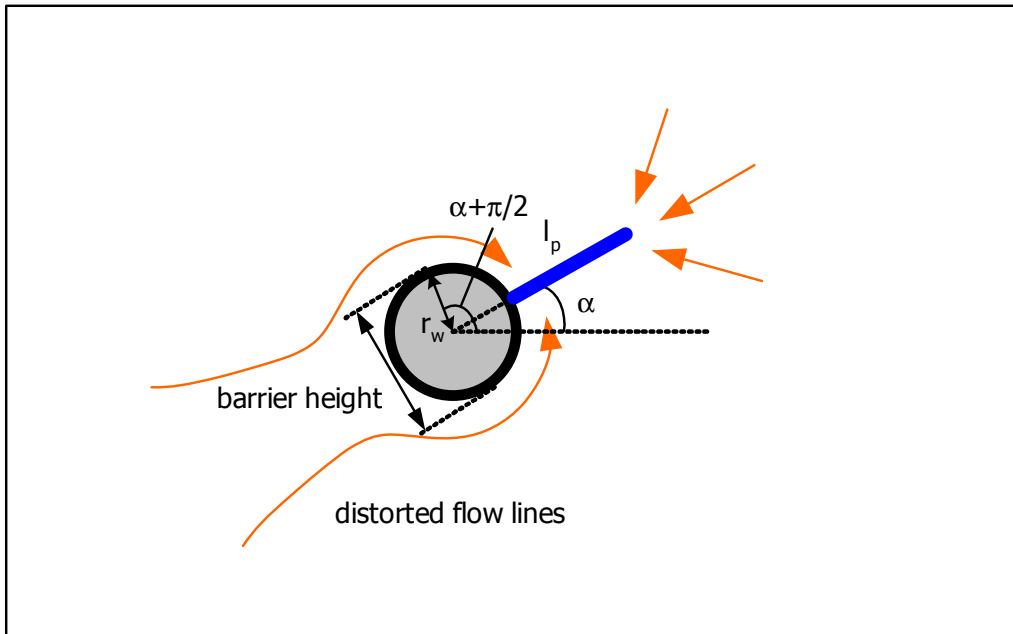


Fig. 5.6 Concept of wellbore blockage effect.

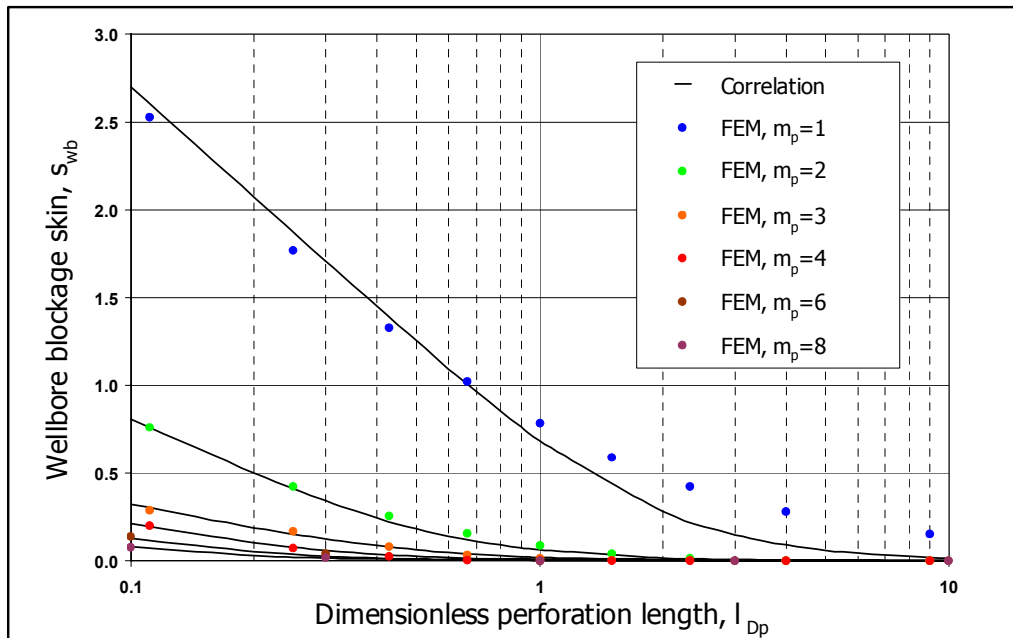


Fig. 5.7 Wellbore blockage effect in an isotropic formation.

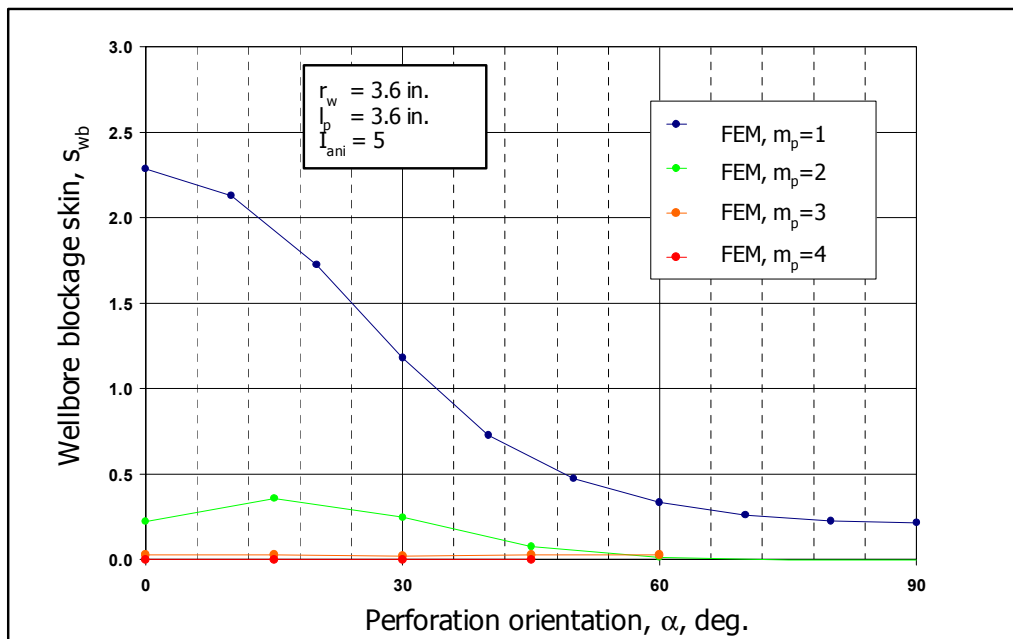


Fig. 5.8 Effect of perforation orientation on s_{wb} .

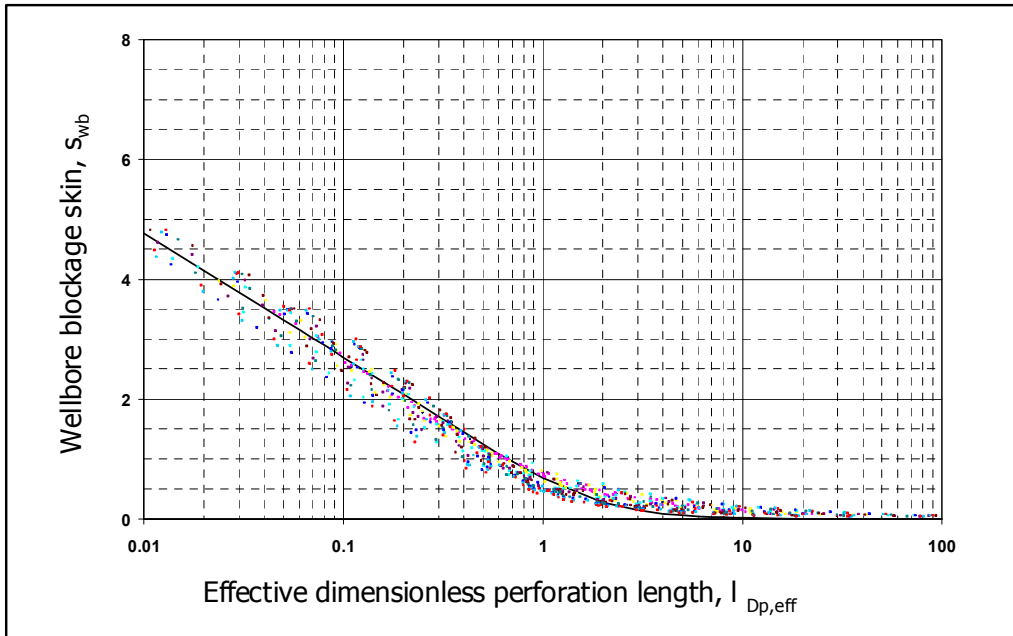


Fig. 5.9 Wellbore blockage effect in anisotropic formations ($m_p=1$).

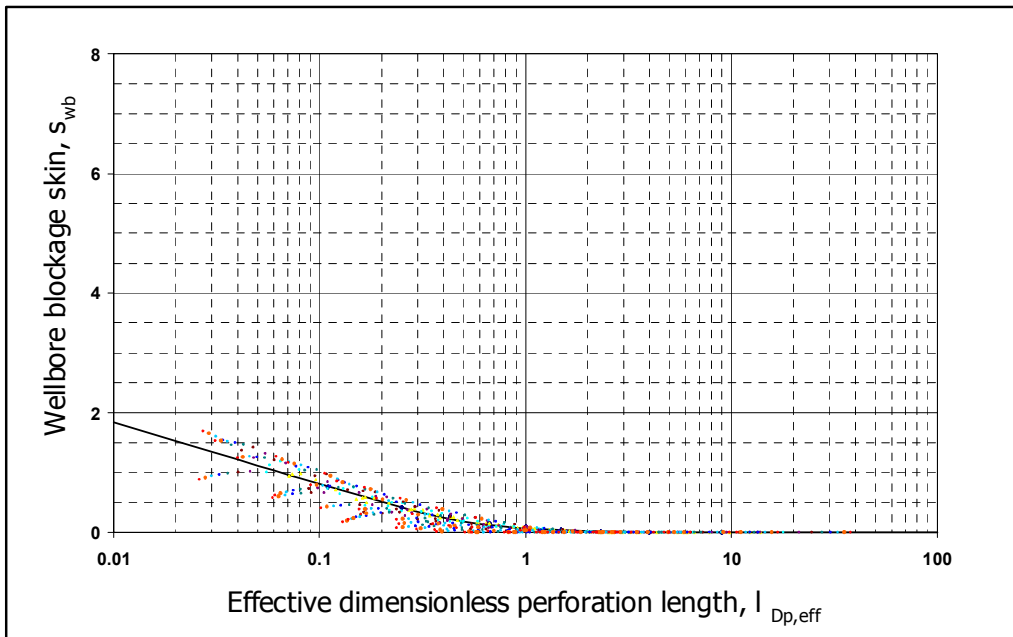


Fig. 5.10 Wellbore blockage effect in anisotropic formations ($m_p=2$).

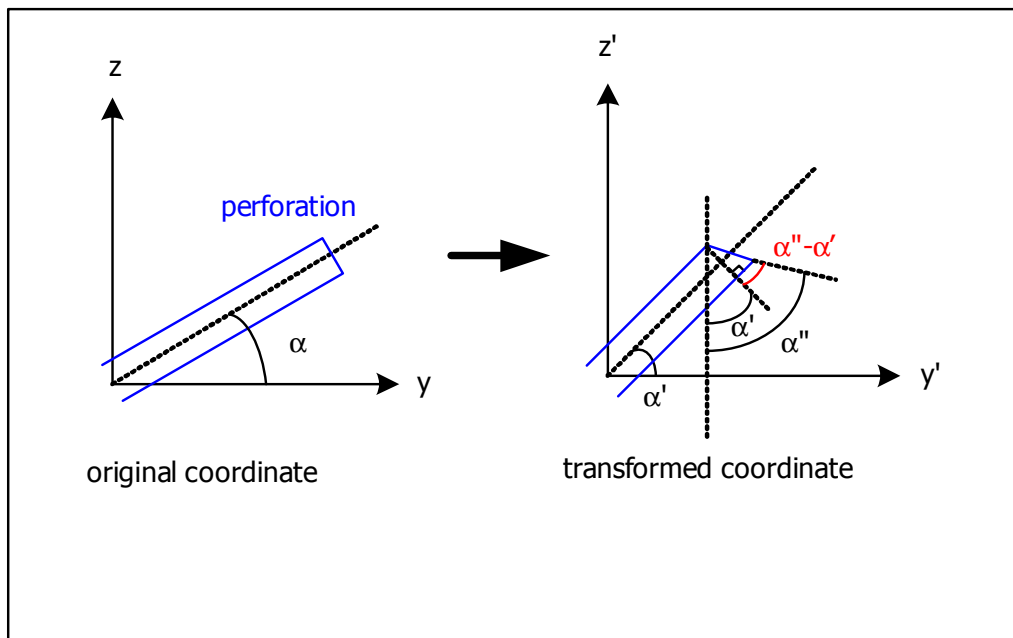


Fig. 5.11 Details of the perforation in the equivalent isotropic system.

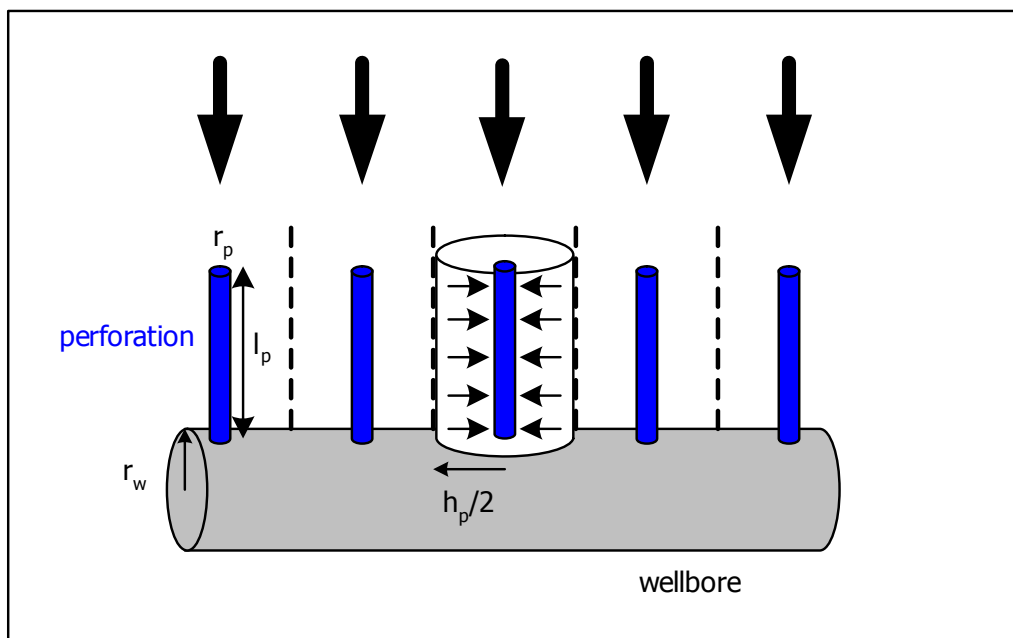


Fig. 5.12 Simplified flow geometry for perforated horizontal wells.

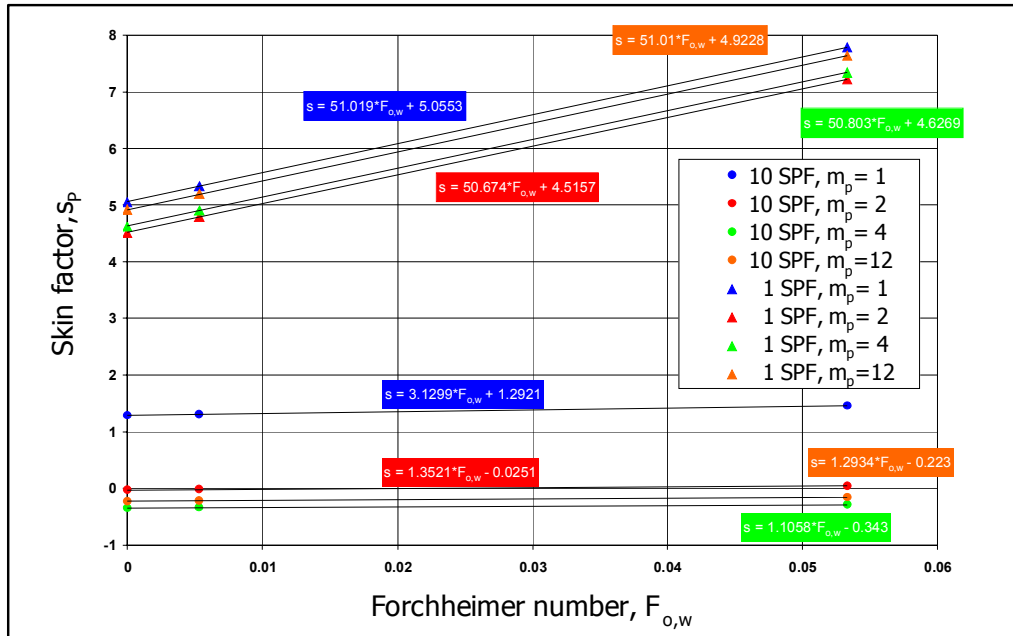


Fig. 5.13 The effect of perforation phasing on turbulence.

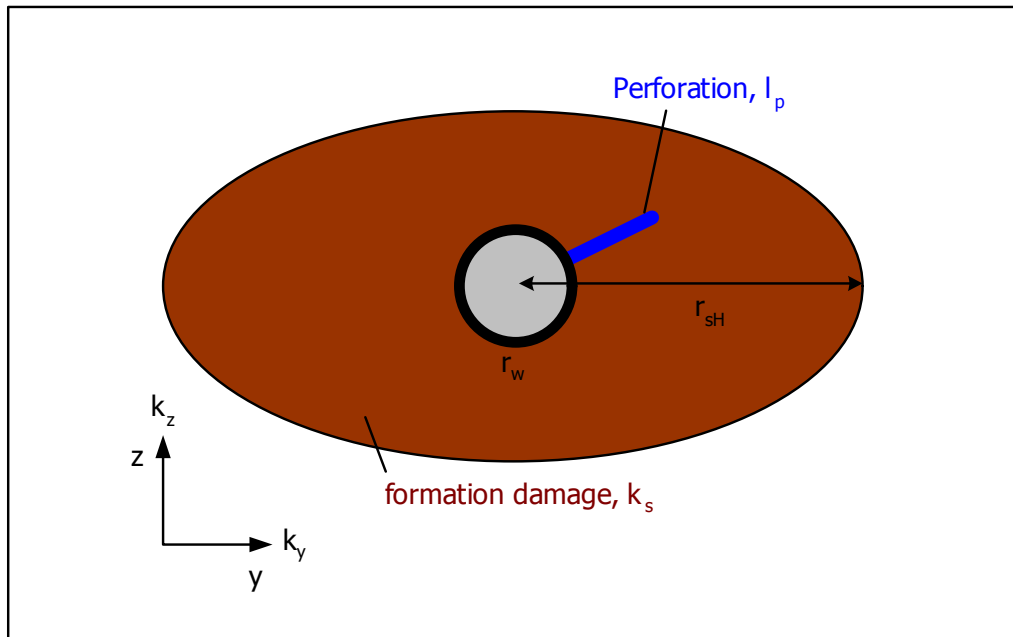


Fig. 5.14 Perforated well with deep penetration of damage.

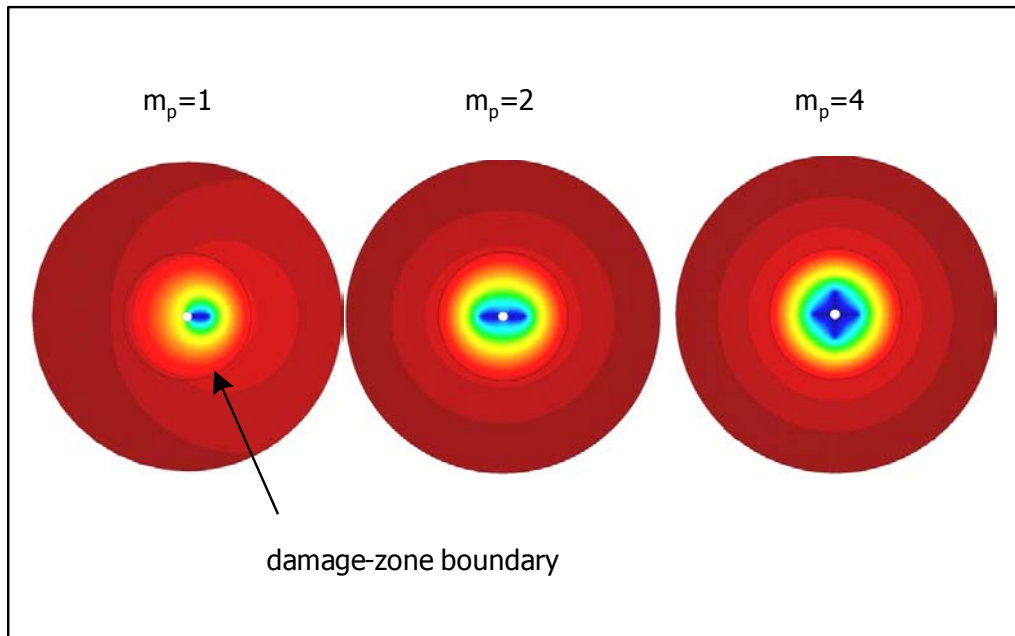


Fig. 5.15 2D pressure contour fill of perforated wells (Pseudoskin, s_x).

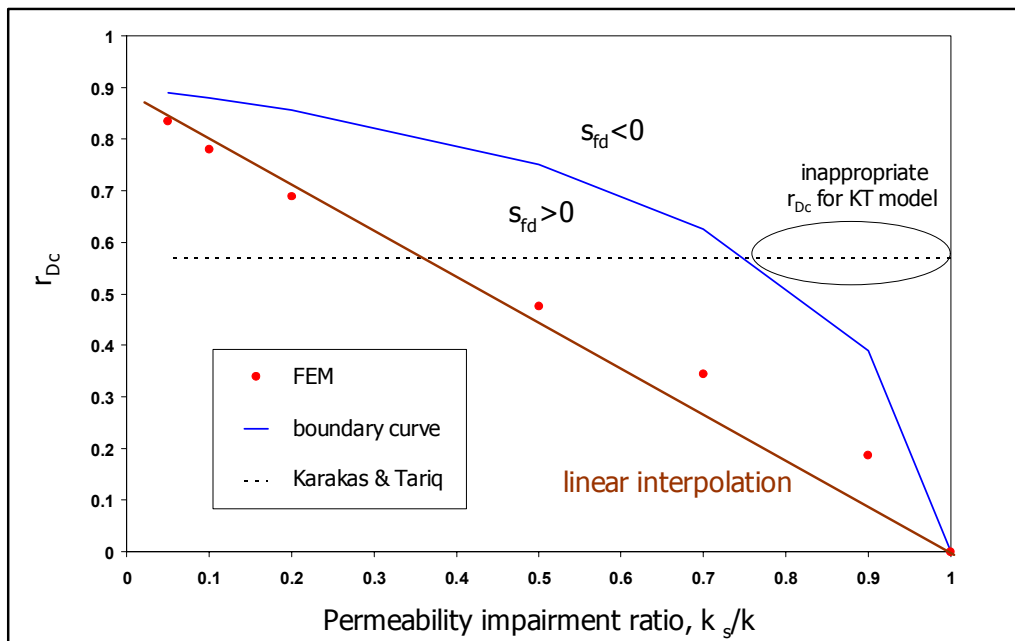


Fig. 5.16 Dimensionless off-centered perforation position, r_{Dc} .

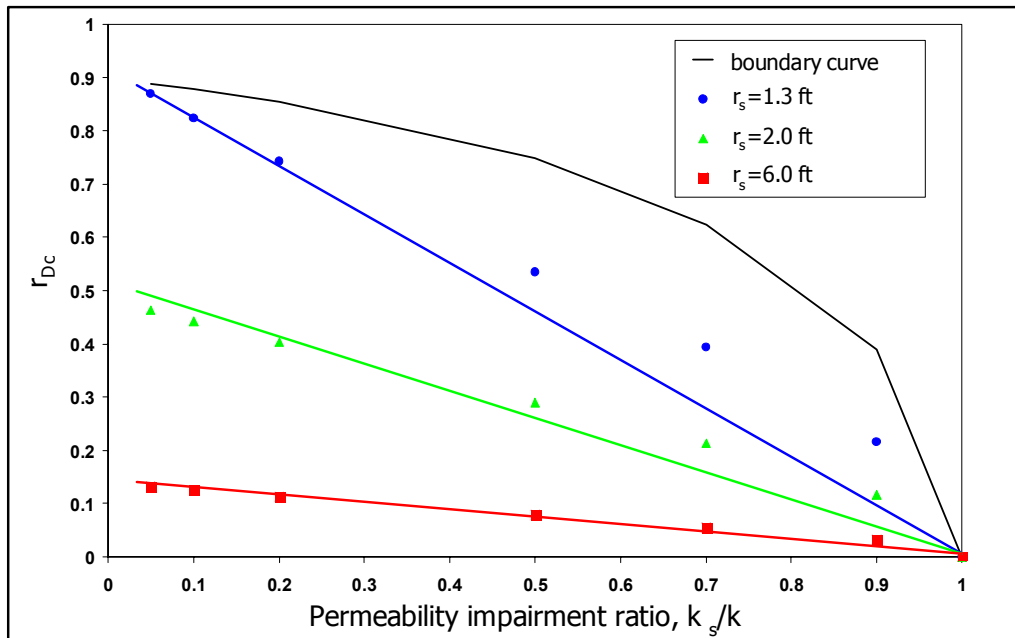


Fig. 5.17 Determination of the dimensionless off-centered perforation position.

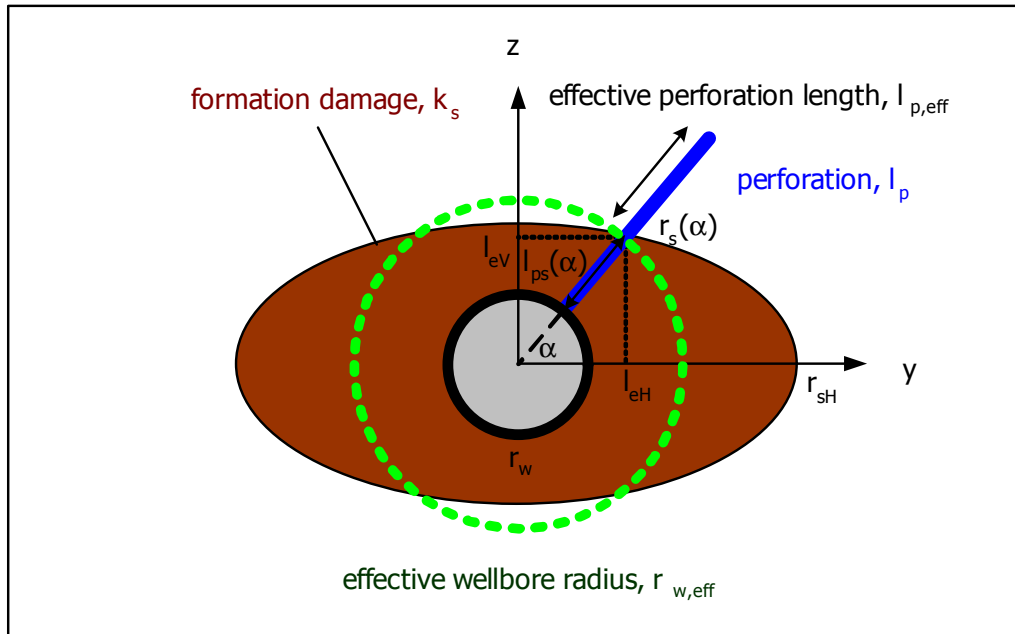


Fig. 5.18 Perforated well with shallow penetration of damage.

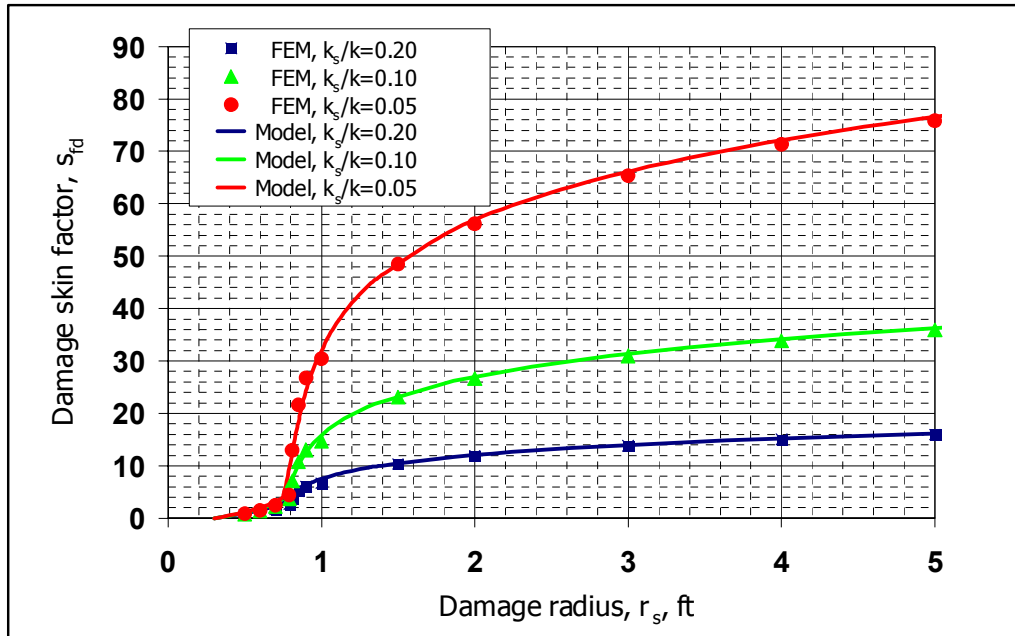


Fig. 5.19 Comparison of formation damage skin with FEM simulation ($k_H/k_V=1$).

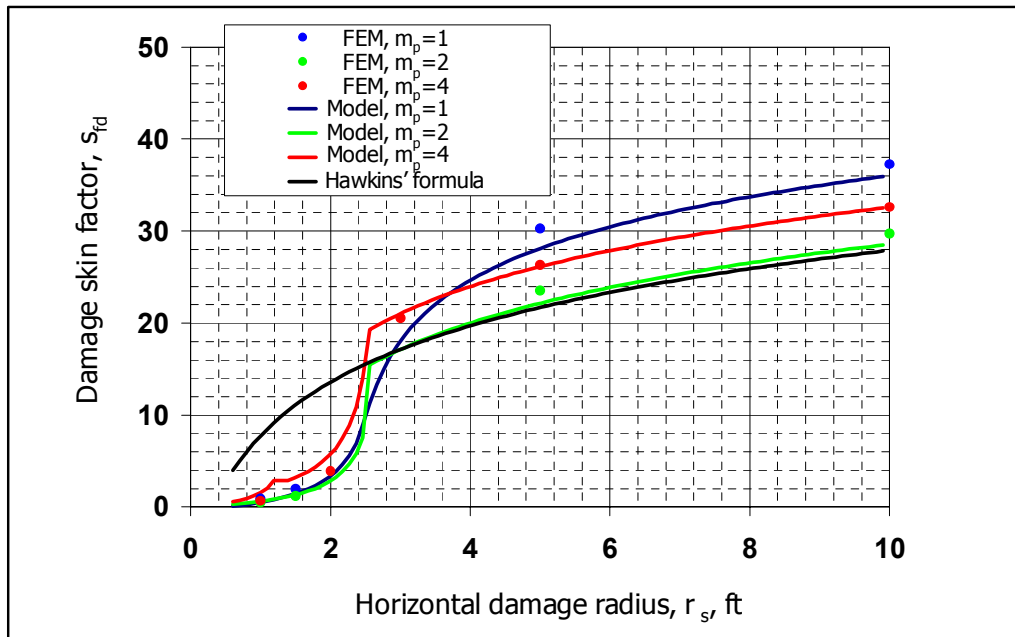


Fig. 5.20 Comparison of formation damage skin with FEM simulation ($k_H/k_V=4$).

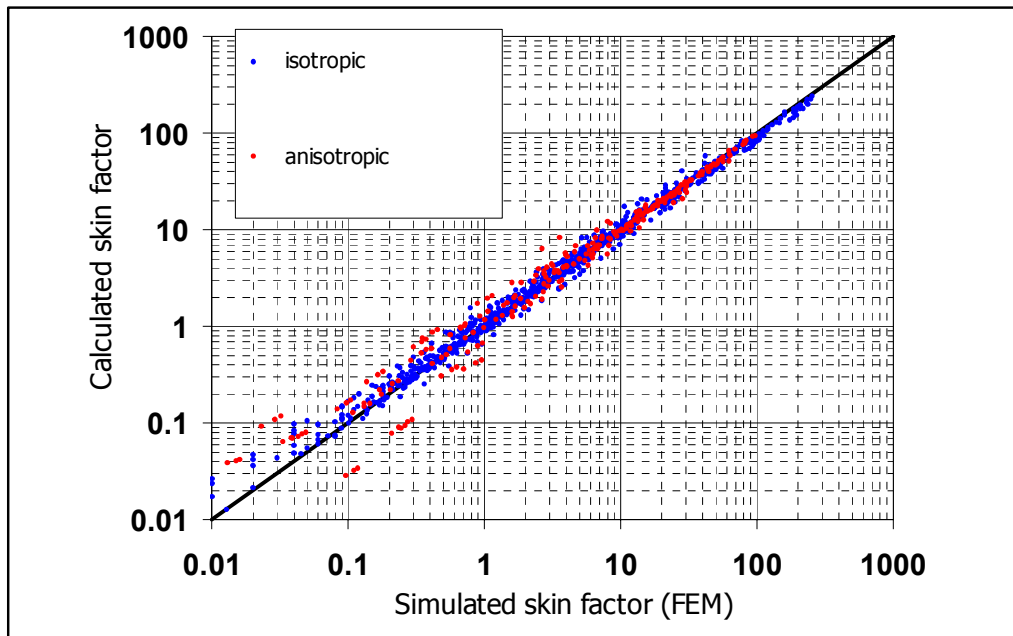


Fig. 5.21 Verification of the perforation skin model.

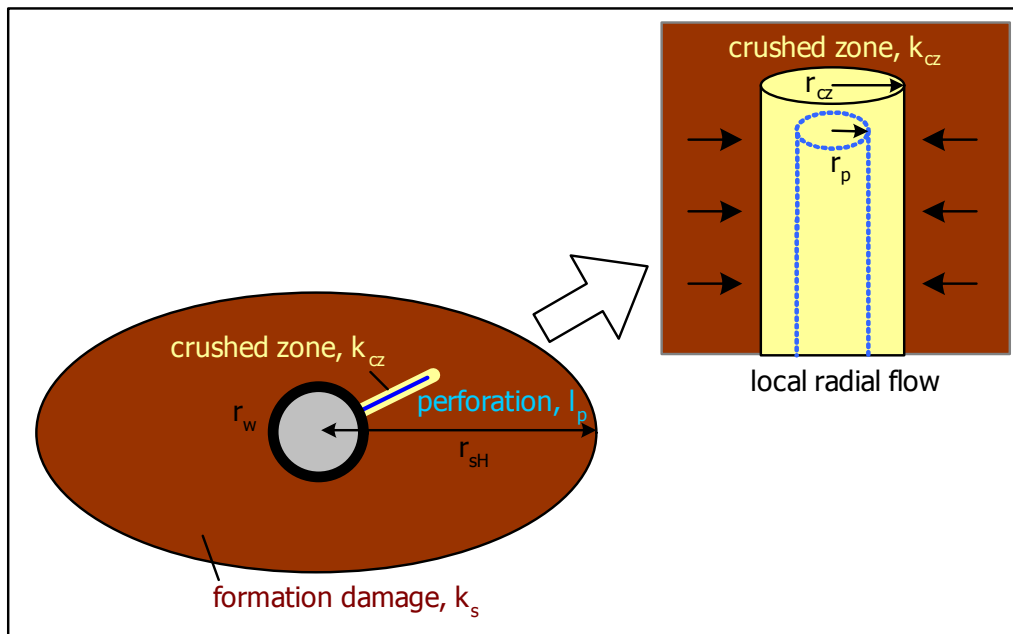


Fig. 5.22 Crushed zone around a perforation.

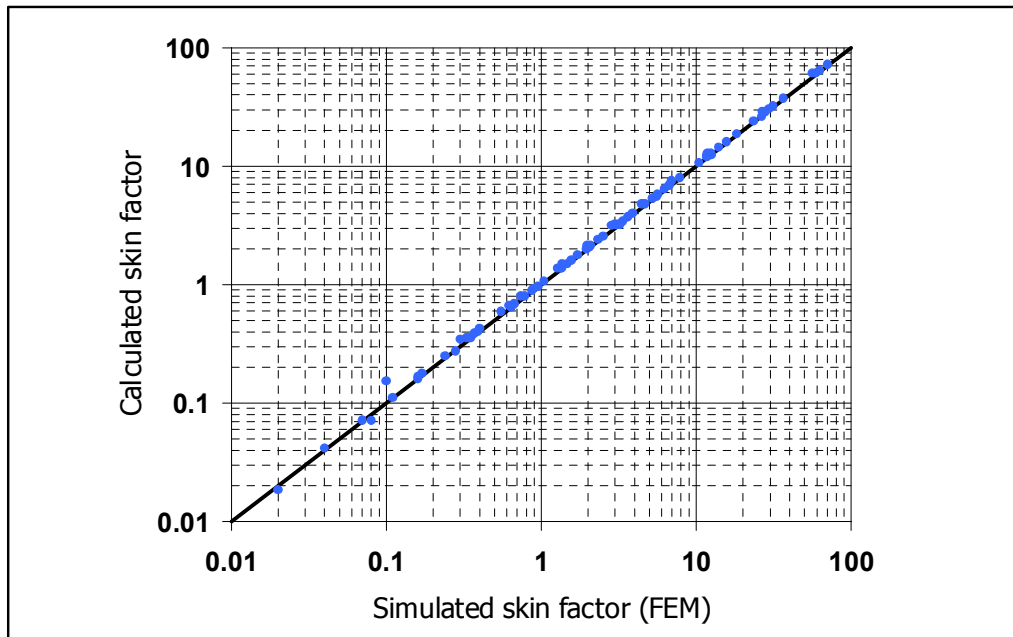


Fig. 5.23 Verification of the perforation skin model with crushed zone.

CHAPTER 6

Gravel Pack Completions

6.1 INTRODUCTION TO GRAVEL PACK COMPLETIONS.

Gravel packing is a well completion method applied to prevent formation sand production and extend the productive life of the well. The method uses a slotted or wire wrapped screen set in the well bore or perforated casing (Fig. 6.1). Many reservoirs comprised of relatively young sediments are so poorly consolidated that sand will be produced along with the reservoir fluids unless the rate is restricted significantly. Sand production leads to numerous production problems, including erosion of downhole tubulars; erosion of valves, fittings, and surface flow lines; the wellbore filling up with sand; collapsed casing because of the lack of formation support; and clogging of surface processing equipment. Even if sand production can be tolerated, disposal of the produced sand is a problem, particularly at offshore fields.

Horizontal gravel packs have gained popularity as a method of completing horizontal wells in formations with large amounts of fines because of the number of failures that have been experienced in openhole screen completions (Walvekar *et al.*, 2002). The gravel between the openhole and the screen is designed to enhance the capability of the completion to filter out the formation particles. The gravel pack sand, though it is actually sand in grain size, should retain most of the formation sand, but let very fine particles pass through it and be produced. Cased-hole gravel packs must have enough gravel outside the casing to assure that all perforations remain filled with gravel that has not become mixed with formation sands while the size and number of

perforations must be sufficient to minimize restriction of fluid flow through perforation tunnels filled by gravel.

6.2 DEVELOPMENT OF A SKIN EQUATION FOR OPEN HOLE GRAVEL PACKED WELLS.

In open hole gravel packed wells, the pressure drop through the gravel should be very small compared with the pressure drop in the formation, unless the gravel permeability has been severely reduced by formation particles. Applying the general form of a skin equation, a skin factor for open hole gravel packed wells is

$$s_{OG} = s_{OG}^0 + f_{t,OG} F_{o,w} \quad (6.1)$$

Assuming the presence of formation damage (Fig. 6.2), the rate-independent skin factor, s_{OG}^0 , can be calculated by integrating Eq. 2.38 in radial coordinates;

$$\begin{aligned} s_{OG}^0 &= \int_{\xi_{D0}}^{\xi_{D1}} k_D^{-1} A_D^{-1} d\xi_D - \int_{\xi'_{D0}}^{\xi'_{D1}} A_D^{-1} d\xi_D \\ &= \left(\int_{r_{Dgi}}^1 k_{Dg}^{-1} r_D^{-1} dr_D + \int_1^{r_{Ds}} k_{Ds}^{-1} r_D^{-1} dr_D \right) - \int_1^{r_{Ds}} r_D^{-1} dr_D \\ &= -k_{Dg}^{-1} \ln r_{Dgi} + k_{Ds}^{-1} \ln r_{Ds} - \ln r_{Ds} \\ &= -k_{Dg}^{-1} \ln r_{Dgi} + (k_{Ds}^{-1} - 1) \ln r_{Ds} \end{aligned} \quad (6.2)$$

where

$$r_{Dgi} = r_{gi} / r_w \quad (6.3)$$

$$k_{Dg} = k_g / k \quad (6.4)$$

r_{gi} and k_g are the inner screen (liner) radius and the permeability of gravel placed between the openhole and the screen. The first term of Eq. 6.2 is usually negligible due to the high permeability of gravel compared with formation permeability unless gravel is damaged (e.g., scale, wax or drilling mud contamination). Then, Eq. 6.1 reduces to the usual Hawkins' formula:

$$s_{OG}^0 = (k_{Ds}^{-1} - 1) \ln r_{Ds} \quad \text{for } k_g \gg k \quad (6.5)$$

The turbulence scale factor for open hole gravel packed wells is similarly derived by

$$\begin{aligned}
f_{t,OG} &= \int_{\xi_{D0}}^{\xi_{D1}} \beta_D A_D^{-2} d\xi_D \\
&= \int_{r_{Dgi}}^1 \beta_{Dg} r_D^{-2} dr_D + \int_1^{r_{Ds}} \beta_{Ds} r_D^{-2} dr_D + \int_{r_{Ds}}^{r_{Db}} r_D^{-2} dr_D \\
&\approx \beta_{Dg} (1/r_{Dgi} - 1) + \beta_{Ds} (1 - 1/r_{Ds}) + 1/r_{Ds} \\
&= \beta_{Dg} (1/r_{Dgi} - 1) + \beta_{Ds} + (1 - \beta_{Ds})/r_{Ds}
\end{aligned} \tag{6.6}$$

where r_{Db} term is neglected sin the above equation and

$$\beta_{Dg} = \beta_g / \beta \tag{6.7}$$

and for $k_g \gg k$

$$f_{t,OG} = \beta_{Ds} + (1 - \beta_{Ds})/r_{Ds} \tag{6.8}$$

and Eq. 6.8 reduces to the turbulence scale factor for openhole completions given by Eq. 3.6.

In anisotropic formations, the rate-independent skin and the turbulent scale factors are given by

$$s_{OG}^0 = -k_{Dg}^{-1} \ln r_{Dgi} + (k_{Ds}^{-1} - 1) \ln \left(\frac{r_{DsH} + \sqrt{r_{DsH}^2 + I_{ani}^2 - 1}}{I_{ani} + 1} \right) \tag{6.9}$$

$$f_{t,OG} = \beta_{Dg} \left(\frac{1}{r_{Dgi}} - 1 \right) + \beta_{Ds} + (1 - \beta_{Ds}) \left(\frac{I_{ani} + 1}{r_{DsH} + \sqrt{r_{DsH}^2 + I_{ani}^2 - 1}} \right) \tag{6.10}$$

6.3 DEVELOPMENT OF A SKIN EQUATION FOR CASED HOLE GRAVEL PACKED WELLS.

For inside-casing gravel pack completions (Fig. 6.3), the pressure drop through the gravel-packed perforations can contribute significantly to the overall pressure drop and be divided into three parts; the pressure drop in the gravel between the casing and screen which is usually small and can be neglected, the pressure drop occurring in the casing and cement perforation tunnels which is usually higher, and the pressure drop outside the casing caused by flow converging to the perforations. The latter two pressure drops are

considered in this study. According to the general form of a skin equation, a skin equation for cased, perforated and gravel packed wells can be presented by

$$s_{CG} = s_{CG}^0 + f_{t,CG} F_{o,w} \quad (6.11)$$

The rate-independent skin factor, s_{CG}^0 , is given by the integration form:

$$s_{CG}^0 = \int_{\xi_D} k_D^{-1} A_D^{-1} d\xi_D - \int_{\xi_D'} A_D^{-1} d\xi_D' \quad (6.12)$$

The first integration of the right hand side can be divided into two intervals:

$$\begin{aligned} s_{CG}^0 &= \left(\int_{\xi_{Dic}} k_D^{-1} A_D^{-1} d\xi_D + \int_{\xi_{Doc}} k_D^{-1} A_D^{-1} d\xi_D \right) - \int_{\xi_D'} A_D^{-1} d\xi_D' \\ &= s_{CG,ic}^0 + s_{CG,oc}^0 \end{aligned} \quad (6.13)$$

where

$$s_{CG,ic}^0 = \int_{\xi_{Dic}} k_D^{-1} A_D^{-1} d\xi_D \quad (6.14)$$

$$s_{CG,oc}^0 = \int_{\xi_{Doc}} k_D^{-1} A_D^{-1} d\xi_D - \int_{\xi_D'} A_D^{-1} d\xi_D' \quad (6.15)$$

ic and oc denote inside and outside of the casing. We presume the flow through the casing tunnel is linear to give

$$s_{CG,ic}^0 = \int_0^{t_{Dct}} k_{Deg}^{-1} A_D^{-1} dx_D \quad (6.16)$$

where

$$t_{Dct} = t_{ct} / r_w \quad (6.17)$$

$$k_{Deg} = k_{cg} / k \quad (6.18)$$

t_{ct} and k_{cg} are the casing tunnel length and the permeability inside the tunnel filled by gravel. The dimensionless flow area for the linear flow region is

$$\begin{aligned} A_D &= N_p \pi_{ct}^2 / (2\pi_w L) \\ &= r_{Dct}^2 / 2h_{Dp} \end{aligned} \quad (6.19)$$

where

$$r_{Dct} = r_{ct} / r_w \quad (6.20)$$

$$h_{Dp} = h_p / r_w \quad (6.21)$$

and r_{ct} is the casing tunnel radius. Substituting Eq. 6.19 into Eq. 6.16 gives

$$\begin{aligned}
s_{CG,ic}^0 &= k_{Dcg}^{-1} \int_0^{t_{Dct}} (2h_{Dp} / r_{Dct}^2) dx_D \\
&= \left(\frac{2h_{Dp}}{r_{Dct}^2} \right) \frac{t_{Dct}}{k_{Dcg}}
\end{aligned} \tag{6.22}$$

Figs. 6.4 (Case 1) and 6.5 (Case 2) show the pressure field of gravel packed wells where the reservoir permeabilities are low and high ($k=10$ and $1,000$ md), respectively. Both cases have the same perforation conditions and gravel permeability ($k_p=50,000$ md). It is assumed that the perforation tunnel, the casing tunnel, and the annular space inside casing are cleanly filled with the gravel. Fig. 6.6 shows the pressure profile in the direction along the perforation for each case. The normalized pressure is defined by pressure divided by the total pressure drop of the system, which shows where the major pressure drop occurs. The result shows that the pressure drops through the perforation tunnel can be negligible compared with that inside the formation for Case 1 ($k_p \gg k$). The entire pressure field looks very similar to that of a cased and perforated well. On the other hand, the pressure drop through the gravel can be substantial compared with one inside formation for Case 2 ($k_p = 50k$). The pressure field is more likely to be spherical near the perforation and flow convergence to the base of the perforation is observed.

We can conclude that the flow geometry outside the casing depends on the ratio of the gravel permeability to formation permeability, k_{Dpg} ($=k_p/k$), which approaches to one of a cased and perforated well for $k_{Dpg}=\infty$ and one of a perforated liner for $k_{Dpg}=1$. With this observation, the following interpolation may be applied to calculate skin components outside the casing zone:

$$s_{CG,oc}^0 = (1 - k_{Dpg}^{-\delta}) s_p^0 + k_{Dpg}^{-\delta} s_{pL}^0 \Big|_{mp=1} \tag{6.23}$$

where $s_{pL}^0|_{mp=1}$ and δ denote a perforated liner skin factor with $m_p=1$ and an empirical constant determined by FEM simulation results. A choice of $\delta \approx 0.5$ shows good matches as shown in Fig. 6.7.

Similarly the turbulence scale factor is obtained by the following equation;

$$f_{t,CG} = f_{t,CG,ic} + f_{t,CG,oc} \quad (6.24)$$

For the inside the casing tunnel,

$$f_{t,CG,ic} = \left(\frac{2h_{Dp}}{r_{Dct}^2} \right)^2 \beta_{Deg} t_{Dct} \quad (6.25)$$

The turbulence scale factor for the outside casing is correlated by

$$f_{t,CG,oc} = (1 - k_{Dpg}^{-0.5}) f_{t,P} + k_{Dpg}^{-0.5} f_{t,PL} \Big|_{mp=1} \quad (6.26)$$

Fig. 6.8 shows the comparison of Eq. 6.11 with Golan and Whitson's model (linear flow model). The simulation conditions are described in Fig. 6.9. As discussed in the previous section, the flow geometry greatly depends on the ratio of the reservoir to perforation tunnel permeabilities. For $k/k_p < 0.01$, since the perforation creates the efficient flow geometry, skin factor is not significant. As k/k_p increases, skin factors calculated by Golan and Whitson's model become greater than FEM simulation results. This is because the flow geometry near the perforation through the casing is no longer linear but spherical (as if there is no perforation in the formation). Since the model developed here accounts for the transition from linear to spherical flow, it can be reliably applied for any k/k_p .

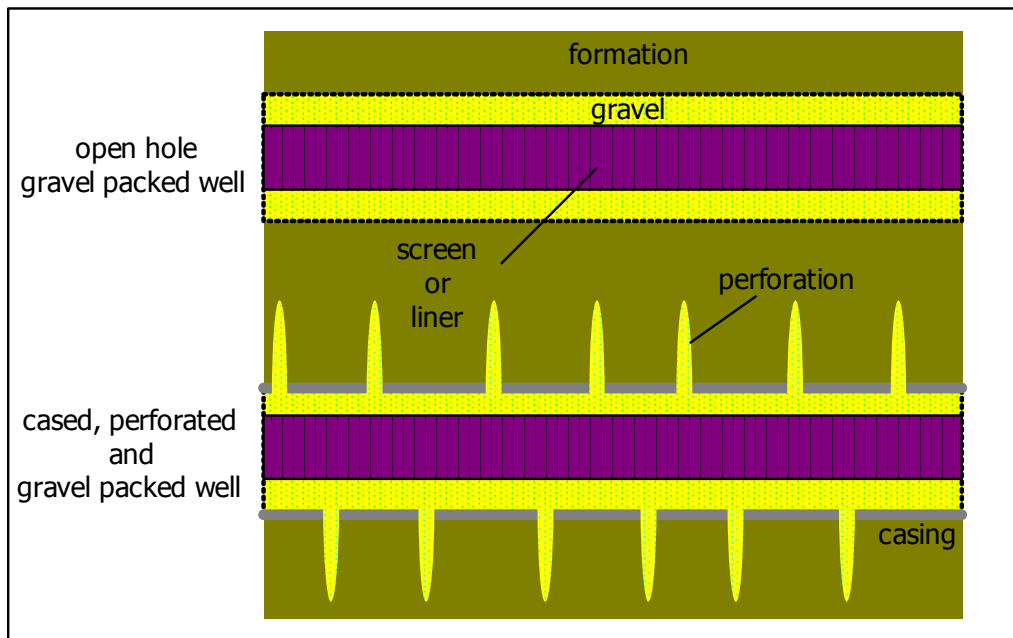


Fig. 6.1 Gravel pack completions.

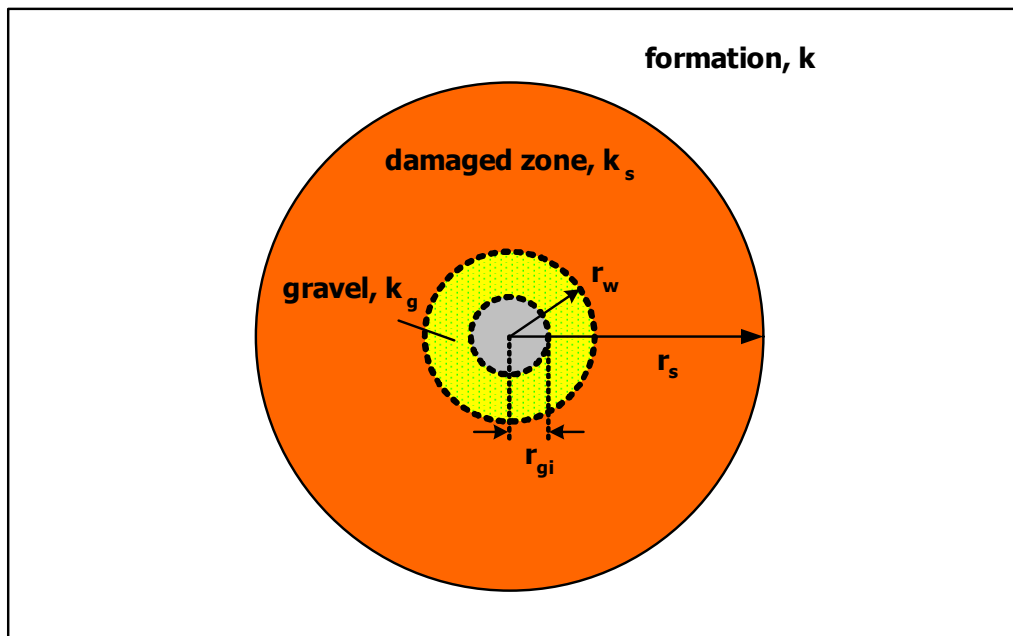


Fig. 6.2 Mathematical representation of open hole gravel packed wells.

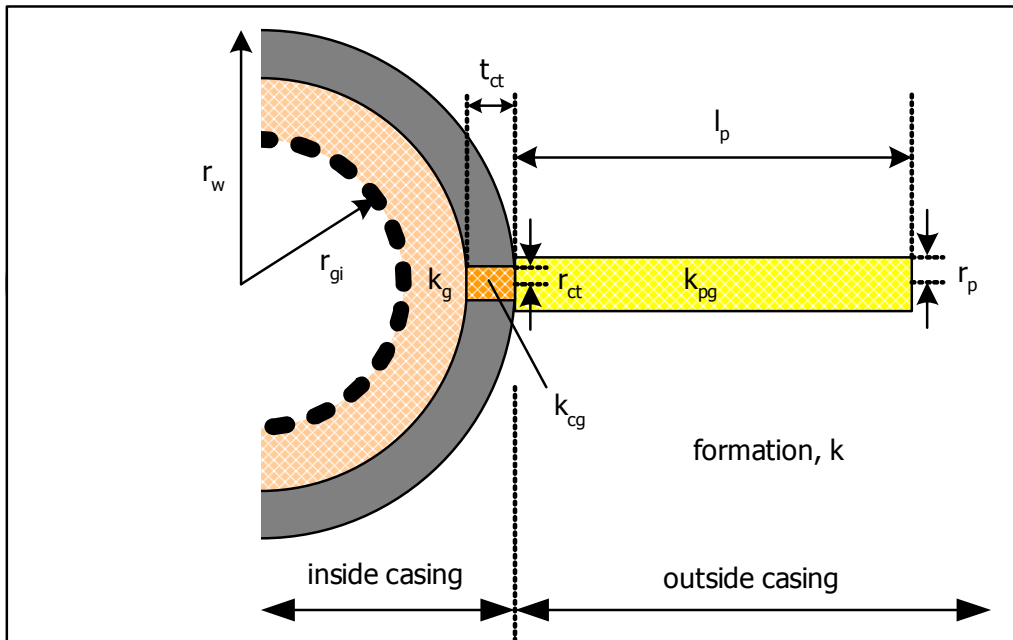


Fig. 6.3 Mathematical representation of cased and gravel packed wells.

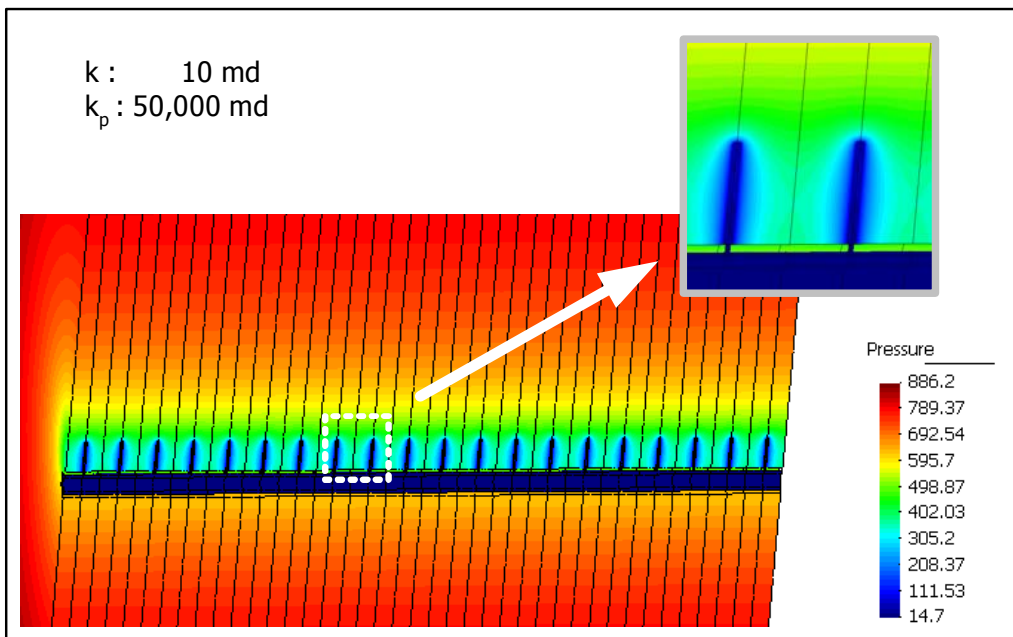


Fig. 6.4 FEM simulation result for a low permeability reservoir.

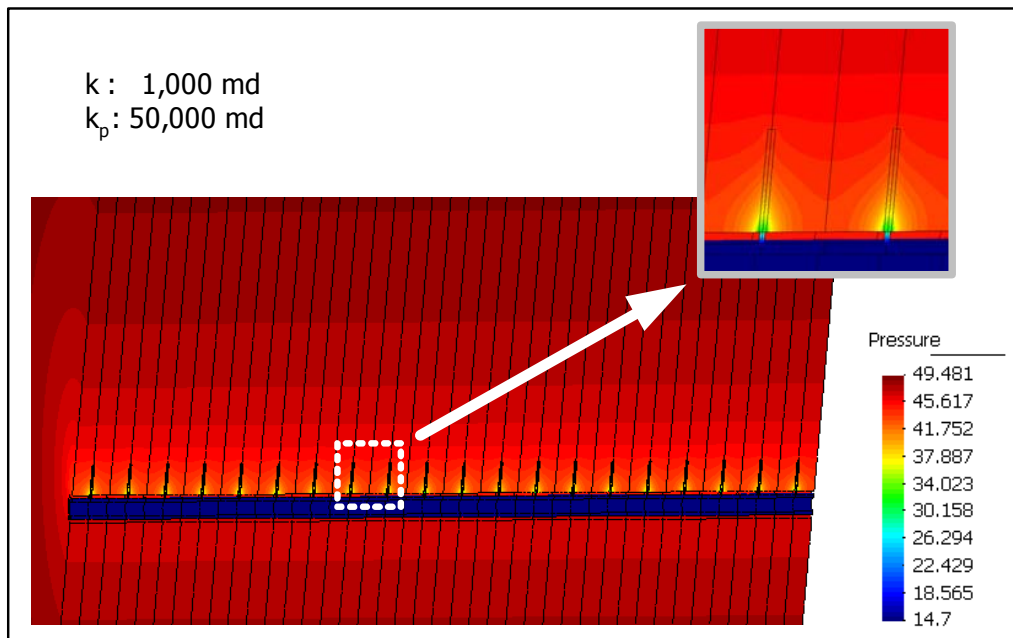


Fig. 6.5 FEM simulation result for a high permeability reservoir.

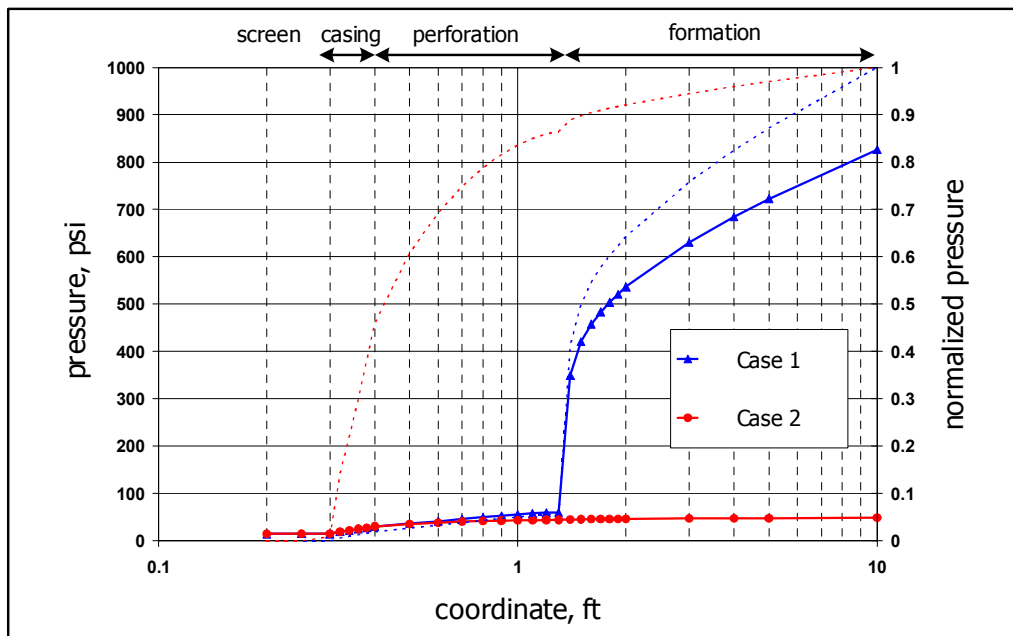


Fig. 6.6 Pressure profile of cased and gravel packed wells.

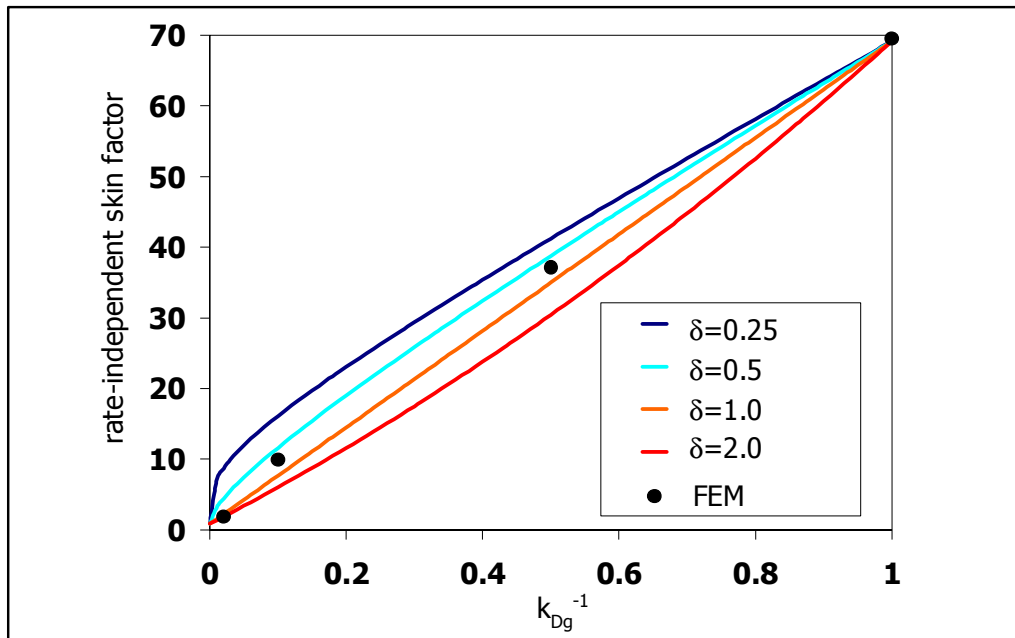


Fig. 6.7 Determination of the interpolation constant for the gravel pack model.

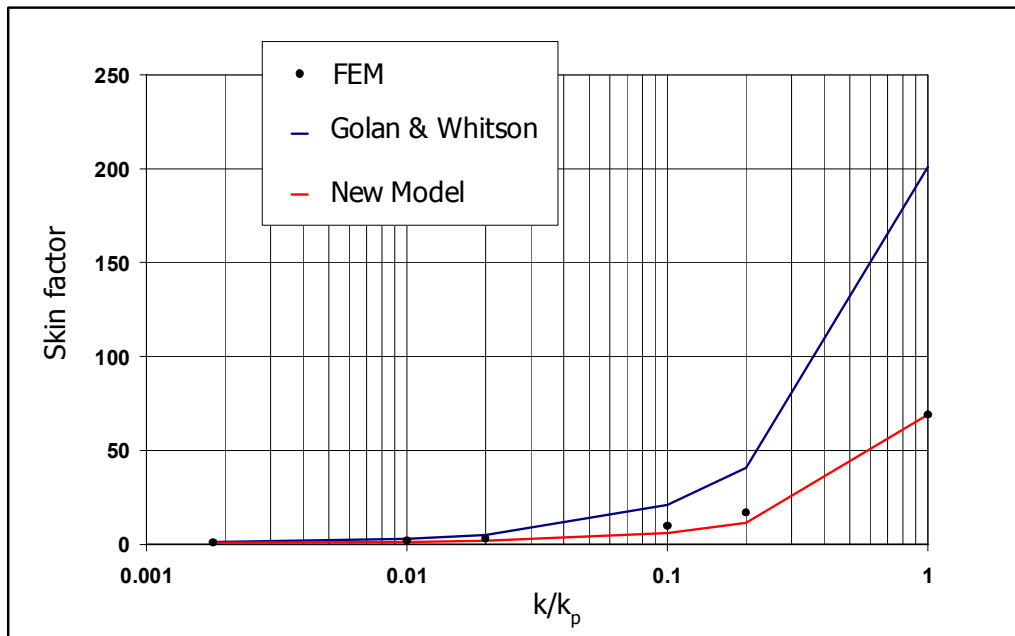


Fig. 6.8 Comparison and verification of the gravel pack skin model.

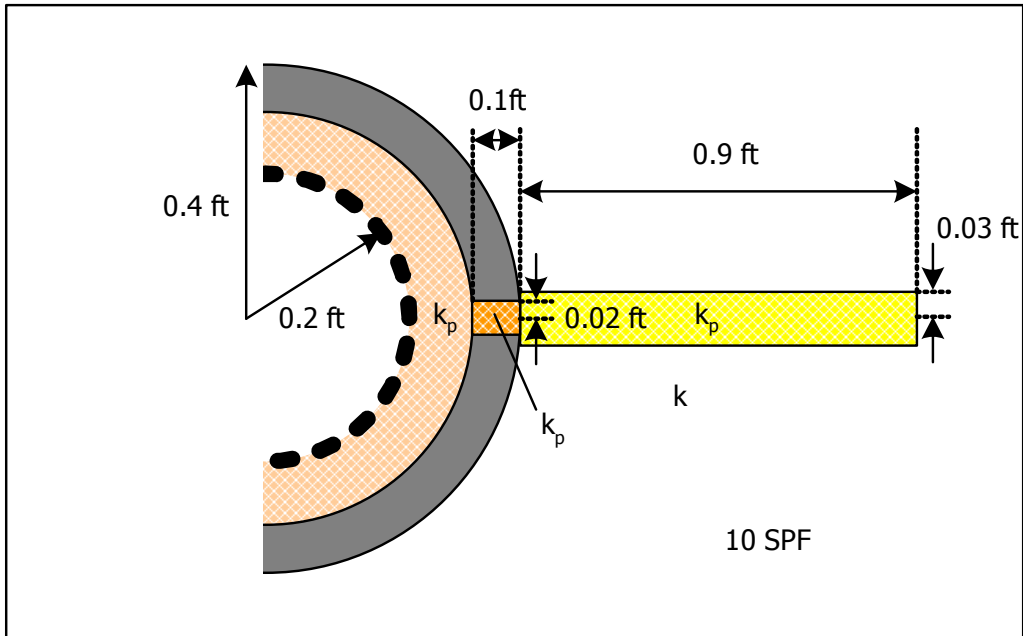


Fig. 6.9 Simulation conditions for Fig. 6.8.

CHAPTER 7

Guidelines for Horizontal Well Completions – Application of the Skin Factor Models

7.1 SLOTTED (PERFORATED) LINER OPTIMIZATION

Slotted liners are commonly characterized by open area of the liner (inflow area relative to the liner surface). The open area of a slotted or perforated liner is often in the range of 1~3%. Fig. 7.1 shows the rate-independent skin factors and the turbulence scale factors for various slot patterns, using the range of parameters presented in Table 7.1. All the data is obtained by the slotted liner skin model presented in Chapter 4. The results generate bands that contain the lower and upper limit lines for s_{SL}^0 and $f_{t,SL}$. Both factors tend to decrease as the open area increases. With the selection of the proper slot design, s_{SL}^0 of 0.5 to 2.0 is easily obtained. As discussed by Kaiser *et al.* (2000), the recommended slot pattern is usually higher m_s and smaller w_s (i.e., smaller slots allow higher slot densities for a given open area). However, too small a slot width may result in the plugging of slots with grains of formation sand. The turbulence scale factors range from 4 to 500 (Note that the turbulence scale factor for openhole completions is equal to one). The turbulence effects for slotted liners are more significant and about 10 times larger than for openhole completions even with the optimum slot design. This is primarily due to the convergent flow into the slots.

Fig. 7.2 shows results for perforated liners for various perforation patterns presented in Table 7.2. The overall trend is similar to that of slotted liner completions. For the given open areas, the rate-independent skin factor, s_{PL}^0 , can be very small and negligible. The turbulent scale factors are slightly higher than those for slotted liners. The

flow into perforations induces spherical flow rather than radial flow, resulting in severe flow concentrations and increasing the turbulence effects.

Plugging of slots may be a major problem in unconsolidated formations. The flow through the slot becomes flow through a porous medium instead of open-channel flow, substantially increasing the pressure loss. Fig. 7.3 shows the skin analysis of slots filled by formation sand. Comparing with Fig. 7.1, the overall performance becomes poor for both the rate-independent skin and the turbulence scale factors. For slots plugged by formation sand, the open area of liners is more likely to be important since we could still obtain small skin factors ($s_{sl} < 5$) with the proper slot design. For high-rate wells, the importance of open area is further emphasized. Plugged slots with low open areas induce extremely high turbulence effects, up to hundreds of times higher than openhole completions.

Fig. 7.4 shows a summary of skin factor for slotted or perforated liner completions where formation damage is not severe. For high-rate production wells, liner skin factors become substantial, especially if slots are plugged by formation sand. For low-rate production wells, liner skin factor are very small and negligible and hence the overall performance is very similar to that of open hole completions.

7.2 PERFORATING HORIZONTAL WELLS

The major difference between horizontal and vertical perforated wells is the influence of permeability anisotropy on perforation orientation relative to the minimum and maximum permeability directions. The perforation skin model developed in Chapter 5 shows that perforations should be oriented parallel to the direction of minimum permeability to give the minimum perforation skin factor (the maximum perforation productivity). For most horizontal wells, this means that perforations should be vertical, extending from the upper

and/or lower sides of the wellbore. With this advantage, the reservoir anisotropy will make the perforation skin factor decrease and result in favorable production. 180° perforation phasing ($m_p=2$) will be the best completion technique for horizontal perforated wells since all the perforations can be orientated in the direction of minimum permeability. As a result, multidirectional perforation techniques ($m_p>2$) applied for anisotropic formations may not be efficient, unlike for isotropic formations. However, with sufficient perforation shot densities, multidirectional perforation technique (i.e., $m_p=4$) could provide skin factors almost as small as $m_p=2$ (Fig. 7.5). Multidirectional perforation phasings rather than 180° phasing may be preferable because it is independent of perforation orientation (i.e., less risk and the perforating guns do not need to be oriented).

Fig. 7.6 is a summary for perforating horizontal wells. It shows that the selection of perforation phasing depends greatly on the degree of formation anisotropy. For highly anisotropic formations, all the perforations need to be oriented in the direction of the minimum permeability to give the maximum perforation productivity and hence 180° phasing will be the best completion technique. On the other hand, for slightly anisotropic formations, multidirectional phasings will provide higher perforation productivity than 0° and 180° phasings, which is similar to results for perforated vertical wells.

7.3 MINIMIZING FORMATION DAMAGE EFFECT FOR PERFORATED WELLS.

Fig. 7.7 shows guidelines for minimizing formation damage effect for cased and perforated wells. The most important thing is to perforate in the direction of minimum damage radius, $r_s(\alpha)$. Formation damage due to drilling mud filtration may distribute elliptically in anisotropic formations. In some literature, the minimum damage penetration is assumed to be parallel to the direction of minimum permeability (i.e.,

vertical direction). Perforating in the upper or lower sides of the well can provide chances to bypass through the damage zone, which minimizes the effect of formation damage. Even if all the perforations are terminated inside the damage zone, the effects of formation damage can be lower than those of openhole completions. Effectively perforated wells (i.e., $s_p < 0$) provide a larger effective wellbore radius, which slightly lowers skin factors. On the other hand, inefficient perforations (i.e., $s_p > 0$) results in severe formation damage effects since the convergent flow to perforations are magnified by the permeability reduction in the near-perforation vicinity.

7.4 MINIMIZING CRUSHED ZONE EFFECT FOR PERFORATED WELLS.

Fig. 7.8 shows guidelines for minimizing crushed zone effect for cased and perforated wells. As shown in Eqs. 5.98 and 5.99, the crushed zone effects are proportional to the perforation spacing and inversely proportional to the perforation length. Longer perforations and higher perforation shot densities, the radial flow region around a perforation become negligible. The flow field eventually reduces to 2D plane flow similar to fractured wells. Under these conditions, the damaged zone can be negligible. An analogous observation was discussed by Karakas and Tariq (1991).

When the perforation length and perforation shot density are not sufficiently high, a crushed zone will significantly impair the perforation productivity. However, if the formation perforated is highly anisotropic, you can decrease the crushed zone effect by applying 0° or 180° perforation phasings with proper perforation orientations. Locating all of the perforations parallel to the direction of minimum permeability increases the effective perforation length and lowers the skin factor.

7.5 DIAGNOSIS OF FORMATION DAMAGE EFFECT ON WELL COMPLETIONS.

The reduction in permeability of the near-wellbore formation due to the invasion of drilling and completion fluids can significantly affect well productivity. As presented in Chapter 4, the effect of formation damage on well completions is more significant for slotted or perforated liner than for openhole completions. In this section, how formation damage impairs the completion performance is discussed.

Fig. 7.9 compares the skin factors for various well completions: Case 1, an openhole completion ($r_w=0.25$ ft); Case 2, a cased and perforated well with an excellent perforation geometry ($l_p=12$ in. and $s_p^0=-1.20$), Case 3, a cased and perforated well with a good perforation geometry ($l_p=12$ in. $s_p^0=0.00$), and Case 4, a slotted liner ($s_{SL}^0=1.54$). For cased and perforated well completions with efficient perforating (i.e., $s_p<0$), skin factors are lower than those for the openhole completion. The perforations extending beyond the damage zone (i.e., $r_s<1.25$ ft) create flowpaths through the damage zone so that the effect of formation damage becomes less important. Even if all the perforations terminate inside the damaged zone (i.e., $r_s>1.25$ ft), skin factors can be less than openhole completions. The increase of skin where damage is deeper is almost parallel to Hawkins' formula.

On the other hand, slotted (perforated) liner completions are unsuitable for formations where severe permeability reduction is observed. The skin factor may significantly increase even for shallow penetration of damage since the reduced permeability magnifies skin factor due to the convergent flow to slots. To lower the damage effects requires either a excellent slot design to achieve $s_{SL}^0\approx 0$, or appropriate damage removable operations to recover the damaged permeability (e.g., acidizing).

Fig. 7.10 summarizes the effect of formation damage on different types of well completions relative to open hole wells. For shallow penetration of damage, cased and perforated wells are very efficient since perforations easily extend beyond the damage

zone. Cased and perforated well completions can also provide lower skin factors compared to those of open hole completions for deeper penetration of damage if the wells are efficiently perforated (i.e., $s_p^0 < 0$). In contrast, productivity of slotted (perforated) liner completions greatly depends on the severity of permeability damage (i.e., k_s/k) since convergent flow to slots and perforations are magnified even for shallow penetration of damage.

Table 7.1 Data for slotted liner study.

Entry	Unit	Value
r_w	in.	3.0
w_s	in.	0.005~0.3
l_s	in.	0.5~3.5
m_s	-	4~12
n_s	-	1~3
λ	-	0.2~0.8

Note: $w_u = (2n_s - 1)w_s$

Table 7.2 Data for perforated liner study.

Entry	Unit	Value
r_w	in.	3.0
r_p	in.	0.01~0.5
m_p	-	4~12
λ	-	0.2~0.8

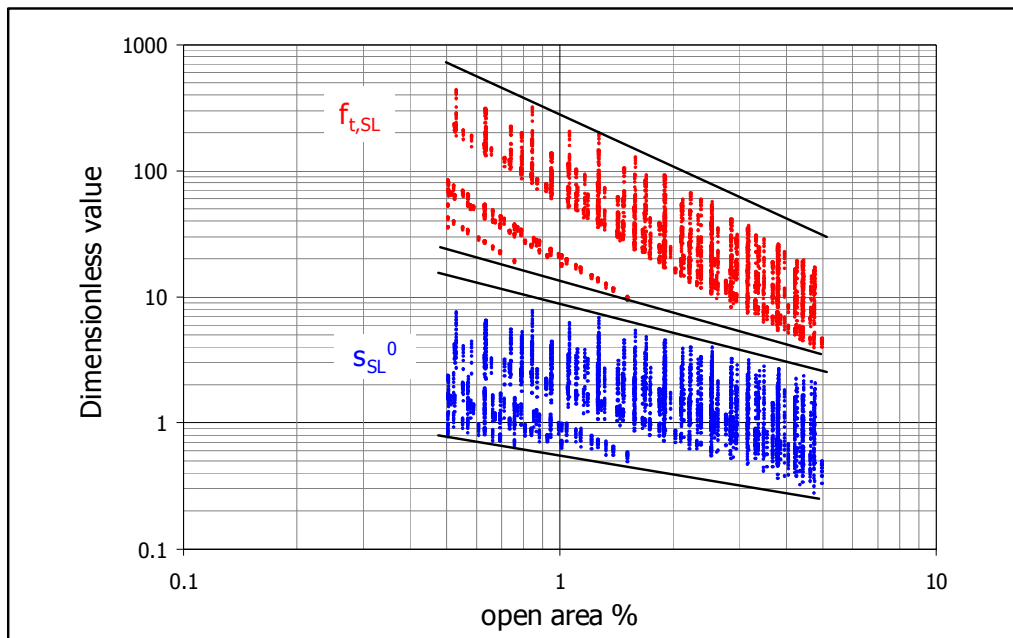


Fig. 7.1 Skin factor analysis of slotted liners (open slots).

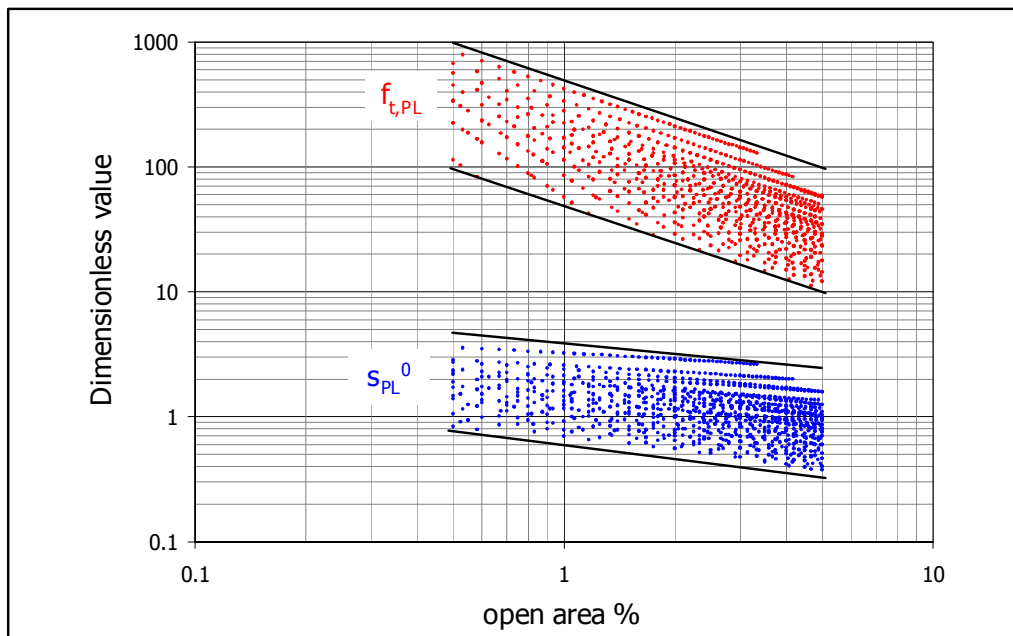


Fig. 7.2 Skin factor analysis of perforated liners.

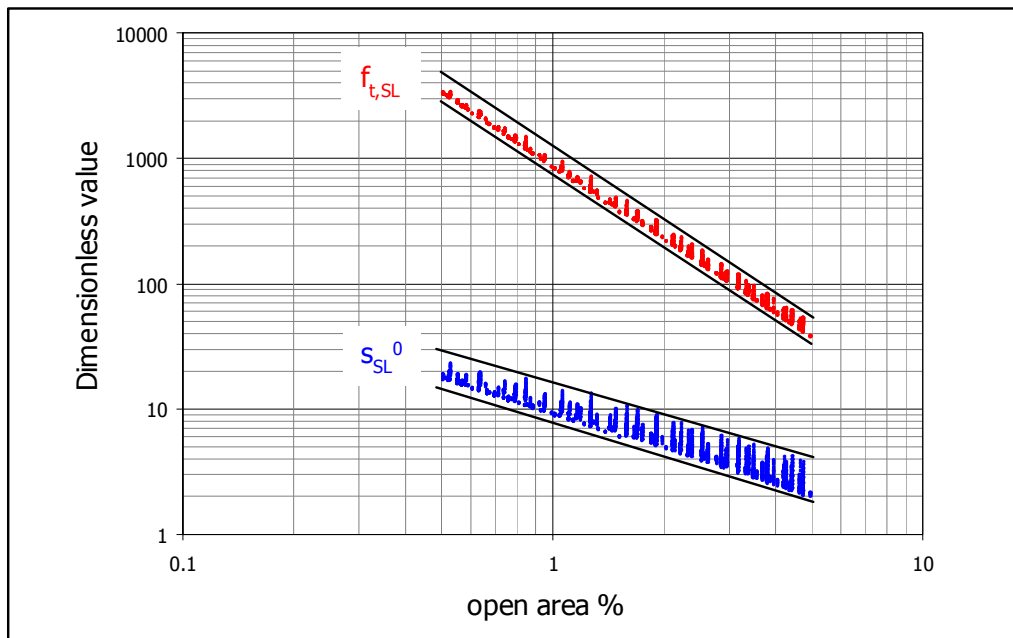


Fig. 7.3 Skin factor analysis of slotted liners (plugged slots).

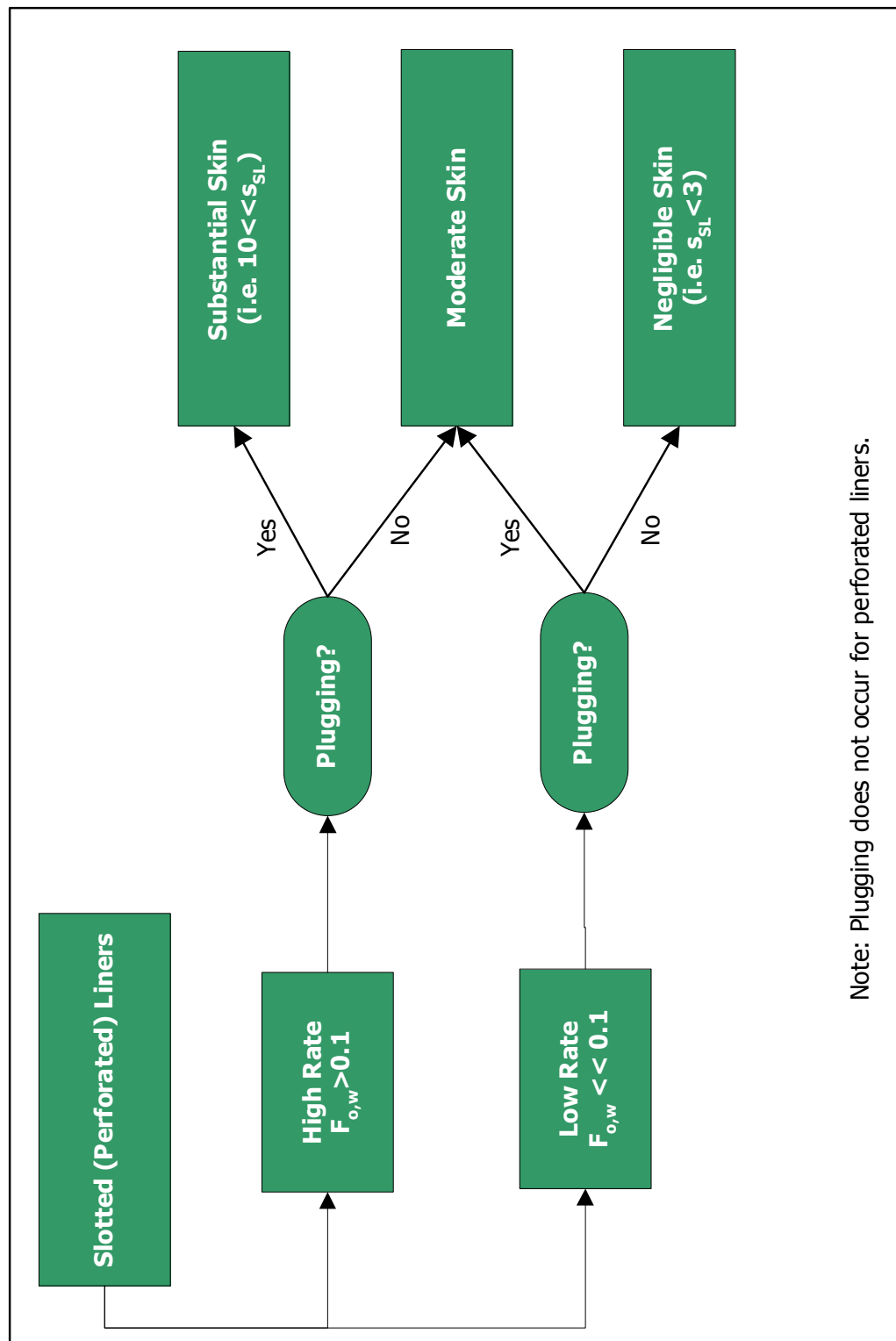


Fig. 7.4 Skin factor summary for liner completions.

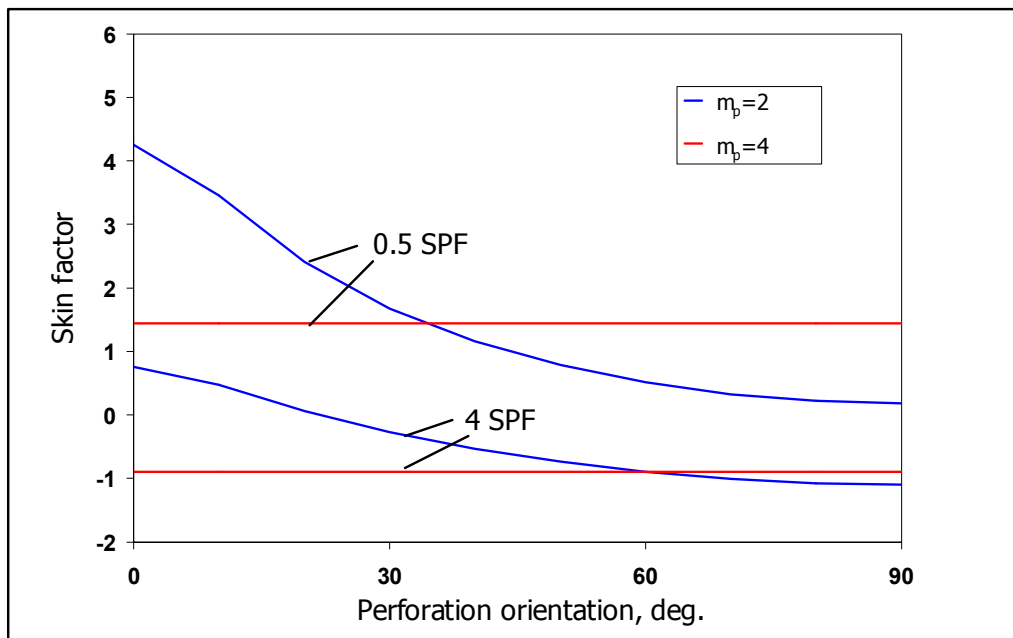


Fig. 7.5 Effect of perforation orientation on perforation skin factor.

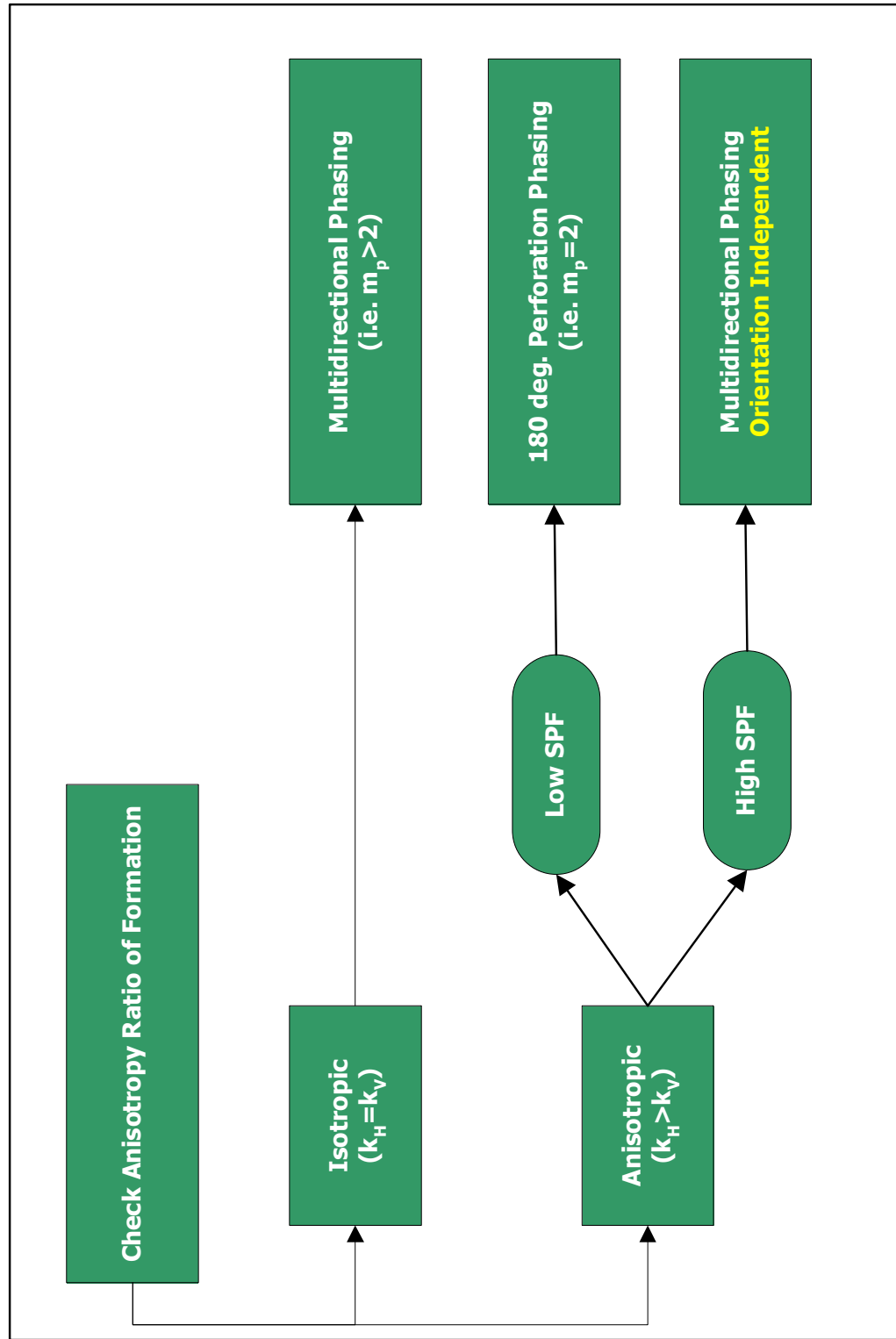


Fig. 7.6 Guidelines for perforating horizontal wells.

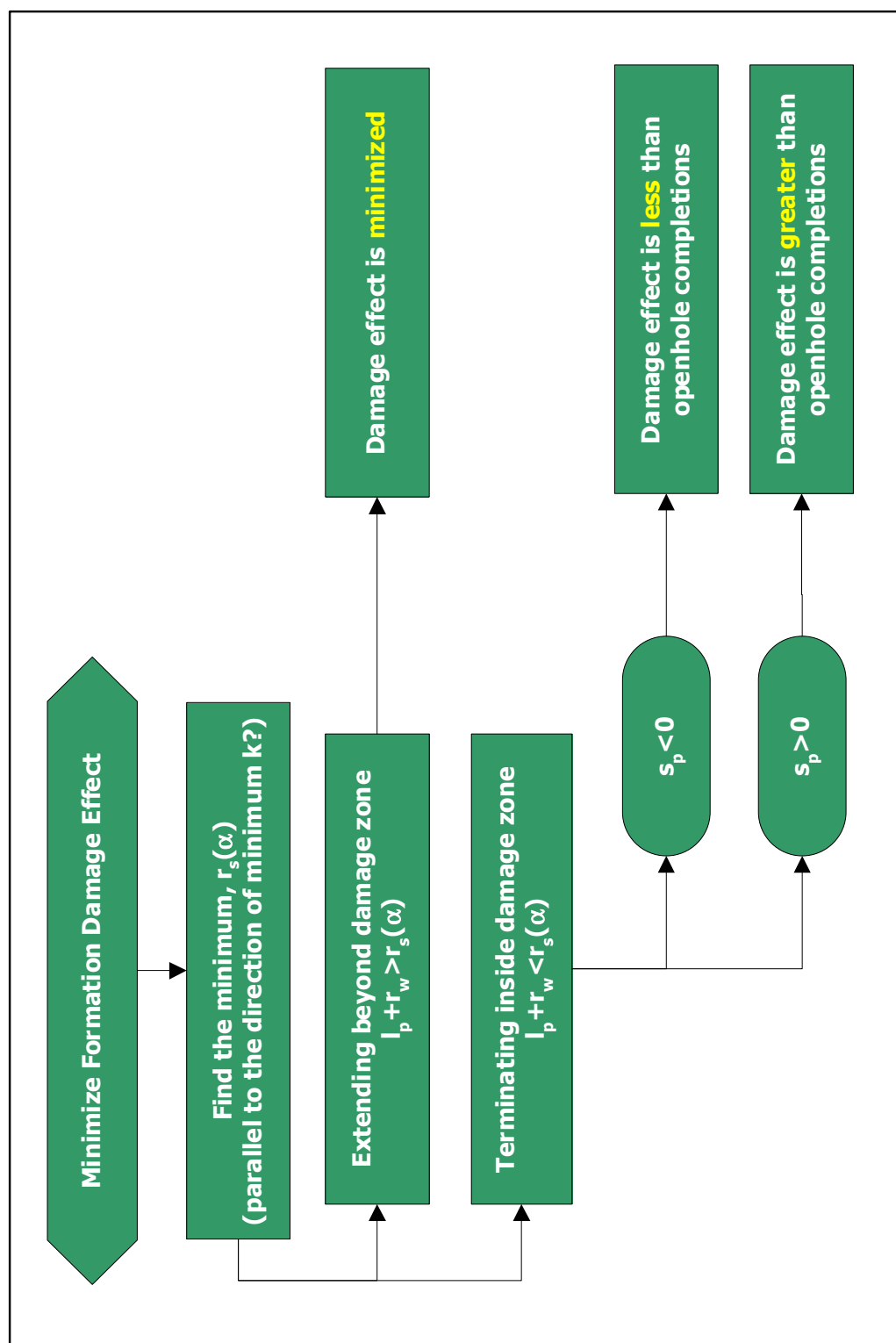


Fig. 7.7 Guidelines for minimizing formation damage effect.

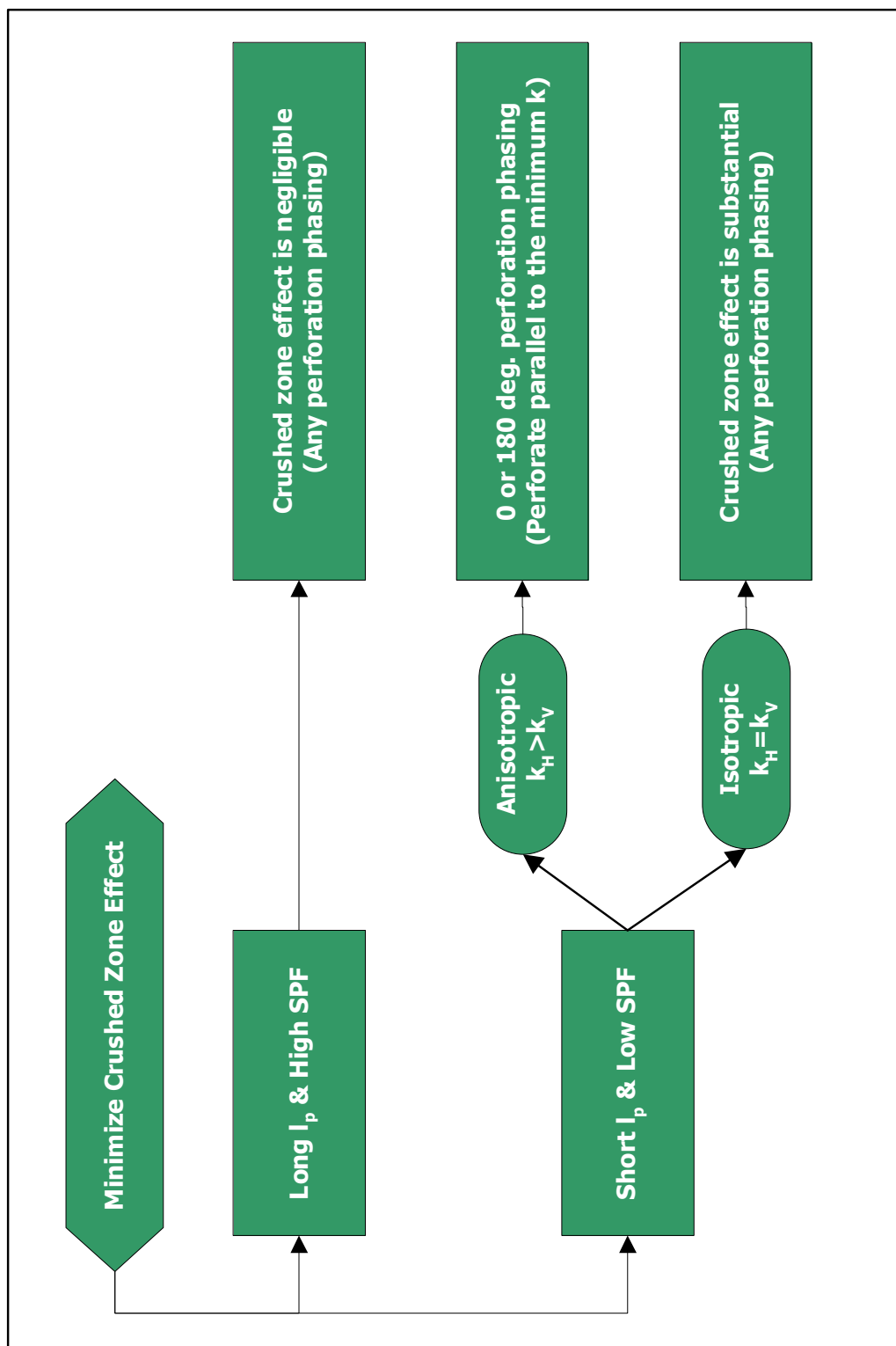


Fig. 7.8 Guidelines for minimizing crushed zone effect.

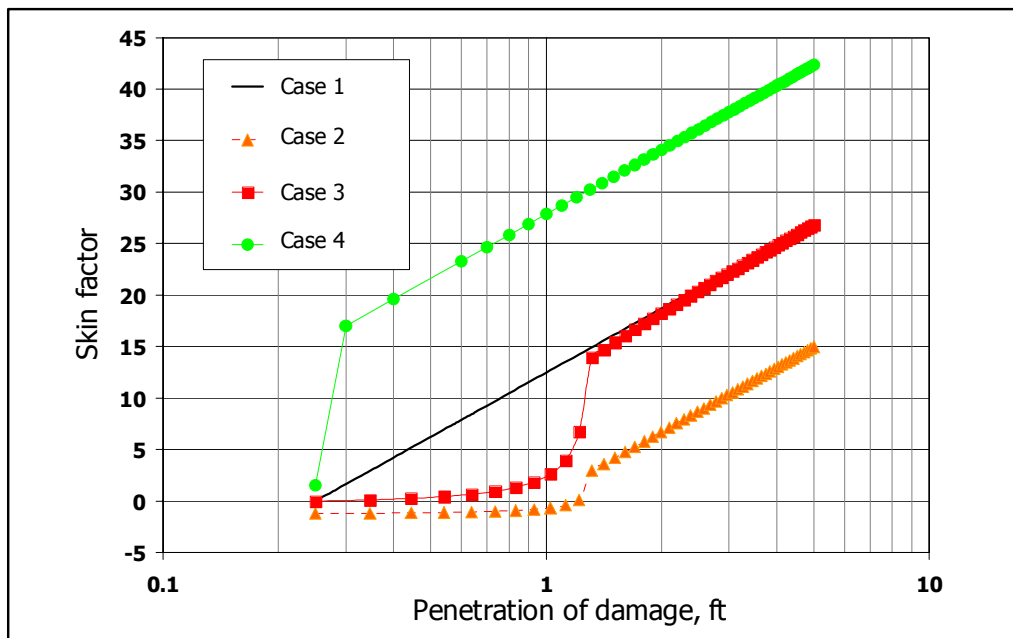


Fig. 7.9 Effect of formation damage on different well completions.

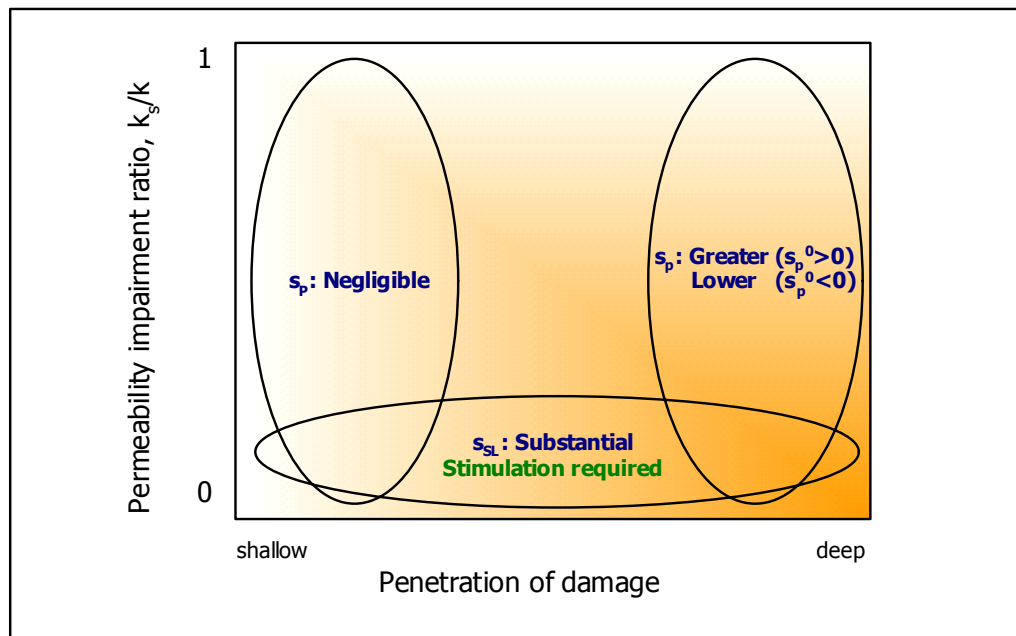


Fig. 7.10 Diagnosis of Formation Damage Effect.

CHAPTER 8

Conclusions

Using a general expression for skin factor, we developed comprehensive skin factor models for various types of horizontal well completions. The models account for the convergent flow to perforations and slots, formation and perforation damage, plugging of slots, gravel damage, and turbulence effects as well as the interactions among these effects. We also developed a 3D extensive FEM simulator to solve the complex flow field problems. The FEM simulations provide visual representations of the flow to horizontal well completions while avoiding use of significantly simplified assumptions and are used to validate the skin model.

The skin model shows that skin factors due to the turbulence effects for slotted or perforated liners can be tens of times more significant than openhole completions while the rate-independent skin factor may be negligible. If the slots are plugged by formation sand, the turbulence skin can be hundreds of times more significant. The results also show that formation damage in the near-well vicinity substantially increases skin factors for slotted or perforated liner completions even for shallow penetration of damage, while cased and perforated well completions can easily overcome the damaged zone effects. We also presented a skin factor equation to account for the transition from linear to spherical flow for cased and gravel packed wells. The model can be applied for any k/k_p (ratio of gravel to formation permeabilities) while the conventional linear flow model may give inaccurate skin factors for $k/k_p > 0.1$.

Our skin model can be used to design optimum well completions (e.g., slot and perforation patterns) and determine the magnitude of reduction of the formation

permeability and the severity of the plugging of slots. The model gives simple, analytical expressions for determining these effects and can be programmed without advanced computational skills. The model presented in this study clarifies the causes of high skin value under various production conditions and suggests techniques to minimize the problems.

Appendix A: Finite Element Simulator

A.1 FINITE ELEMENT FORMULATION

The first section of Appendix A is a brief review of the finite element formulation (Gartling and Hickox, 1982 and Reddy and Gartling, 2001). In this study the Galerkin form of the method of weighted residuals (MWR) are applied to produce an integral representation of the basic conservation laws. We consider the problem of finding the steady state pressure $p(x, y, z)$ distribution in a three dimensional orthotropic medium Ω with boundary Γ . The equation is given by:

$$-\left[\frac{\partial}{\partial x}\left(\hat{k}_{xx}\frac{\partial p}{\partial x}\right)+\frac{\partial}{\partial y}\left(\hat{k}_{yy}\frac{\partial p}{\partial y}\right)+\frac{\partial}{\partial z}\left(\hat{k}_{zz}\frac{\partial p}{\partial z}\right)\right]=Q \quad (\text{A.1})$$

where $Q(x, y, z)$ is the known internal source per unit volume. The boundary conditions are specified as

$$p = f^p(s) \quad \text{on } \Gamma_p \quad (\text{A.2})$$

$$u_n = \hat{k}_{xx}\frac{\partial p}{\partial x}n_x + \hat{k}_{yy}\frac{\partial p}{\partial y}n_y + \hat{k}_{zz}\frac{\partial p}{\partial z}n_z = f^u(s) \quad \text{on } \Gamma_u \quad (\text{A.3})$$

where Γ_p and Γ_u are disjoint portions of the boundary Γ such that $\Gamma = \Gamma_p \cup \Gamma_u$. (n_x, n_y, n_z) denote the direction cosines of the unit normal vector on the boundary.

Fig. A.1 shows the domain of a typical element by the symbol Ω^e and its boundary by Γ^e . The element Ω^e can be a tetrahedra or hexahedra in shape (triangle or quadrilateral in two-dimensional problem), and the degree of interpolation over it can be linear, quadratic, and so on. The non-overlapping sum (or assembly) of all elements used to represent the actual domain will be denoted by Ω^h , and it is called the finite element mesh of the domain Ω . The dependent unknown p is approximated over a typical finite element Ω^e by the expression

$$p(x, y, z) \approx p^e(x, y, z) = \sum_{j=1}^n p_j^e \psi_j^e(x, y, z) \quad (\text{A.4})$$

where $p^e(x, y, z)$ represents an approximation of $p(x, y, z)$ over the element Ω^e , p_j^e denote the values of the function $p^e(x, y, z)$ at a selected number of points, called element nodes, in the element Ω^e , and ψ_j^e are the approximation functions associated with the element.

Multiplying Eq. A.1 with a weight function w , and integrate the equation over the element domain Ω^e :

$$0 = \int_{\Omega^e} w \left[-\frac{\partial}{\partial x} \left(\hat{k}_{xx} \frac{\partial p^e}{\partial x} \right) - \frac{\partial}{\partial y} \left(\hat{k}_{yy} \frac{\partial p^e}{\partial y} \right) - \frac{\partial}{\partial z} \left(\hat{k}_{zz} \frac{\partial p^e}{\partial z} \right) - Q(x, y, z) \right] dx dy dz \quad (\text{A.5})$$

The expression in square brackets of the above equation represents a residual of the approximation of Eq. A.1, because $p^e(x, y, z)$ is only an approximation of $p(x, y, z)$.

Applying the Green-Gauss theorem on the first three terms in Eq. A.5

$$\begin{aligned} 0 = \int_{\Omega^e} \left(\hat{k}_{xx} \frac{\partial w}{\partial x} \frac{\partial p}{\partial x} + \hat{k}_{yy} \frac{\partial w}{\partial y} \frac{\partial p}{\partial y} + \hat{k}_{zz} \frac{\partial w}{\partial z} \frac{\partial p}{\partial z} - wQ \right) dx dy dz \\ - \oint_{\Gamma^e} w \left(\hat{k}_{xx} \frac{\partial p}{\partial x} n_x + \hat{k}_{yy} \frac{\partial p}{\partial y} n_y + \hat{k}_{zz} \frac{\partial p}{\partial z} n_z \right) ds \end{aligned} \quad (\text{A.6})$$

From an inspection of the boundary term in Eq. A.6, we note that the specification of p constitutes the essential boundary condition, and p is called the primary variable. The specification of the coefficient of the weight function in the boundary expression

$$u_n = \hat{k}_{xx} \frac{\partial p}{\partial x} n_x + \hat{k}_{yy} \frac{\partial p}{\partial y} n_y + \hat{k}_{zz} \frac{\partial p}{\partial z} n_z \quad (\text{A.7})$$

constitutes the natural boundary condition, and u_n is the secondary variable of the formulation. Substituting Eq. A.7 into Eq. A.6 gives

$$0 = \int_{\Omega^e} \left(\hat{k}_{xx} \frac{\partial w}{\partial x} \frac{\partial p}{\partial x} + \hat{k}_{yy} \frac{\partial w}{\partial y} \frac{\partial p}{\partial y} + \hat{k}_{zz} \frac{\partial w}{\partial z} \frac{\partial p}{\partial z} - wQ \right) dx dy dz - \oint_{\Gamma^e} w u_n ds \quad (\text{A.8})$$

The weak form in Eq. A.8 forms the basis of the finite element model of Eq. A.1. By substituting for p from Eq. A.4 and setting $w = \psi_1, \psi_2, \dots, \psi_n$ (for the Ritz-Galerkin

model), we obtain n algebraic equations from Eq. A.8. In Eq. A.4, ψ_j^e are the interpolation functions, with the property

$$\psi_i^e(x_j, y_j, z_j) = \delta_{ij} \quad (\text{A.9})$$

The specific form of ψ_j^e will be presented for various elements in the next section. Eq. A.4 can be written in matrix notation as

$$p(\mathbf{x}) = (\boldsymbol{\Psi}^e)^T \mathbf{p}^e \quad (\text{A.10})$$

where $(\boldsymbol{\Psi}^e)^T$ is a $(1 \times n_e)$ vector of interpolation functions of the element Ω_e

$$(\boldsymbol{\Psi}^e)^T = \{\psi_1^e \quad \psi_2^e \quad \cdots \quad \psi_{n_e}^e\} \quad (\text{A.11})$$

where \mathbf{p}^e is a $(n_e \times 1)$ vector of nodal pressures, superscript $(\cdot)^T$ denotes the transpose of a vector or matrix, and n_e is the number of nodal points in an element. Substituting the finite element approximation given by Eq. A.4 for p into the weak form, we obtain

$$0 = \int_{\Omega^e} \left\{ \frac{\partial w}{\partial x_i} \left[\hat{k}_{ij} \left(\sum_{k=1}^n p_k^e \frac{\partial \psi_k^e}{\partial x_j} \right) \right] - wQ \right\} dx dy dz - \oint_{\Gamma^e} w u_n ds \quad (\text{A.12})$$

Since we need n independent algebraic equations to solve for the n unknowns, $p_1^e, p_2^e, \dots, p_n^e$, we choose n independent functions for w : $w = \psi_1^e, \psi_2^e, \dots, \psi_n^e$. The i -th algebraic equation is obtained by substituting $w = \psi_i^e$ into Eq. A.8:

$$\sum_{j=1}^n K_{ij}^e p_j^e = Q_i^e + u_i^e \quad (\text{A.13})$$

where the coefficients K_{ij}^e , Q_i^e , and u_i^e are defined by

$$K_{ij}^e = \int_{\Omega^e} \left(\hat{k}_{mn} \frac{\partial \psi_i}{\partial x_m} \frac{\partial \psi_j}{\partial x_n} \right) dx dy dz \quad (\text{A.14})$$

$$Q_i^e = \int_{\Omega^e} Q \psi_i dx dy dz \quad (\text{A.15})$$

$$u_i^e = \oint_{\Gamma^e} u_n \psi_i ds \quad (\text{A.16})$$

In matrix notation, Eq. A.13 takes the form

$$[K^e(\mathbf{u})] \{p^e\} = \{Q^e\} + \{u^e\} \quad (\text{A.17})$$

or

$$\mathbf{K}^e(\mathbf{u})\mathbf{p}^e = \mathbf{Q}^e + \mathbf{u}^e \quad (\text{A.18})$$

The matrix $[\mathbf{K}^e]$ is called the coefficient matrix, or conductivity matrix. Eq. A.17 is called the finite element model of Eq. A.1. The element coefficient matrices and vectors are written in vector form as

$$\mathbf{K}^e = \int_{\Omega^e} \frac{\partial \Psi}{\partial x_m} \hat{k}_{mn} \frac{\partial \Psi^T}{\partial x_n} d\mathbf{x} \quad (\text{A.19})$$

$$\mathbf{Q}^e = \int_{\Omega^e} \Psi Q d\mathbf{x} \quad (\text{A.20})$$

$$\mathbf{u}^e = \oint_{\Gamma^e} \Psi u_n ds \quad (\text{A.21})$$

The assembled matrices are symbolically represented as

$$\mathbf{K} = \sum_e \mathbf{K}^e; \quad \mathbf{F} = \sum_e \mathbf{F}^e, \quad \mathbf{F} = \mathbf{Q}^e + \mathbf{u}^e \quad (\text{A.22})$$

In Eq. A.22 the sum is taken over all elements in the mesh, and the element matrices are defined by Eqs. A.19, A.20, and A.21. Once the form of the element interpolation functions Ψ^e is known and the element geometry is specified, the integrals can be evaluated, and the global (assembled) equations are then constructed through use of Eq. A.22:

$$\mathbf{K}(\mathbf{u})\mathbf{p} = \mathbf{F} \quad (\text{A.23})$$

The formulation represented by Eq. A.23 requires that the flux field be computed from Forchheimer equation for a given pressure field. The discretized form of Forchheimer equation is

$$\mathbf{M}\mathbf{u} = -\mathbf{H}(\mathbf{u})\mathbf{p} \quad (\text{A.24})$$

where

$$\mathbf{M} = \int_{\Omega} \Psi \Psi^T d\mathbf{x} \quad (\text{A.25})$$

$$\mathbf{H} = \int_{\Omega} \Psi \hat{k}_{ij} \frac{\partial \Psi^T}{\partial x_j} d\mathbf{x} \quad (\text{A.26})$$

The solution of the above equation requires that the equation be assembled and the \mathbf{M} matrix then reduced to upper triangular form (via Gauss elimination). The solution of Eq. A.24 may be less expensive if the \mathbf{M} matrix is converted to a diagonal form:

$$\mathbf{u} = -\mathbf{M}^{-1}\mathbf{H}(\mathbf{u})\mathbf{p} \quad (\text{A.27})$$

where the inverse of \mathbf{M} has particularly simple form. From Eq. A.28 we note that the \mathbf{M} matrix is constructed from the inner product of two basis functions (i.e., bilinear functions). This construction may be accurately diagonalized (or lumped) by a simple matrix row sum technique.

Because of the computational expense of such a procedure, IWPCOMPS uses alternative method to calculate the velocity. Further reductions in computation are possible if Eq. A.24 is replaced by the original differential statement of Forchheimer equation:

$$u_i = -\hat{k}_{ij}(\mathbf{u}) \frac{\partial p}{\partial x_j} \quad (\text{A.28})$$

Using the appropriate finite element expression for pressure allows Eq. A.28 to be written

$$u_i = -\hat{k}_{ij}(\mathbf{u}) \frac{\partial \Psi^T}{\partial x_j} \mathbf{p} \quad (\text{A.29})$$

The above expression may be evaluated at any point within the element to yield the velocity components at that point. During calculations of the coefficient matrices, the velocity component u_i are computed at the numerical quadrature (Gauss) points of the element. Such a process is particularly efficient since no matrix assembly or solution is required. However, as a result of eliminating the matrix assembly process, inter-element continuity of the velocity field can no longer be enforced and the velocities are discontinuous between elements.

A.2 ELEMENT AND ELEMENT MATRIX CONSTRUCTION

The triangular elements used in two-dimensional applications of IWPCOMPS consist of a straight-sided, three-node element and a six-node element as shown in Fig A.2. For triangular elements, it is possible to construct three non-dimensional coordinates L_i ($i=1, 2, 3$), which vary in a direction normal to the sides directly opposite each node. The coordinates are defined such that

$$L_i = \frac{A_i}{A} \quad (\text{A.30})$$

$$A = \sum_{i=1}^3 A_i \quad (\text{A.31})$$

where A_i is the area of the triangular formed by nodes j and k and an arbitrary point P in the element, and A is the total area of the element. The linear interpolation function for the three-node element is given by

$$\{\psi^e\} = \begin{Bmatrix} L_1 \\ L_2 \\ L_3 \end{Bmatrix} \quad (\text{A.32})$$

and the corresponding quadratic function for the six-node element is

$$\{\psi^e\} = \begin{Bmatrix} L_1(2L_1 - 1) \\ L_2(2L_2 - 1) \\ L_3(2L_3 - 1) \\ 4L_1L_2 \\ 4L_2L_3 \\ 4L_3L_1 \end{Bmatrix} \quad (\text{A.33})$$

The ordering of the functions in Eqs. A.32 and A.33 corresponds to the ordering of the nodes shown in Fig. A.2. The shape functions are expressed in terms of the area or natural coordinates, L_i , for a triangle which range from 0 to 1, and are related by the auxiliary condition $L_1 + L_2 + L_3 = 1$ (i.e., there are only two independent area coordinates).

Two types of quadrilateral elements are used in IWPCOMPS – a four-node and an eight-node element. For the linear, four node element the interpolation functions are given by

$$\{\psi^e\} = \frac{1}{4} \begin{Bmatrix} (1-\xi)(1-\eta) \\ (1+\xi)(1-\eta) \\ (1+\xi)(1+\eta) \\ (1-\xi)(1+\eta) \end{Bmatrix} \quad (\text{A.34})$$

The ordering of the functions in Eq. A.34 corresponds to the nodal point ordering shown in Fig. A.3. The interpolation functions are written in terms of the normalized or natural coordinates for the element, ξ , η , which vary from -1 to $+1$. The eight-node element uses the biquadratic, “serendipity” functions given by

$$\{\psi^e\} = \frac{1}{4} \begin{Bmatrix} (1-\xi)(1-\eta)(-\xi-\eta-1) \\ (1+\xi)(1-\eta)(+\xi-\eta-1) \\ (1+\xi)(1+\eta)(+\xi+\eta-1) \\ (1-\xi)(1+\eta)(-\xi+\eta-1) \\ 2(1-\xi^2)(1-\eta) \\ 2(1+\xi)(1-\eta^2) \\ 2(1-\xi^2)(1+\eta) \\ 2(1-\xi)(1-\eta^2) \end{Bmatrix} \quad (\text{A.35})$$

The standard tetrahedral elements are a three-dimensional version of the triangular elements. The four-node linear and ten-node quadratic tetrahedral elements are shown in Fig. A.4, and their interpolation functions are

$$\{\psi^e\} = \begin{Bmatrix} L_1 \\ L_2 \\ L_3 \\ L_4 \end{Bmatrix} \quad (\text{A.36})$$

$$\{\psi^e\} = \begin{Bmatrix} L_1(2L_1-1) \\ L_2(2L_2-1) \\ L_3(2L_3-1) \\ L_4(2L_4-1) \\ 4L_1L_2 \\ 4L_2L_3 \\ 4L_3L_1 \\ 4L_1L_4 \\ 4L_2L_4 \\ 4L_3L_4 \end{Bmatrix} \quad (\text{A.37})$$

The volume coordinates, L_i , are used to describe the interpolation functions for linear and quadratic elements, where $L_1+L_2+L_3+L_4=1$.

Brick elements represent the most commonly used finite elements for three-dimensional analysis, and the straight-sided, linear eight-node brick element is the most cost-effective choice (Fig. A.5). The interpolation functions of the linear element are given in terms of the normalized coordinates (ξ, η, ζ) as follows:

$$\{\psi^e\} = \frac{1}{8} \begin{Bmatrix} (1-\xi)(1-\eta)(1-\zeta) \\ (1+\xi)(1-\eta)(1-\zeta) \\ (1+\xi)(1+\eta)(1-\zeta) \\ (1-\xi)(1+\eta)(1-\zeta) \\ (1-\xi)(1-\eta)(1+\zeta) \\ (1+\xi)(1-\eta)(1+\zeta) \\ (1+\xi)(1+\eta)(1+\zeta) \\ (1-\xi)(1+\eta)(1+\zeta) \end{Bmatrix} \quad (\text{A.38})$$

The quadratic shape functions for the twenty-node serendipity element are given by

$$\{\psi^e\} = \frac{1}{8} \left\{ \begin{array}{l} (1-\xi)(1-\eta)(1-\varsigma)(-\xi-\eta-\varsigma-2) \\ (1+\xi)(1-\eta)(1-\varsigma)(+\xi-\eta-\varsigma-2) \\ (1+\xi)(1+\eta)(1-\varsigma)(+\xi+\eta-\varsigma-2) \\ (1-\xi)(1+\eta)(1-\varsigma)(-\xi+\eta-\varsigma-2) \\ (1-\xi)(1-\eta)(1+\varsigma)(-\xi-\eta+\varsigma-2) \\ (1+\xi)(1-\eta)(1+\varsigma)(+\xi-\eta+\varsigma-2) \\ (1+\xi)(1+\eta)(1+\varsigma)(+\xi+\eta+\varsigma-2) \\ (1-\xi)(1+\eta)(1+\varsigma)(-\xi+\eta+\varsigma-2) \\ 2(1-\xi^2)(1-\eta)(1-\varsigma) \\ 2(1+\xi)(1-\eta^2)(1-\varsigma) \\ 2(1-\xi^2)(1+\eta)(1-\varsigma) \\ 2(1-\xi)(1-\eta^2)(1-\varsigma) \\ 2(1-\xi)(1-\eta)(1-\varsigma^2) \\ 2(1+\xi)(1-\eta)(1-\varsigma^2) \\ 2(1+\xi)(1+\eta)(1-\varsigma^2) \\ 2(1-\xi)(1+\eta)(1-\varsigma^2) \\ 2(1-\xi^2)(1-\eta)(1+\varsigma) \\ 2(1+\xi)(1-\eta^2)(1+\varsigma) \\ 2(1-\xi^2)(1+\eta)(1+\varsigma) \\ 2(1-\xi)(1-\eta^2)(1+\varsigma) \end{array} \right\} \quad (\text{A.39})$$

The transformation between the actual element Ω^e and the master element $\hat{\Omega}$ [or equivalently, between (x, y, z) and (ξ, η, ζ)] is accomplished by a coordinate transformation of the form

$$x = \sum_{j=1}^m x_j^e \varphi_j^e(\xi, \eta, \varsigma) \quad (\text{A.40})$$

$$y = \sum_{j=1}^m y_j^e \varphi_j^e(\xi, \eta, \varsigma) \quad (\text{A.41})$$

$$z = \sum_{j=1}^m z_j^e \varphi_j^e(\xi, \eta, \varsigma) \quad (\text{A.42})$$

where φ_j denote the finite element interpolation functions of the master element $\hat{\Omega}$. The coordinates in the master element are chosen to be the natural coordinates (ξ, η, ζ) such

that $-1 \leq (\xi, \eta, \zeta) \leq 1$. This choice is dictated by the limits of integration in the Gauss quadrature rule, which is used to evaluate the integrals. The transformation A.40, A.41 and A.42 map a point (ξ, η, ζ) in the master element $\hat{\Omega}$ onto a point (x, y, z) in element Ω^e , and vice versa if the Jacobian of the transformation is positive-definite.

The construction of the various finite element coefficient matrices requires the integration of combinations of the interpolation functions and their spatial derivatives over the volume (area) of the element. The derivatives are expressed by

$$\begin{pmatrix} \frac{\partial \psi_i}{\partial \xi} \\ \frac{\partial \psi_i}{\partial \eta} \\ \frac{\partial \psi_i}{\partial \zeta} \end{pmatrix} = \begin{bmatrix} \frac{\partial x}{\partial \xi} & \frac{\partial y}{\partial \xi} & \frac{\partial z}{\partial \xi} \\ \frac{\partial x}{\partial \eta} & \frac{\partial y}{\partial \eta} & \frac{\partial z}{\partial \eta} \\ \frac{\partial x}{\partial \zeta} & \frac{\partial y}{\partial \zeta} & \frac{\partial z}{\partial \zeta} \end{bmatrix} \begin{pmatrix} \frac{\partial \psi_i}{\partial x} \\ \frac{\partial \psi_i}{\partial y} \\ \frac{\partial \psi_i}{\partial z} \end{pmatrix} = \begin{bmatrix} J_{11} & J_{12} & J_{13} \\ J_{21} & J_{22} & J_{23} \\ J_{31} & J_{32} & J_{33} \end{bmatrix} \begin{pmatrix} \frac{\partial \psi_i}{\partial x} \\ \frac{\partial \psi_i}{\partial y} \\ \frac{\partial \psi_i}{\partial z} \end{pmatrix} = [J] \begin{pmatrix} \frac{\partial \psi_i}{\partial x} \\ \frac{\partial \psi_i}{\partial y} \\ \frac{\partial \psi_i}{\partial z} \end{pmatrix} \quad (\text{A.43})$$

where $[J]$ is the Jacobian of the transformation from global coordinates (x, y, z) to the local element coordinates (ξ, η, ζ) . The parametric transformation defined in Eqs. A.40, A.41 and A.42 can be used to define the components of $[J]$:

$$[J] = \begin{bmatrix} \sum_{j=1}^m x_j \frac{\partial \phi_j^e}{\partial \xi} & \sum_{j=1}^m y_j \frac{\partial \phi_j^e}{\partial \xi} & \sum_{j=1}^m z_j \frac{\partial \phi_j^e}{\partial \xi} \\ \sum_{j=1}^m x_j \frac{\partial \phi_j^e}{\partial \eta} & \sum_{j=1}^m y_j \frac{\partial \phi_j^e}{\partial \eta} & \sum_{j=1}^m z_j \frac{\partial \phi_j^e}{\partial \eta} \\ \sum_{j=1}^m x_j \frac{\partial \phi_j^e}{\partial \zeta} & \sum_{j=1}^m y_j \frac{\partial \phi_j^e}{\partial \zeta} & \sum_{j=1}^m z_j \frac{\partial \phi_j^e}{\partial \zeta} \end{bmatrix} \quad (\text{A.44})$$

Inverting Eq. A.43, we obtain the global spatial derivatives of the interpolation functions in terms of the local derivatives:

$$\begin{pmatrix} \frac{\partial \psi_i}{\partial x} \\ \frac{\partial \psi_i}{\partial y} \\ \frac{\partial \psi_i}{\partial z} \end{pmatrix} = [J]^{-1} \begin{pmatrix} \frac{\partial \psi_i}{\partial \xi} \\ \frac{\partial \psi_i}{\partial \eta} \\ \frac{\partial \psi_i}{\partial \zeta} \end{pmatrix} = \begin{bmatrix} J_{11}^* & J_{12}^* & J_{13}^* \\ J_{21}^* & J_{22}^* & J_{23}^* \\ J_{31}^* & J_{32}^* & J_{33}^* \end{bmatrix} \begin{pmatrix} \frac{\partial \psi_i}{\partial \xi} \\ \frac{\partial \psi_i}{\partial \eta} \\ \frac{\partial \psi_i}{\partial \zeta} \end{pmatrix} \quad (\text{A.45})$$

where $[J]^{-1}$ is the inverse of the Jacobian matrix $[J]$. The components J_{ij}^* are complex functions of the components of $[J]$ that can be obtained by inverting the 3×3 Jacobian matrix. In practice, the Jacobian is usually inverted numerically. For the two-dimensional case the above equations are simplified substantially and permit analytic manipulation of the resulting 2×2 matrix.

In performing numerical integration over the element volume, it is necessary to transform the integrand and limits of integration from the global coordinates to the local element coordinates. The differential elemental volume transforms according to

$$d\Omega = dx dy dz = |[J]| d\xi d\eta d\zeta \quad (\text{A.46})$$

where $|[J]|$ indicates the determinant of the Jacobian matrix J . In the above equations the ξ , η , ζ variables for a brick element have been used.

Consider first the problem of evaluating finite element matrices that contain a variable coefficient. The xx -component of the diffusion matrix is

$$\mathbf{K}_{xx} = \int_{\Omega_e} \frac{\partial \Psi}{\partial x} \hat{k} \frac{\partial \Psi^T}{\partial x} dx \quad (\text{A.47})$$

when the conductivity is variable, the matrix in Eq. A.47 must be reevaluated each time new values of the flux are produced during the solution procedure. One standard method for treating this variable coefficient simply involves recomputing the matrix for each new set of conductivities. For each element the flux is evaluated at the quadrature points via the basis functions, thus permitting the conductivity to be evaluated at the quadrature locations. The matrix coefficients are then computed by the standard quadrature procedure. IWPCOMPS employs this technique, but the work involved in such a procedure can become large when considering anisotropic conductivities and/or higher-order elements.

The flux associated with Forchheimer equation can be computed on an element-by-element basis. The fluid flux are given by

$$u_x = -\hat{k}_{xx} \frac{\partial p}{\partial x} - \hat{k}_{xy} \frac{\partial p}{\partial y} - \hat{k}_{xz} \frac{\partial p}{\partial z} \quad (\text{A.48})$$

$$u_y = -\hat{k}_{yx} \frac{\partial p}{\partial x} - \hat{k}_{yy} \frac{\partial p}{\partial y} - \hat{k}_{yz} \frac{\partial p}{\partial z} \quad (\text{A.49})$$

$$u_z = -\hat{k}_{zx} \frac{\partial p}{\partial x} - \hat{k}_{zy} \frac{\partial p}{\partial y} - \hat{k}_{zz} \frac{\partial p}{\partial z} \quad (\text{A.50})$$

The flux components are computed by using the standard finite element approximations for p ,

$$p(\mathbf{x}_i) = \boldsymbol{\Psi}^T(\mathbf{x}_i) \mathbf{p} \quad (\text{A.51})$$

Using these definitions the flux components become

$$\begin{pmatrix} u_x \\ u_y \\ u_z \end{pmatrix} = - \begin{pmatrix} \hat{k}_{xx} & \hat{k}_{xy} & \hat{k}_{xz} \\ \hat{k}_{yx} & \hat{k}_{yy} & \hat{k}_{yz} \\ \hat{k}_{zx} & \hat{k}_{zy} & \hat{k}_{zz} \end{pmatrix} \begin{pmatrix} J_{11}^* & J_{12}^* & J_{13}^* \\ J_{21}^* & J_{22}^* & J_{23}^* \\ J_{31}^* & J_{32}^* & J_{33}^* \end{pmatrix} \begin{pmatrix} \partial \boldsymbol{\Psi}^T / \partial \xi \\ \partial \boldsymbol{\Psi}^T / \partial \eta \\ \partial \boldsymbol{\Psi}^T / \partial \zeta \end{pmatrix} \mathbf{p} \quad (\text{A.52})$$

in the vector form,

$$\mathbf{u} = -\hat{\mathbf{k}} \mathbf{J}^{-1} \mathbf{B} \mathbf{p} \quad (\text{A.53})$$

where

$$\mathbf{B} = \begin{pmatrix} J_{11}^* & J_{12}^* & J_{13}^* \\ J_{21}^* & J_{22}^* & J_{23}^* \\ J_{31}^* & J_{32}^* & J_{33}^* \end{pmatrix} \begin{pmatrix} \partial \boldsymbol{\Psi}^T / \partial \xi \\ \partial \boldsymbol{\Psi}^T / \partial \eta \\ \partial \boldsymbol{\Psi}^T / \partial \zeta \end{pmatrix} \quad (\text{A.54})$$

Since Eq. A.53 is nonlinear, it cannot be solved explicitly. Eq. A.53 is written by

$$\hat{\mathbf{k}}^{-1} \mathbf{u} = -\mathbf{B} \mathbf{p} \quad (\text{A.55})$$

or

$$(\mu \mathbf{k}^{-1} + \beta \rho | \mathbf{u} |) \mathbf{u} = -\mathbf{B} \mathbf{p} \quad (\text{A.56})$$

The above nonlinear equation is solved using Newton-Raphson method in IWPCOMPS.

Define the residual equation $g(\mathbf{u}) = 0$ of Eq. A.56:

$$\mathbf{g}(\mathbf{u}) = \mathbf{B} \mathbf{p} + (\mu \mathbf{k}^{-1} + \beta \rho | \mathbf{u} |) \mathbf{u} \quad (\text{A.57})$$

Considering the Jacobian matrix of the first order partial derivative

$$\mathbf{Dg} = \begin{bmatrix} \frac{\partial g_1}{\partial u_1} & \frac{\partial g_1}{\partial u_2} & \frac{\partial g_1}{\partial u_3} \\ \frac{\partial g_2}{\partial u_1} & \frac{\partial g_2}{\partial u_2} & \frac{\partial g_2}{\partial u_3} \\ \frac{\partial g_3}{\partial u_1} & \frac{\partial g_3}{\partial u_2} & \frac{\partial g_3}{\partial u_3} \end{bmatrix} \quad (\text{A.58})$$

where

$$\frac{\partial g_i}{\partial u_j} = \mu(k^{-1})_{ij} + \beta_{ij}\rho|\mathbf{u}| + \beta_{ik}\rho u_k \frac{u_j}{|\mathbf{u}|} \quad (\text{A.59})$$

Newton's iteration procedure is defined by

$$\mathbf{u}^{(n+1)} = \mathbf{u}^{(n)} - (\mathbf{Dg}^{-1})^{(n)} \mathbf{g}^{(n)} \quad (\text{A.60})$$

The starting value of the iteration $\mathbf{u}^{(0)}$ is set for the Darcy velocity that is given in the explicit form:

$$\mathbf{u}^{(0)} = -\mathbf{kBp} \quad (\text{A.61})$$

Note that fluxes computed from pressure gradients are discontinuous between elements. In case of producing a continuous flux distribution at nodes, the integration point flux values are linearly extrapolated to the nodes of each element and averaged between all connected elements.

With the previous definitions it is now possible to derive a computational form for the matrix coefficients involved in the finite element equations. We consider the cross (xy) component in the (1,2) coefficient of K^e ,

$$(K_{12}^e)_{xy} = \int_{\Omega^e} \hat{k}_{xy} \frac{\partial \psi_1}{\partial x} \frac{\partial \psi_2}{\partial y} dx dy dz \quad (\text{A.62})$$

which will be evaluated for a three-dimensional, brick element as

$$\begin{aligned} (K_{12}^e)_{xy} = \int_{-1}^{+1} \int_{-1}^{+1} \int_{-1}^{+1} \hat{k}_{xy}(u) & \left(J_{11}^* \frac{\partial \psi_1}{\partial \xi} + J_{12}^* \frac{\partial \psi_1}{\partial \eta} + J_{13}^* \frac{\partial \psi_1}{\partial \zeta} \right) \\ & \cdot \left(J_{21}^* \frac{\partial \psi_2}{\partial \xi} + J_{22}^* \frac{\partial \psi_2}{\partial \eta} + J_{23}^* \frac{\partial \psi_2}{\partial \zeta} \right) |J| d\xi d\eta d\zeta \end{aligned} \quad (\text{A.63})$$

Each component of the integral in Eq. A.63 is of the form

$$I = \int_{-1}^{+1} \int_{-1}^{+1} \int_{-1}^{+1} F(\xi, \eta, \varsigma) d\xi d\eta d\varsigma \quad (\text{A.64})$$

Applying the Gauss quadrature formula

$$\int_{-1}^{+1} \int_{-1}^{+1} \int_{-1}^{+1} F(\xi, \eta, \varsigma) d\xi d\eta d\varsigma \approx \sum_{I=1}^M \sum_{J=1}^N \sum_{K=1}^P F(\xi_I, \eta_J, \varsigma_K) W_I W_J W_K \quad (\text{A.65})$$

For brick elements it is typical to employ a product rule with $M=N=P=2$ or 3.

The nodal flux u_i^e due to applied boundary conditions need only be computed for those element sides that coincide with the boundary of the problem domain; contributions from interior element boundaries are canceled by adjoining elements. The surface flux vector is given by

$$\mathbf{u}^e = \oint_{\Gamma_e} \psi u_i n_i ds \quad (\text{A.66})$$

where Γ_e denotes the boundary surface of the element and $u_i n_i$ is the total fluid flux normal to the surface.

The computation of the indicated surface integral is most easily carried out in the normalized or natural coordinate system for the face (edge) of an element. This requires that the elemental surface are ds , or element edge length ds , be related to the local surface coordinates. Consider the typical quadrilateral element face shown in Fig. A.6, where the vectors \mathbf{e}_1 and \mathbf{e}_2 are defined as being tangent to the curvilinear coordinates, ξ_s and η_s . The elemental area ds in terms of the global coordinates (x, y, z) is related to an elemental area in surface coordinates by

$$ds = |\mathbf{J}_s| d\xi_s d\eta_s \quad (\text{A.67})$$

where \mathbf{J}_s is the Jacobian of the coordinate transformation and $|\cdot|$ indicates the determinant.

The determinant of the Jacobian can be written in terms of the vectors $(\mathbf{e}_1, \mathbf{e}_2)$ as

$$|\mathbf{J}_s| = |\mathbf{e}_1 \times \mathbf{e}_2| = [(\mathbf{e}_1 \cdot \mathbf{e}_1)(\mathbf{e}_2 \cdot \mathbf{e}_2) - (\mathbf{e}_1 \cdot \mathbf{e}_2)^2]^{1/2} \quad (\text{A.68})$$

The vectors \mathbf{e}_i can be expressed in terms of the global coordinates by

$$\mathbf{e}_1 = \begin{Bmatrix} \frac{\partial x}{\partial \xi_s} \\ \frac{\partial y}{\partial \xi_s} \\ \frac{\partial z}{\partial \xi_s} \end{Bmatrix}, \mathbf{e}_2 = \begin{Bmatrix} \frac{\partial x}{\partial \eta_s} \\ \frac{\partial y}{\partial \eta_s} \\ \frac{\partial z}{\partial \eta_s} \end{Bmatrix} \quad (\text{A.69})$$

Using the coordinate transformation, we can write

$$\mathbf{e}_1 = \begin{Bmatrix} \sum_{i=1}^{n_s} x_i^e \frac{\partial \hat{\psi}_i^e}{\partial \xi_s} \\ \sum_{i=1}^{n_s} y_i^e \frac{\partial \hat{\psi}_i^e}{\partial \xi_s} \\ \sum_{i=1}^{n_s} z_i^e \frac{\partial \hat{\psi}_i^e}{\partial \xi_s} \end{Bmatrix}, \mathbf{e}_2 = \begin{Bmatrix} \sum_{i=1}^{n_s} x_i^e \frac{\partial \hat{\psi}_i^e}{\partial \eta_s} \\ \sum_{i=1}^{n_s} y_i^e \frac{\partial \hat{\psi}_i^e}{\partial \eta_s} \\ \sum_{i=1}^{n_s} z_i^e \frac{\partial \hat{\psi}_i^e}{\partial \eta_s} \end{Bmatrix} \quad (\text{A.70})$$

where the $\hat{\cdot}$ indicates the restriction of the interpolation functions to an element face and n_s is the number of nodes defining the surface. The functions $\hat{\psi}_i$ may be either linear or quadratic, depending on the type of mapping used to describe the element geometry. Eq. A.85 provides a means for computing $|\mathbf{J}_s|$, which can be used in Eq. A.82. The unit normal vector \mathbf{n} is also defined by

$$\mathbf{n} = \frac{\mathbf{e}_1 \times \mathbf{e}_2}{|\mathbf{e}_1 \times \mathbf{e}_2|} \quad (\text{A.71})$$

or

$$\begin{pmatrix} n_x \\ n_y \\ n_z \end{pmatrix} = \frac{1}{|\mathbf{J}_s|} \begin{pmatrix} \frac{\partial y}{\partial \xi_s} \frac{\partial z}{\partial \eta_s} - \frac{\partial z}{\partial \xi_s} \frac{\partial y}{\partial \eta_s} \\ \frac{\partial \xi_s}{\partial x} \frac{\partial \eta_s}{\partial z} - \frac{\partial \xi_s}{\partial z} \frac{\partial \eta_s}{\partial x} \\ \frac{\partial \xi_s}{\partial x} \frac{\partial \eta_s}{\partial y} - \frac{\partial \xi_s}{\partial y} \frac{\partial \eta_s}{\partial x} \end{pmatrix} \quad (\text{A.72})$$

For the two-dimensional case,

$$ds = |\mathbf{J}_s| d\xi_s = \Delta d\xi_s \quad (\text{A.73})$$

where

$$\Delta = \left[\left(\frac{\partial x}{\partial \xi_s} \right)^2 + \left(\frac{\partial y}{\partial \xi_s} \right)^2 \right]^{1/2} \quad (\text{A.74})$$

and unit normal vector becomes

$$\begin{pmatrix} n_x \\ n_y \end{pmatrix} = \frac{1}{\Delta} \begin{pmatrix} \frac{\partial y}{\partial \xi_s} \\ -\frac{\partial x}{\partial \xi_s} \end{pmatrix} \quad (\text{A.75})$$

A.3 SOLUTION PROCEDURE

Fig. A.7 shows program flow of IWPCOMPS. As shown in Eq. A.23, the coefficient matrix, \mathbf{K} depends on the flux distribution. A particularly simple iterative method with a large radius of convergence is the successive substitution (Picard, functional iteration) method described by

$$\mathbf{K}(\mathbf{u}^n) \mathbf{p}^{n+1} = \mathbf{F} \quad (\text{A.76})$$

where the superscript indicates the iteration level. By evaluating the coefficient matrix \mathbf{K} using \mathbf{u}^n from the pressure at the previous iteration, we have linearized the problem. For the mildly nonlinear behavior typically found in heat conduction problems, the rate of converge of Eq. A.76 is generally good, despite being a first-order method. The linearized problem is solved for \mathbf{p}^{n+1} (using any matrix solution method), which is then used to evaluate the flux and the coefficient matrix for the next iteration. This procedure is continued until the root-mean-square value of the difference between the solution vectors at two consecutive iterations (normalized with respect to the current solution) is reduced to a value less than preassigned tolerance, ε :

$$\frac{(\mathbf{p}^{n+1} - \mathbf{p}^n)^T (\mathbf{p}^{n+1} - \mathbf{p}^n)}{(\mathbf{p}^{n+1})^T (\mathbf{p}^{n+1})} < \varepsilon^2 \quad (\text{A.77})$$

The value of ε are taken to be in the range of $10^{-2} \sim 10^{-4}$. During an iteration step, Eq. A.76 can be written in general form of

$$\mathbf{Ax} = \mathbf{b} \quad (\text{A.78})$$

In this study the matrix \mathbf{A} is large sparse, banded and symmetric. A solution to Eq. A.78 can be achieved by either an iterative or direct method. The solution methods used in IWPCOMPS are based on a preconditioned conjugate gradient (PCG) algorithm in default. However, the frontal method can be also chosen as an option.

A.4 VERIFICATION OF THE FEM SIMULATOR

In this section, two simple problems are presented to show the accuracy of the FEM simulator. The first example is a 2D radial flow problem. The geometry and its boundary conditions are shown in Fig. A.8. The analytical solution of this problem is obtained by integrating the Forchheimer equation in the radial coordinate systems. From Eq. 2.20,

$$-\frac{dp}{dr} = \frac{\mu}{k}u + \beta\rho u^2 \quad (\text{A.79})$$

and the fluid velocity is given by

$$u = -\frac{r_b}{r}u_b \quad (\text{A.80})$$

Substituting Eq. A.80 into Eq. A.79 gives

$$-\frac{dp}{dr} = -\frac{\mu}{k}\left(\frac{r_b}{r}u_b\right) + \beta\rho\left(\frac{r_b}{r}u_b\right)^2 \quad (\text{A.81})$$

Integrating Eq. A.81 to give

$$\begin{aligned} -\int_{p_w}^p dp &= -\frac{\mu}{k}r_b u_b \int_{r_w}^r r^{-1} dr + \beta\rho r_b^2 u_b^2 \int_{r_w}^r r^{-2} dr \\ p_w - p(r) &= -\frac{\mu}{k}r_b u_b \ln \frac{r}{r_w} - \beta\rho r_b^2 u_b^2 \left(\frac{1}{r_w} - \frac{1}{r} \right) \\ p(r) &= p_w + \frac{\mu}{k}r_b u_b \ln \frac{r}{r_w} + \beta\rho r_b^2 u_b^2 \left(\frac{1}{r_w} - \frac{1}{r} \right) \end{aligned} \quad (\text{A.82})$$

Fig. A.9 shows the finite element meshes obtained by GiD (in default mesh). The simulation results (Fig. A.10) are compared with Eq. A.82 in Fig. A.11 using linear and quadratic interpolation functions. The pressure profiles for linear and quadratic elements match very well with the analytical solution.

The second example is 3D spherical flow problem (Fig. A.12). Since the flow geometry is spherical, the flux distribution can be determined by

$$u = \left(\frac{r_b}{r} \right)^2 u_b \quad (\text{A.83})$$

Substituting Eq. A.83 into Eq. A.79 gives

$$-\frac{dp}{dr} = -\frac{\mu}{k} \left(\frac{r_b}{r} \right)^2 u_b + \beta \rho \left(\frac{r_b}{r} \right)^4 u_b^2 \quad (\text{A.84})$$

Integrating Eq. A.84 to give

$$\begin{aligned} -\int_{p_w}^p dp &= -\frac{\mu}{k} r_b^2 u_b \int_{r_w}^r r^{-2} dr + \beta \rho r_b^4 u_b^2 \int_{r_w}^r r^{-4} dr \\ p_w - p(r) &= -\frac{\mu}{k} r_b^2 u_b \left(\frac{1}{r_w} - \frac{1}{r} \right) - \frac{\beta \rho r_b^4 u_b^2}{3} \left(\frac{1}{r_w^3} - \frac{1}{r^3} \right) \\ p(r) &= p_w + \frac{\mu}{k} r_b^2 u_b \left(\frac{1}{r_w} - \frac{1}{r} \right) + \frac{\beta \rho r_b^4 u_b^2}{3} \left(\frac{1}{r_w^3} - \frac{1}{r^3} \right) \end{aligned} \quad (\text{A.85})$$

Fig. A.13 shows the mesh plot of tetrahedral elements obtained by GiD (in default mesh). The simulation results (Fig. A.14) are compared with Eq. A.85 for linear and quadratic elements. Unlike the previous problem (a radial flow problem), linear elements become inaccurate, especially for the turbulence flow case. The result shows that the higher degree of interpolation or fine elements is required to obtain more accurate solutions. On the other hand, quadratic tetrahedral elements give very accurate results even for the turbulence flow case.

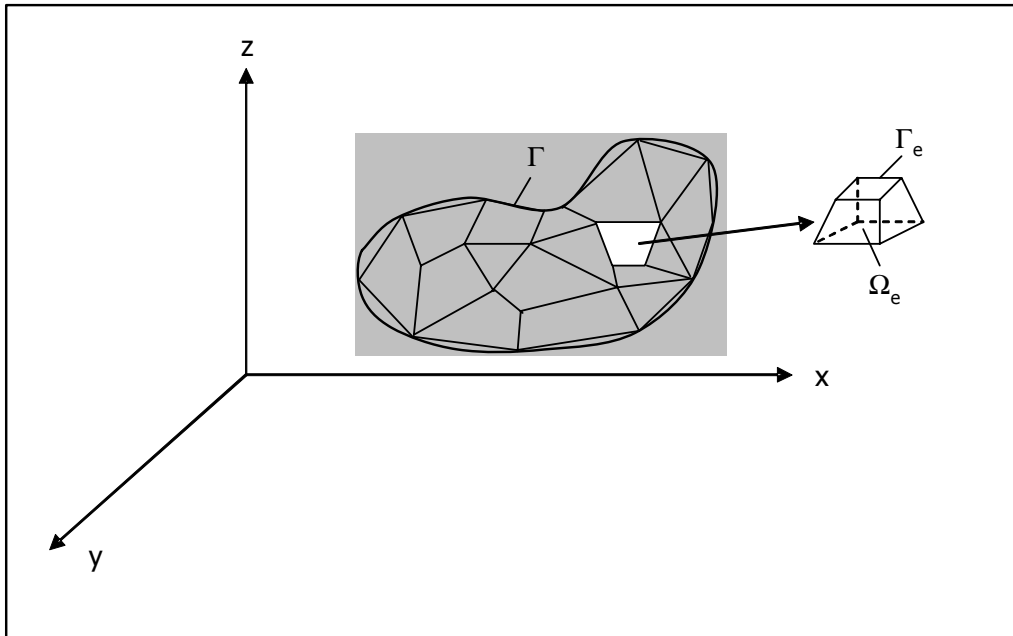


Fig. A.1 Finite element discretization of a domain.

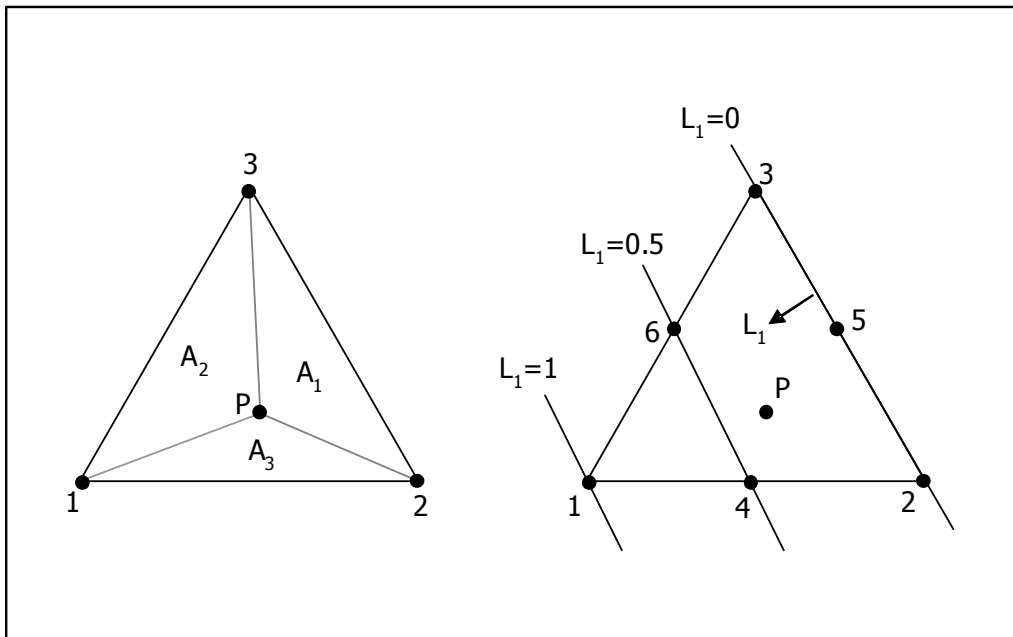


Fig. A.2 Definition of area coordinates L_i used for triangular elements.

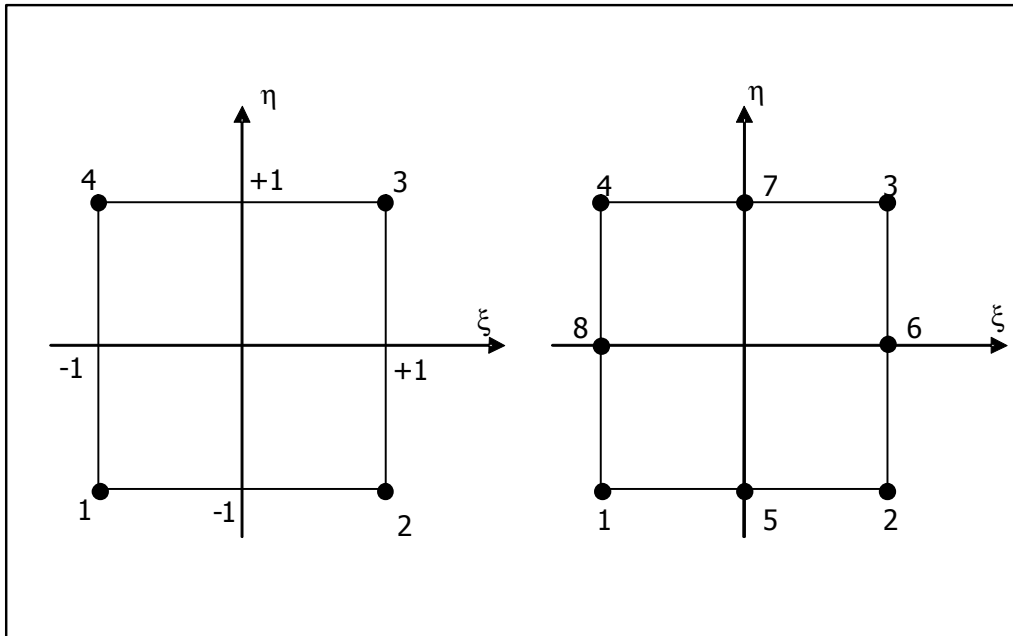


Fig. A.3 Linear and quadratic rectangular elements.

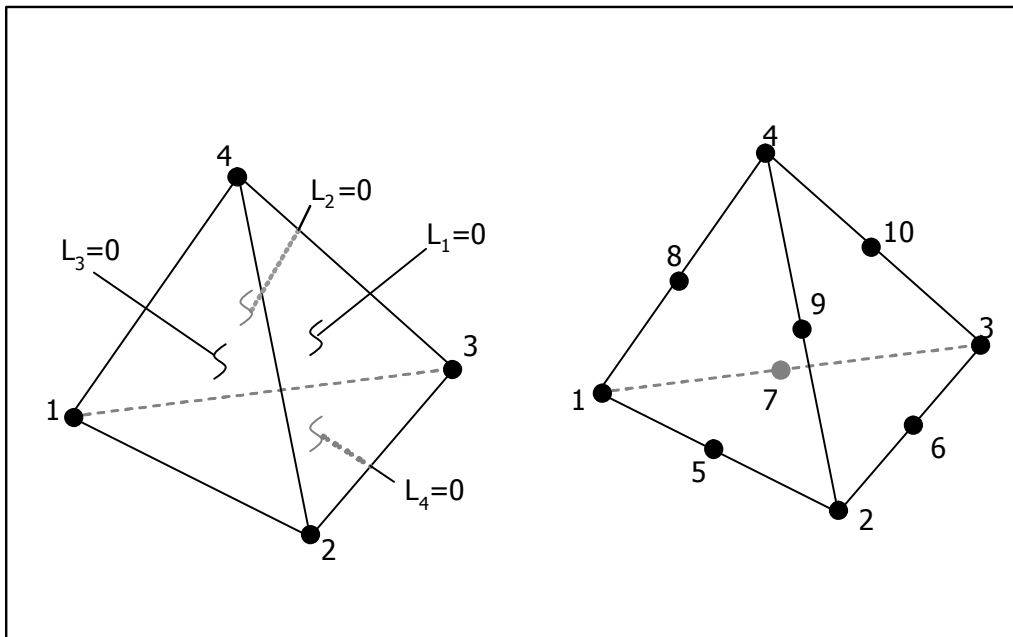


Fig. A.4 Linear and quadratic tetrahedral elements.

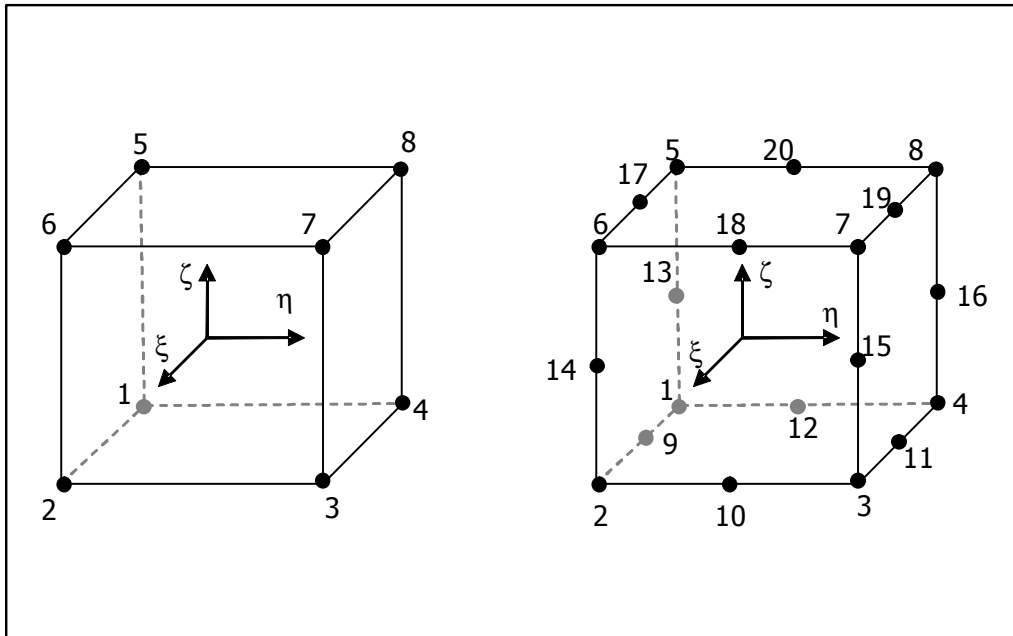


Fig. A.5 Linear and quadratic brick elements.

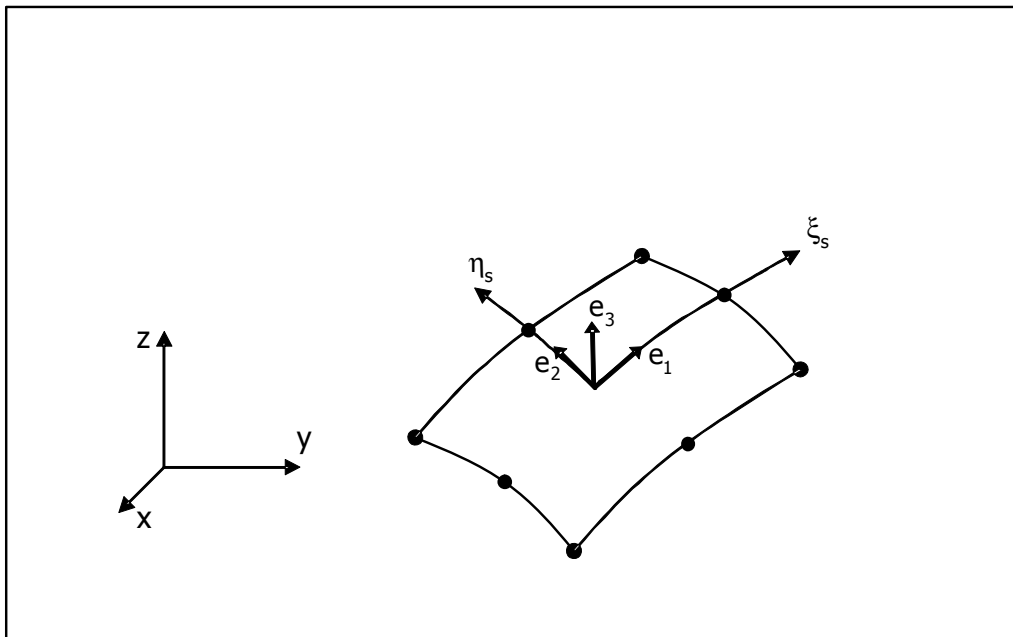


Fig. A.6 Surface fluxes computations.

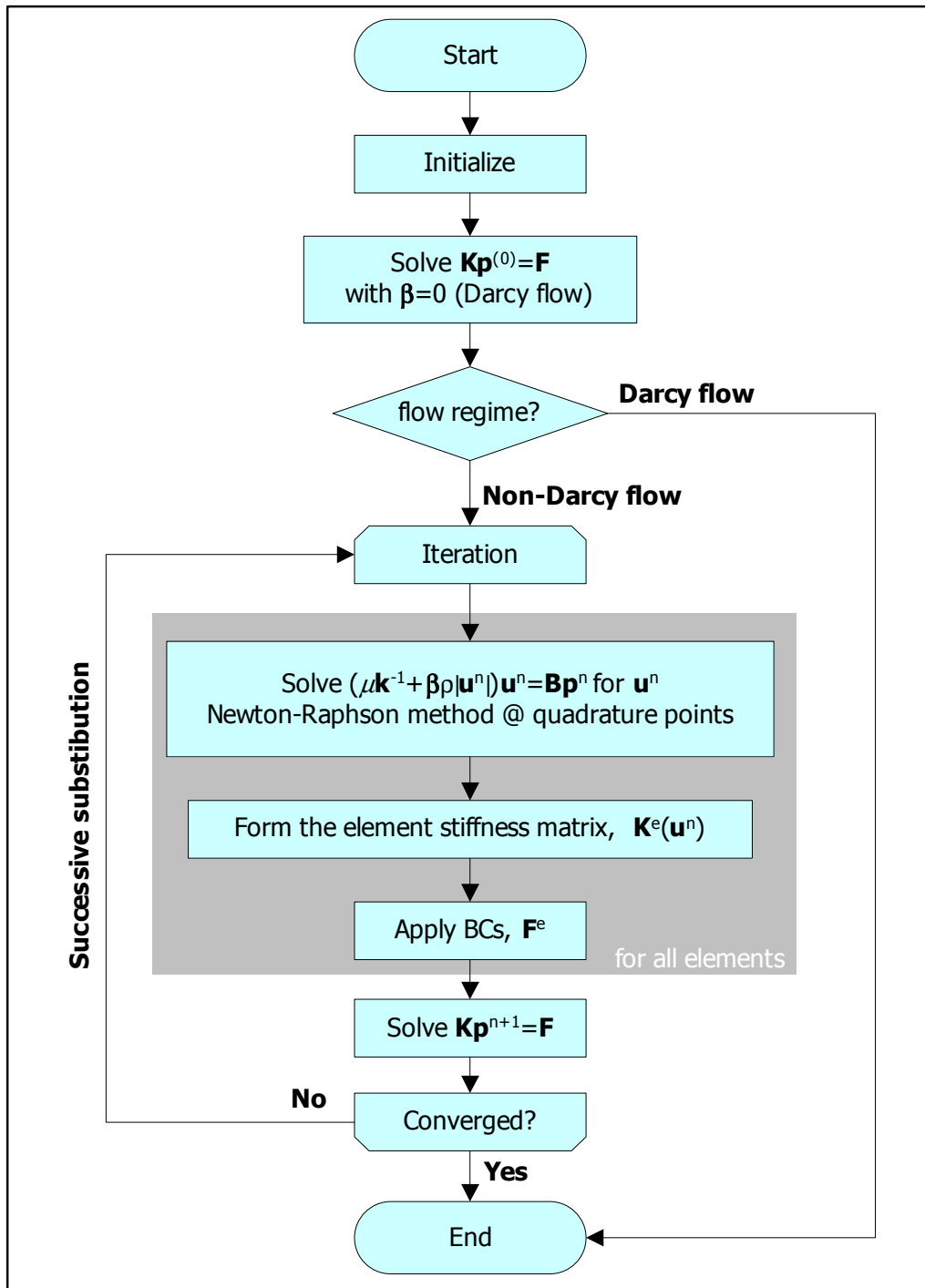


Fig. A.7 Program flow of the FEM simulation (IWPCOMPS).

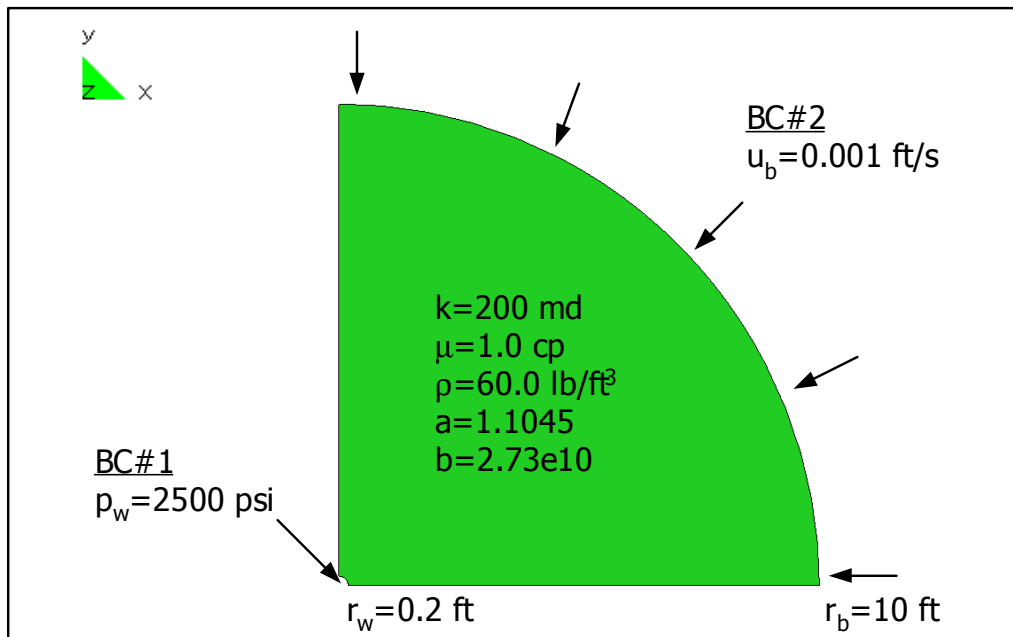


Fig. A.8 2D radial flow problem.

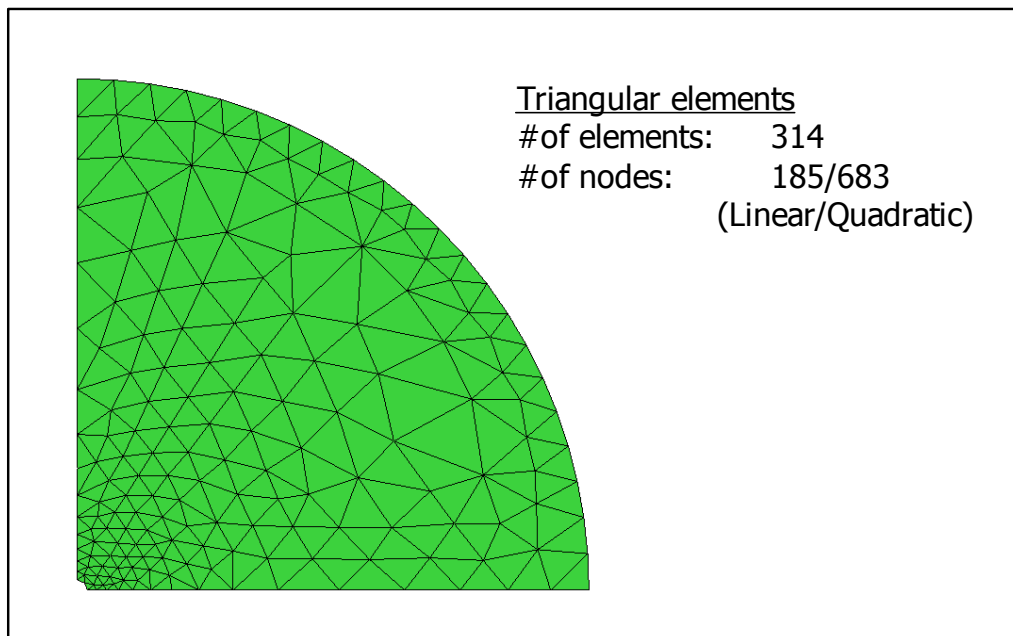


Fig. A.9 Element mesh plot – radial flow problem.

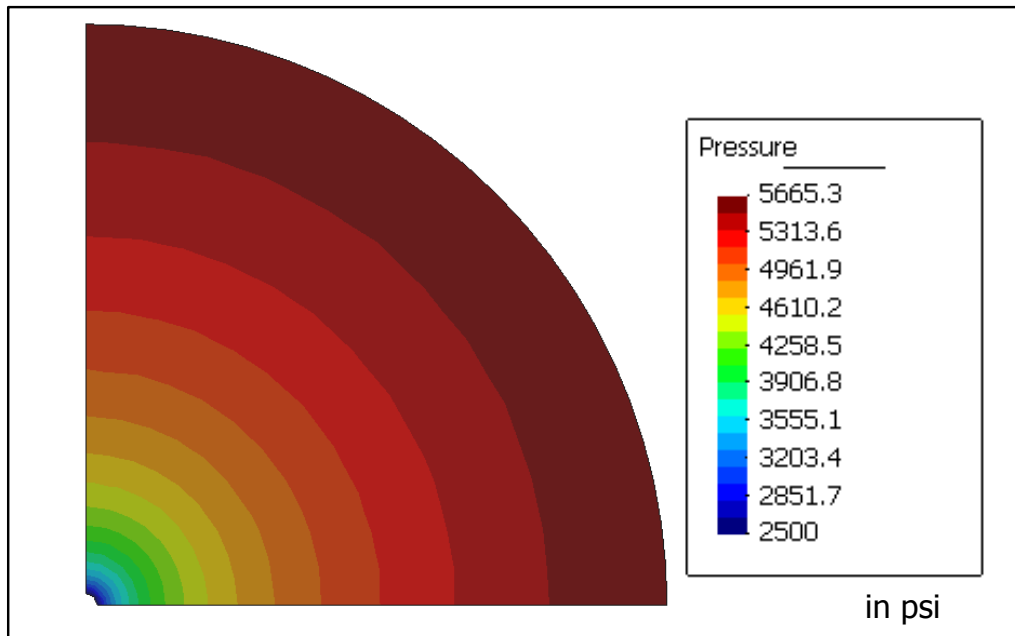


Fig. A.10 Pressure contour fill plot – radial flow problem.

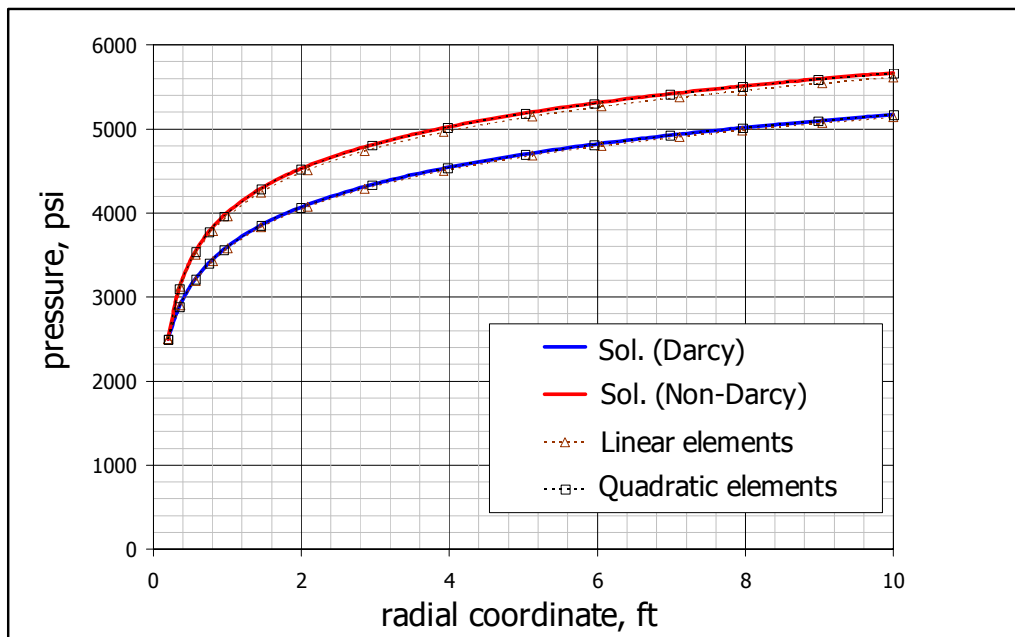


Fig. A.11 Comparison with analytical solutions, radial flow problem.

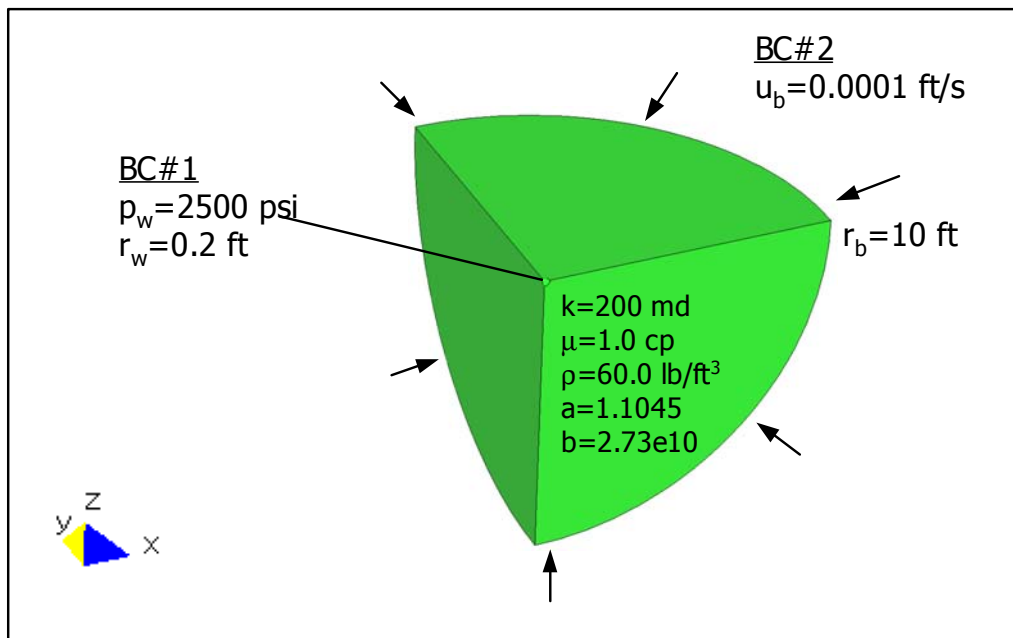


Fig. A.12 3D spherical flow problem.

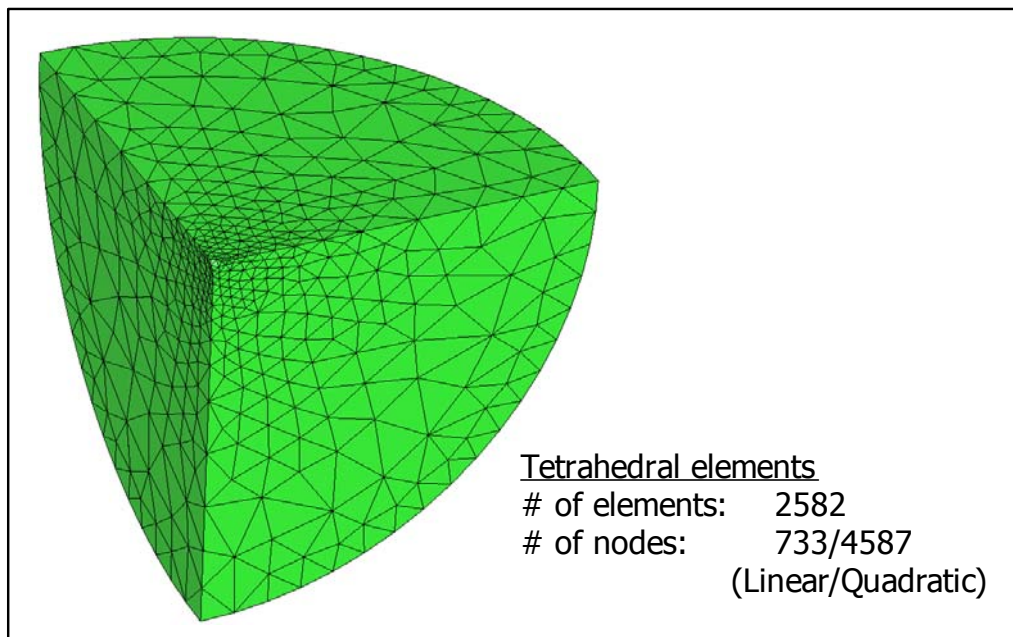


Fig. A.13 Element mesh plot – spherical flow problem.

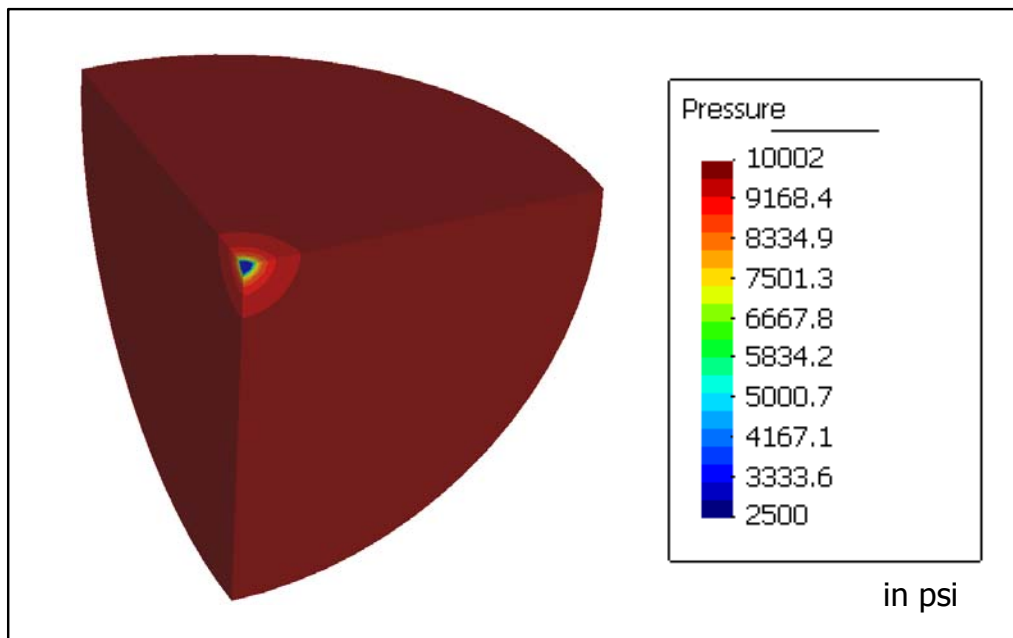


Fig. A.14 Pressure contour fill plot – spherical flow problem.

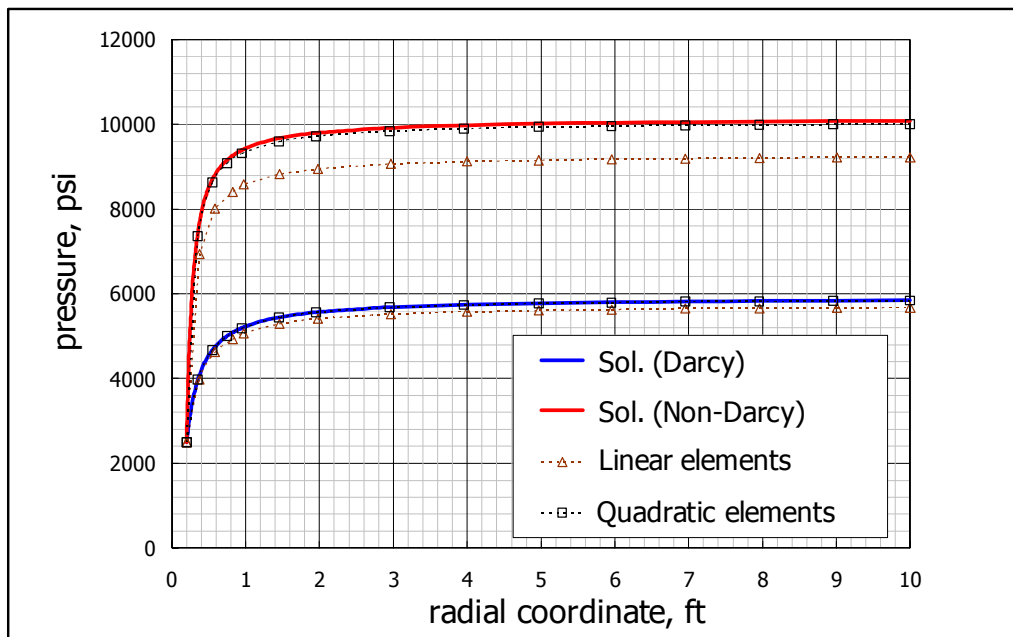


Fig. A.15 Comparison with analytical solutions, spherical flow problem.

Appendix B: GiD Files

B.1 INTERACTION OF GiD WITH IWPCOMPS

GiD is a universal, adaptive and user-friendly graphical user interface for geometrical modeling, data input and visualization of results for all types of numerical simulation programs. When GiD is to be used for a particular problem, several configuration files are necessary to be installed in the problem type folder in the main GiD executable directory (Diaz, 1999). Fig. B.1 shows the diagram of the interaction of GiD with IWPCOMPS. The GiD preprocessor discretizes a domain under study and generates a mesh of elements, each one of which is assigned a material property (i.e., permeability and porosity) and boundary conditions (i.e., pressure and/or flux). The preprocessor information in GiD (mesh, materials, and boundary conditions) enables IWCOMPS to generate results (i.e., pressure and flux distributions).

The configuration of GiD is accomplished through text formatted files. The following files are installed in IWPCOMPS:

- `irina3D.prb`: Define the general parameters
- `irina3D.mat`: Define materials and their properties
- `irina3D.cnd`: Define the boundary conditions
- `irina3D.bas`: Define the format of the interchange that mediates between GiD data and IWPCOMPS. The `.bas` file exports the geometric and physical data of the problem to `irina3D.dat` file.
- `irina3D.bat`: Initiate IWPCOMPS. This file can be executed in batches called up from GiD.

The calculating module, *irina.exe*, solves the equations of the problem and saves the results in the results files. *irina.exe* is programmed in Fortran90. The post-process reads the following files generated by *irina.exe*.

- *project_name.flavia.res*: Contain the results for all element/node.

where *project_name* is the name of the project for a particular analysis. The diagram of the file configuration is shown in Fig. B.2.

B.2 MATERIALS FILE

This file stores the physical properties of the material under study for the problem type. In this study, *x*-, *y*-, and *z*- permeabilities and porosity are considered.

Format:

NUMBER: Identifier of the material

MATERIAL: Name of the material (without spaces)

QUESTION: Property of the material (permeability/porosity).

VALUE: Value of the property

...

END MATERIAL

...

Fig. B.3 shows the materials file, *irina3D.mat* and the materials windows in the GiD interface program.

B.3 GENERAL FILE

This file contains general information for the calculating module, such as the problem title, the units system for the problem, the flow regime, the turbulence correlation used in

the study, the maximum iteration number, and tolerance for the convergence determination.

Format:

PROBLEM DATA

QUESTION: Name of the parameter. If the name is followed by the #CB# instruction, the parameter is a display-type menu. The option in the menu must then be entered between parentheses and separated by commas.

VALUE: The default value of the parameter.

...

END GENERAL DATA

Fig. B.4 shows the general file, irina3D.prb and the problem data window in the GiD interface program.

B.4 CONDITIONS FILE

The file specifies the boundary conditions of the problem. In this study, pressure and flux boundary conditions are required.

Format:

NUMBER: Identifier of the condition

CONDITION: Name of the condition

CONDTYPE: Type of entity to which the condition is to be applied. This includes the parameters; “over lines” for 2D problems and “over surfaces” for 3D problem.

CONDMESHTYPE: Type of entity of the mesh to which the condition is to be applied. In IWPCOMPS, “over face elements” is used.

QUESTION: Name of the parameter of the condition

VALUE: Default value of the parameter

...

END CONDITION

...

Fig. B.5 shows the conditions file, irina3D.cnd and the conditions window in the GiD interface program.

B.5 DATA FORMAT FILE

This file defines the format of inina3D.dat text file generated by GiD. It will store the geometric and physical data of the problem. The .dat file will be the input to the calculating module. The format of irina3D.bas file is based on commands. A text not preceded by an asterisk is reproduced exactly the same in irina3D.dat file created by GiD and to be used in irina.exe. A text preceded by an asterisk is interpreted as a command.

Commands:

***GenData()**: This must be used with an argument of integer type that specifies the number of the field to be printed. This number is the order of the field inside the general data list.

***npoin**: returns the total number of nodes of the mesh.

***ndime**: returns the dimension of the problem being considered.

***nnode**: returns the number of nodes per element.

***nelem**: returns the total number of elements of the mesh.

***nmats**: returns the number of materials.

***set elems (all)**: the command to include all the elements of the mesh during the loop.

***loop nodes**: the loop iterates on nodes.

***loop elems:** the loop iterates on elements.

***loop materials:** the loop iterates on assigned materials.

***format:** the command to define the exit format for numerical expressions. This command must be followed by the numerical format expressed in C.

***NodesNum:** returns the identifier of the present node.

***NodesCoord:** returns the coordinates of the present node.

***NodesCoord(n, real):** returns the coordinate x , y , or z in terms of the value n :

$n=1$ returns the x coordinate

$n=2$ returns the y coordinate

$n=3$ returns the z coordinate

***ElemsNum:** returns the identifier of the present element.

***ElemsNnode:** returns the number of nodes of the current element.

***ElemsConec:** returns the nodes of an element in a counterclockwise order.

***ElemsMat:** returns the number of the assigned material of the present element.

***Set var PROP1(real) = Operation(MatProp(variable, real)):** assigns the value returned by **MatProp** to the variable PROP1.

***PROP1:** returns the value of the variable PROP1.

***Matnum:** returns the identifier of the present material.

***Set Cond P1 *elems:** sets a condition over elements.

***CondNumEntities(int):** returns the number of entities that have been assigned a certain condition.

***Set var NFIX(int)=CondNumEntities(int):** assigns the value returned by the command CondNumEntities to the NFIX variable.

***NFIX:** returns the value of the NFIX variable.

***cond(1)**: returns the number 1 field of a condition previously selected with the ***set cond** command.

Fig. B.6 shows the data format file, *irina3D.bas* prepared for IWPCOMPS.

B.6 EXECUTION FILE FOR THE PROBLEM TYPE

This file connects the data file, *irina3D.dat* (internally generated by GiD) to the calculating module, *irina.exe*. When the GiD **Calculate** option is selected (Fig. B.7), it executes the .bat file for the problem type selected. When GiD executes the .bat file, it transfers three parameters in the following way:

(parameter 3)/ *irina3D.bat* (parameter 2)/ (parameter 1)

parameter 1: project name (denoted by %1)

parameter 2: project directory (denoted by %2)

parameter 3: *ProblemType* location directory (denoted by %3)

Commands:

rem: includes comments in a *.bat file or in a configuration file.

rename: renames files and directories from the original name to a new name.

echo (@echo): displays messages.

del: deletes files.

%3/irina.exe %2/%1: executes the *irina.exe* file.

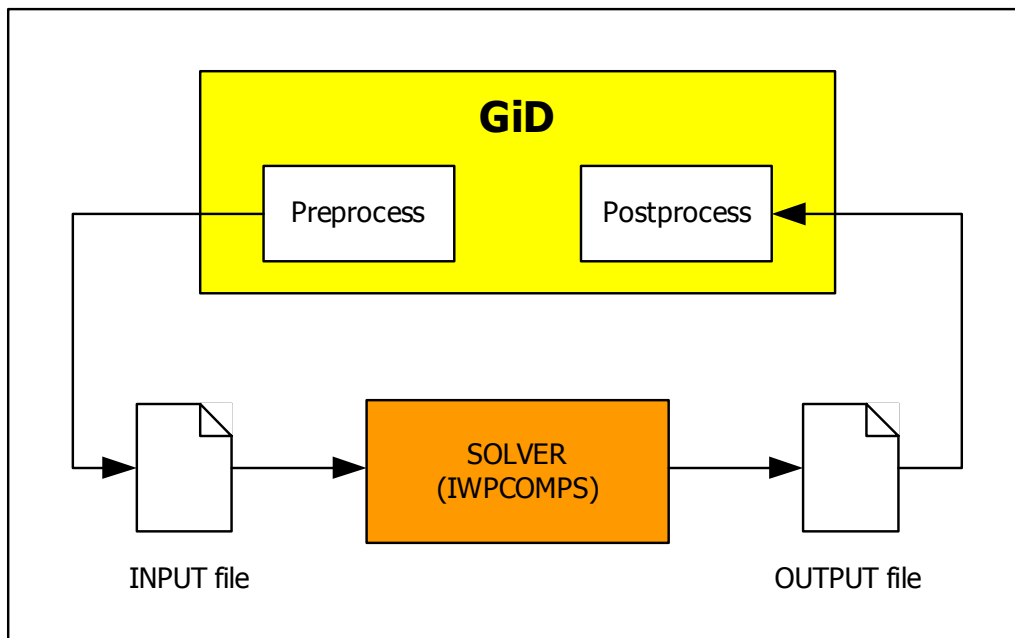


Fig. B.1 GiD customization.

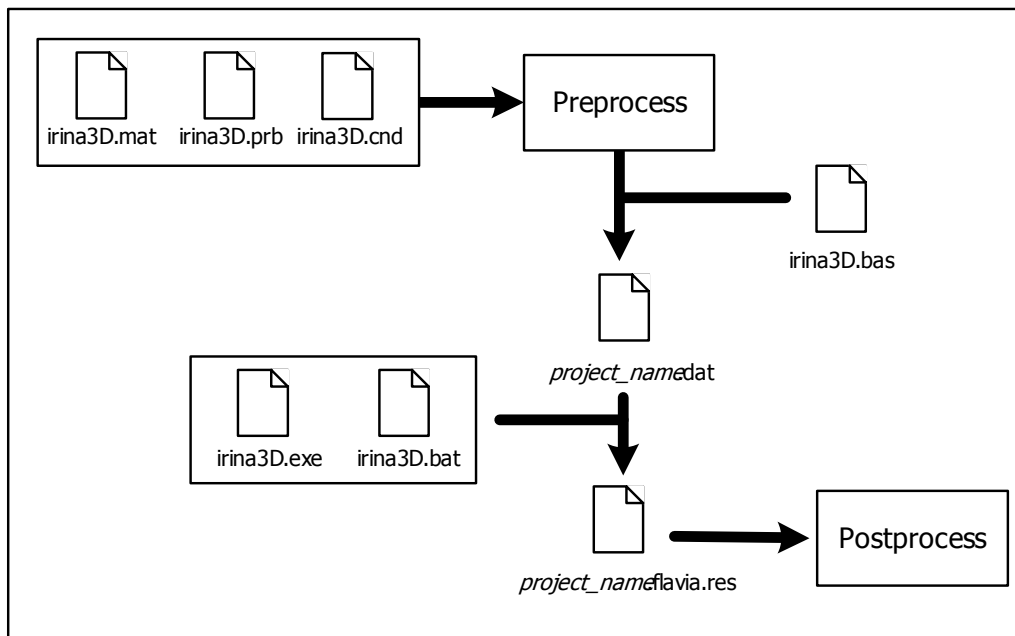


Fig. B.2 Diagram of GiD file configurations.

irina3D.mat

NUMBER: 1 MATERIAL: Formation
QUESTION: X-PERMEABILITY[md]
VALUE: 100.0
QUESTION: Y-PERMEABILITY[md]
VALUE: 100.0
QUESTION: Z-PERMEABILITY[md]
VALUE: 100.0
QUESTION: POROSITY
VALUE: 0.2
END MATERIAL
NUMBER: 2 MATERIAL: DamagedZone
QUESTION: X-PERMEABILITY[md]
VALUE: 10.0
QUESTION: Y-PERMEABILITY[md]
VALUE: 10.0
QUESTION: Z-PERMEABILITY[md]
VALUE: 10.0
QUESTION: POROSITY
VALUE: 0.2
END MATERIAL
NUMBER: 3 MATERIAL: CrushedZone
QUESTION: X-PERMEABILITY[md]
VALUE: 5.0
QUESTION: Y-PERMEABILITY[md]
VALUE: 5.0
QUESTION: Z-PERMEABILITY[md]
VALUE: 5.0
QUESTION: POROSITY
VALUE: 0.2
END MATERIAL
NUMBER: 4 MATERIAL: Gravel
QUESTION: X-PERMEABILITY[md]
VALUE: 50000.0
QUESTION: Y-PERMEABILITY[md]
VALUE: 50000.0
QUESTION: Z-PERMEABILITY[md]
VALUE: 50000.0
QUESTION: POROSITY
VALUE: 0.35
END MATERIAL

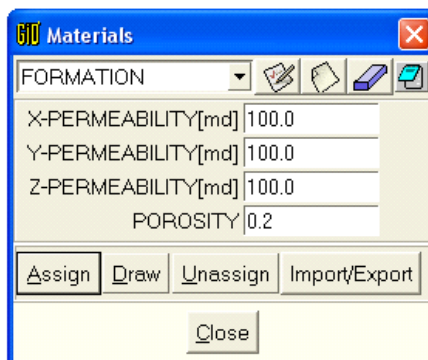
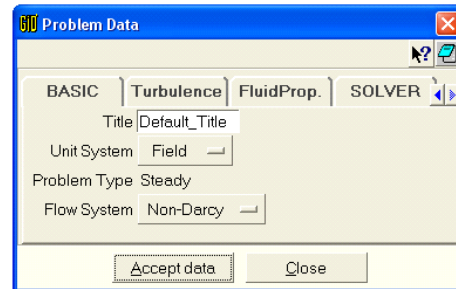


Fig. B.3 GiD materials file.

irina3D.prb

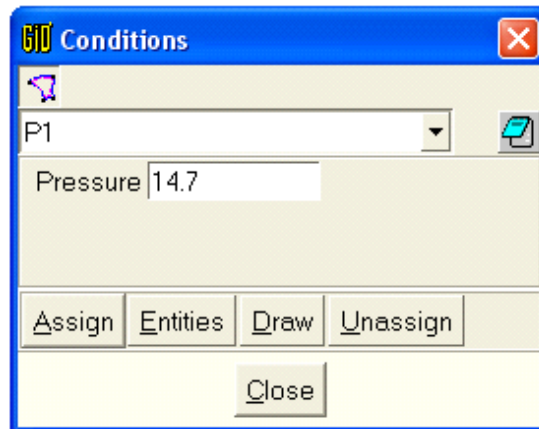
PROBLEM DATA
TITLE: BASIC
QUESTION: Title
VALUE: Default_Title
QUESTION: Unit_System#CB#(SI,Darcy,Field)
VALUE: Field
QUESTION: Problem_Type#CB#(Steady)
VALUE: Steady
QUESTION: Flow_System#CB#(Darcy,Non-Darcy)
VALUE: Non-Darcy
TITLE: TURBULENCE
QUESTION: Correlation#CB#(Tek,Geertsma-Golan,
Geertsma-Norman,Firoozabadi-Katz,Tessem-S,Tessem-L,
Suman,McLeod-C,McLeod-U,Nelson,Brown,Brown-U,
Noman,Beggs,Unneland)
VALUE: Tek
QUESTION: User_Defined#CB#(1,0)
VALUE: 0
QUESTION: a_(slope_for_k)
VALUE: 1.1045
QUESTION: b_(intercept)
VALUE: 2.73e10
QUESTION: c_(slope_for_porosity)
VALUE: 0.0
TITLE: FLUIDPROP
QUESTION: Fluid_Viscosity
VALUE: 1.0
QUESTION: Fluid_Density
VALUE: 60.0
QUESTION: Compressibility#CB#(1.e-10)
VALUE: 1.e-10
TITLE: SOLVER
QUESTION: Solver#CB#(frontal,pcg)
VALUE: frontal
HELP: frontal(DirectSolver), pcg(IterativeSolver)
QUESTION: Tol._for_NI
VALUE: 1.e-3
QUESTION: Max_Iter._for_NI
VALUE: 100
QUESTION: Tol._for_pcg
VALUE: 1.e-6
QUESTION: Max_Iter._for_PCG
VALUE: 10000
END GENERAL DATA



B.4 GiD general file.

irina3D.cnd

NUMBER: 1 CONDITION: P1
CONDTYPE: over surfaces
CONDMESHTYPE: over face elements
QUESTION: Pressure
VALUE: 14.7
END CONDITION
NUMBER: 2 CONDITION: P2
CONDTYPE: over surfaces
CONDMESHTYPE: over face elements
QUESTION: Pressure
VALUE: 100.
END CONDITION
NUMBER: 3 CONDITION: qn1
CONDTYPE: over surfaces
CONDMESHTYPE: over face elements
QUESTION: Flux(normal)
VALUE: 1.e-6
END CONDITION
NUMBER: 4 CONDITION: qn2
CONDTYPE: over surfaces
CONDMESHTYPE: over face elements
QUESTION: Flux(normal)
VALUE: 1.e-6
END CONDITION



B.5 GiD conditions file.

irina3D.bas

```
[DIMENSION CONTROL PARAMETERS - PROBLEM SIZE -]
%Problem
*GenData(1) *GenData(2) *GenData(3) *GenData(4)
*GenData(5) *GenData(6) *GenData(7) *GenData(8) *GenData(9)
*GenData(10) *GenData(11) *GenData(12)
*GenData(13) *GenData(14) *GenData(15) *GenData(16) *GenData(17)
%Dim_Params
npoin,ndime,nnode,nelem,nmats
*npoin *ndime *nnode *nelem *nmats
*if(ndime==2)
*MessageBox Error: irina3D is only for 3D problem.
*endif
%nnode_coord
Node      X      Y      Z
*set elems(all)
*loop nodes
*format "%7f%22.12e%22.12e%22.12e"
*NodesNum *NodesCoord(1,real) *NodesCoord(2,real) *NodesCoord(3,real)
*end nodes
%element_connect
Element #nodes Connectivity #Mat
*loop elems
*ElemsNum *ElemsNnode *ElemsConec *ElemsMat
*end elems
%material
Mat.      Principal Permeabilities, Porosity
*loop materials
*format "%4f%13.5e%13.5e%13.5e%13.5e"
*set var PROP1(real)=Operation(MatProp(X-Permeability,real))
*set var PROP2(real)=Operation(MatProp(Y-Permeability,real))
*set var PROP3(real)=Operation(MatProp(Z-Permeability,real))
*set var PROP4(real)=Operation(MatProp(Porosity,real))
*MatNum *PROP1 *PROP2 *PROP3 *PROP4
*end
%constraint
*Set Cond P1 *elems
*Set var NFIX(int)=CondNumEntities(int)
*NFIX
pside p-1
*loop elems *OnlyInCond
*elemsnum() *cond(1) *LocalNodes
*end
%constraint
*Set Cond P2 *elems
*Set var NFIX(int)=CondNumEntities(int)
*NFIX
pside p-2
*loop elems *OnlyInCond
*elemsnum() *cond(1) *LocalNodes
*end
%constraint
*Set Cond qn1 *elems
*Set var NFIX(int)=CondNumEntities(int)
*NFIX
fside qn-1
*loop elems *OnlyInCond
*elemsnum() *cond(1) *LocalNodes
*end
%constraint
*Set Cond qn2 *elems
*Set var NFIX(int)=CondNumEntities(int)
*NFIX
fside qn-2
*loop elems *OnlyInCond
*elemsnum() *cond(1) *LocalNodes
*end
%end
```

Fig. B.6 GiD data format file.

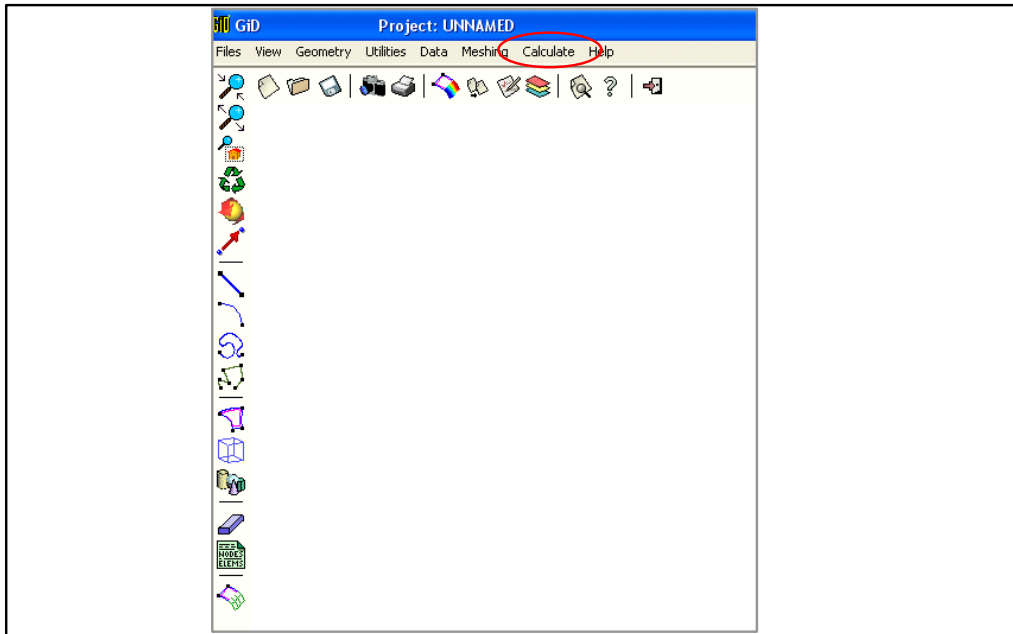


Fig. B.7 Calculate option in GiD interface.

irina3D.bas

```
@ECHO OFF
rem basename=%1
rem directory=%2
rem ProblemDirectory=%3

del %2\irina.dat
del %2\irina.err
del %2\irina.out
del %2\irina.pst
del %2\%1.flavia.res
del %2\%1.flavia.msh
del %2\irina.front.txt
del %2\irina.pcg

rename %2\%1.dat %2\irina.dat

%3\irina.exe %2\%1

rename %2\irina.flavia.res %2\%1.flavia.res
rename %2\irina.flavia.msh %2\%1.flavia.msh
```

Fig. B.8 GiD execution file.

Appendix C: Example Skin Calculations

Assume that a well described in Table C.1 has uniform formation damage which extends 6 inches into the formation in the horizontal direction ($r_{sH}=0.75$ feet all along the well). Find the rate-independent skin factor and turbulence scale factor.

a) Openhole completion

Calculate r_{DsH}

$$r_{DsH} = r_{sH} / r_w = 0.75 / 0.25 = 3 \quad (C.1)$$

Use Eq. 3.12 to get

$$\begin{aligned} s_O^0 &= (k_{Ds}^{-1} - 1) \ln \left(\frac{r_{DsH} + \sqrt{r_{DsH}^2 + I_{ani}^2 - 1}}{I_{ani} + 1} \right) \\ &= (0.1^{-1} - 1) \ln \left(\frac{3 + \sqrt{3^2 + 3^2 - 1}}{3 + 1} \right) = 5.19 \end{aligned} \quad (C.2)$$

The dimensionless turbulence factor, β_{Ds} is given by

$$\begin{aligned} \beta_{Ds} &= \beta_s / \beta = (k / k_s)^a \\ &= 0.1^{-1.1045} \approx 12.7 \end{aligned} \quad (C.3)$$

Use Eq. 3.13

$$\begin{aligned} f_{t,O} &= \beta_{Ds} + (1 - \beta_{Ds}) \left(\frac{I_{ani} + 1}{r_{DsH} + \sqrt{r_{DsH}^2 + I_{ani}^2 - 1}} \right) \\ &= 12.7 + (1 - 12.7) \left(\frac{3 + 1}{3 + \sqrt{3^2 + 3^2 - 1}} \right) \approx 6.15 \end{aligned} \quad (C.4)$$

b) Slotted liner with open area=2.55%, $w_s=0.06$ in., $l_s=2$ in., $m_s=12$, $n_s=1$ (single inline and open slots).

The number of slots per feet, n_s can be obtained by

$$n_s = \frac{A_w \cdot O_s}{w_s l_s} = \frac{(2\pi \times 0.25 \times 12 \times 12) \times 0.0255}{0.06 \times 2} \approx 48 \text{ slots/ft} \quad (C.5)$$

where A_w and O_s denote the O.D. surface area per foot of pipe (in.³/ft) and the open slot area (%) and. The slot unit length, l_u can be obtained by

$$l_u = 12 / (n_s / m_s) = 12 / (48 / 12) = 3 \text{ in.} \quad (\text{C.6})$$

The slot penetration ratio, λ is given by

$$\lambda = l_s / l_u = 2 / 3 \approx 0.667 \quad (\text{C.7})$$

The dimensionless slot length can be obtained by Eq. 4.49 in anisotropic formations

$$l_{Ds} = \frac{2l_s / r_w}{I_{ani} + 1} = \frac{2 \times 2 / (0.25 \times 12)}{3 + 1} \approx 0.333 \quad (\text{C.8})$$

From Eq. 4.2,

$$\gamma = l_{Ds} / 2\lambda = 0.333 / (2 \times 0.667) \approx 0.25 \quad (\text{C.9})$$

Use Eq. 4.1 to find

$$v = \sin(\pi / m_s) = \sin(\pi / 12) = 0.259 \quad (\text{C.10})$$

For $\gamma < v$, we can use Eq. 4.44 and 4.45

$$s_{SL,r}^0 \approx 0.171 + 0.714 - 0.230 = 0.655 \quad (\text{C.11})$$

$$f_{t,SL,r} \approx 6.074 + 5.330 + 0.794 = 12.20 \quad (\text{C.12})$$

Due to the presence of formation damage, the rate-independent skin factor and the turbulence scale factor are magnified.

$$s_{SL}^0 = s_{f0} + s_{SL,r}^0 / k_{Ds} = 5.19 + 0.655 / 0.1 = 11.74 \quad (\text{C.13})$$

$$f_{t,SL} = \beta_{Ds} f_{t,SL,r} = 12.7 \times 12.20 \approx 154.9 \quad (\text{C.14})$$

C) Perforated liner with open area = 2.67%, $r_p=0.2$ in., $m_p=8$.

The perforation shot density can be calculated by

$$n_p = \frac{A_w O_p}{\pi r_p^2} = \frac{(2\pi \times 0.25 \times 12 \times 12) \times 0.0267}{\pi (0.2)^2} \approx 48 \text{ shots/ft} \quad (\text{C.15})$$

The perforation penetration ratio can be obtained by

$$\lambda = 2r_p / l_u = \frac{2(0.2)}{12 / (48 / 8)} = 0.2 \quad (\text{C.16})$$

The dimensionless perforation radius is given by

$$r_{Dp} = r_p / r_w = 0.2 / 3 = 0.0667 \quad (C.17)$$

and using Eq. 4.50

$$\gamma = r_{Dp} / \lambda = 0.0667 / 0.2 = 0.333 \quad (C.18)$$

Using Eq. 4.1 to find

$$v = \sin(\pi / m_p) = \sin(\pi / 8) = 0.383 \quad (C.19)$$

Since $v > \gamma$, Eqs. 4.66 and 4.67 can be applied to obtain

$$s_{PL}^0 \approx 1.62 + 0.03 - 0.32 = 1.33 \quad (C.20)$$

$$f_{t,PL} \approx 79.06 + 0.163 + 0.723 = 79.9 \quad (C.21)$$

Due to the presence of formation damage, the rate-independent skin factor and the turbulence scale factor are magnified.

$$s_{PL}^0 = s_{f0} + s_{PL}^0 / k_{Ds} = 5.19 + 1.33 / 0.1 = 18.49 \quad (C.22)$$

$$f_{t,PL} = \beta_{Ds} f_{t,PL} = 12.7 \times 79.9 = 1014.73 \quad (C.23)$$

d) Cased perforated completion with $n_p = 2$ SPF, 180° phasing ($m_p = 2$), 8 inch long, $r_p = 0.25$ in., no crushed zone, perforations oriented horizontally.

Since $r_{sH} > l_p + r_w$, the perforations extend beyond the damage zone. Using Eqs. 5.67 and 5.68, the modified perforation length and wellbore radius can be obtained by

$$l_{p,mod} = l_p - (1 - k_{Ds}) l_{ps}(0^\circ) = 0.667 - (1 - 0.1) \times 0.5 = 0.217 \quad (C.24)$$

$$r_{w,mod} = r_w + (1 - k_{Ds}) l_{ps}(0^\circ) = 0.25 + (1 - 0.1) \times 0.5 = 0.7 \quad (C.25)$$

With these modification, perforation skin components can be calculated.

For s_{2D} , Eq. 5.83 gives

$$\begin{aligned} s_{2D} &= a_2 \ln \left(\frac{4r_w}{l_{p,mod}} \right) + (1 - a_2) \ln \left(\frac{1}{1 + l_{pD}} \right) + \ln \left[\frac{\sqrt{k_H / k_V} + 1}{2} \right] \\ &= 0.45 \ln \left(\frac{4 \times 0.25}{0.217} \right) + (1 - 0.45) \ln \left(\frac{1}{1 + 0.667 / 0.25} \right) + \ln \left[\frac{3 + 1}{2} \right] \\ &\approx 0.665 \end{aligned} \quad (C.26)$$

For s_{wb} , the effective dimensionless perforation length is given by Eq. 5.22 as

$$l_{pD,eff} = l_{pD} \left[\frac{1}{(k_H / k_V)} \right]^{0.625} = \frac{0.217}{0.7} \left[\frac{1}{9} \right]^{0.625} = 0.0785 \quad (C.27)$$

Use Eq. 5.20 to give

$$s_{wb} = b_2 \ln \left[\frac{c_2}{l_{pD,eff}} + \exp \left(-\frac{c_2}{l_{pD,eff}} \right) \right] = 0.45 \ln \left[\frac{0.6}{0.0785} + \exp \left(-\frac{0.6}{0.0785} \right) \right] \approx 0.915 \quad (C.28)$$

For s_{3D} , the dimensionless perforation spacing and the dimensionless perforation radius are first calculated by Eqs. 5.35 and 5.36 with the modification given by Eq. 5.85;

$$h_{De} = \frac{h_p}{l_{p,mod}} = \frac{0.5}{0.217} \approx 2.304 \quad (C.29)$$

$$r_{De} = \frac{r_p}{2h_p} \left(\sqrt{\frac{k_H}{k_V}} + 1 \right) = \frac{0.25/12}{2 \times 0.5} (3+1) = 0.0833 \quad (C.30)$$

Using Karakas & Tariq's correlation model,

$$\beta_1 = d_2 \log r_{De} + e_2 = -2.025 \log(0.0833) + 0.0943 \approx 2.280 \quad (C.31)$$

$$\beta_2 = f_2 r_{De} + g_2 = 3.0373 \times 0.0833 + 1.8115 \approx 2.065 \quad (C.32)$$

and

$$s_{3D} = 10^{\beta_1} h_{De}^{\beta_2-1} r_{De}^{\beta_2} = 10^{2.280} 2.304^{2.065-1} 0.0833^{2.065} \approx 2.736 \quad (C.33)$$

The rate-independent skin factor is given by

$$s_P^0 = s_{2D} + s_{wb} + s_{3D} = 0.665 + 0.915 + 2.736 \approx 4.32 \quad (C.34)$$

The turbulence scale factor can be obtained by Eqs. 5.49;

$$h_{De} = \frac{h_p}{l_p} = \frac{0.5}{0.667} \approx 0.75 \quad (C.35)$$

and

$$\begin{aligned} f_{t,P} &= 1 + \left[\frac{h_{De} (1 + \sqrt{k_H / k_V})}{2l_{Dp}} \right] \left(\frac{1}{r_{De}} - 2 \right) \\ &= 1 + (0.75 \times 4 / 2 / 2.668) (1 / 0.0833 - 2) \\ &\approx 6.62 \end{aligned} \quad (C.36)$$

e) Same as d), but perforations oriented vertically.

From Eq. 3.9, the mean radius of the damage zone is obtained by

$$\begin{aligned}\bar{r}_s &= 0.5r_w \left(r_{DsH} + \sqrt{r_{DsH}^2 + I_{ani}^2 - 1} \right) / \sqrt{I_{ani}} \\ &= 0.5(0.25) \left(3 + \sqrt{3^2 + 3^2 - 1} \right) / \sqrt{3} \\ &\approx 0.514\end{aligned}\tag{C.37}$$

In the equivalent isotropic system, the mean radius is also given by

$$\bar{r}_s = 0.5(r'_{sH} + r'_{sV})\tag{C.38}$$

where r'_{sH} and r'_{sV} are the horizontal and vertical damage radius in the transformed coordinates, respectively. r'_{sH} is given by

$$\begin{aligned}r'_{sH} &= r_{sH} / \sqrt{I_{ani}} \\ &= 0.75 / 3 \approx 0.433\end{aligned}\tag{C.39}$$

From Eq. C.38,

$$\begin{aligned}r'_{sV} &= 2\bar{r}_s - r'_{sH} \\ &= 2 \times 0.514 - 0.433 = 0.595\end{aligned}\tag{C.40}$$

r_{sV} is then derived by

$$\begin{aligned}r_{sV} &= r'_{sV} / \sqrt{I_{ani}} \\ &= 0.595 / \sqrt{3} \approx 0.344\end{aligned}\tag{C.41}$$

Since $r_{sV} < l_p + r_w$, the perforations extend beyond the damage zone. The modified perforation length and wellbore radius can be obtained by

$$\begin{aligned}l_{p,mod} &= l_p - (1 - k_{Ds})l_{ps}(90^\circ) \\ &= 0.667 - (1 - 0.1) \times (0.344 - 0.25) \approx 0.582\end{aligned}\tag{C.42}$$

$$\begin{aligned}r_{w,mod} &= r_w + (1 - k_{Ds})l_{ps}(90^\circ) \\ &= 0.25 + (1 - 0.1) \times (0.344 - 0.25) \approx 0.335\end{aligned}\tag{C.43}$$

For s_{2D} , Eq. 5.83 gives

$$\begin{aligned}
s_{2D} &= a_2 \ln \left(\frac{4r_w}{l_{p,\text{mod}}} \right) + (1 - a_2) \ln \left(\frac{1}{1 + l_{pD}} \right) + \ln \left[\frac{\sqrt{k_H / k_V} + 1}{2\sqrt{k_H / k_V}} \right] \\
&= 0.45 \ln \left(\frac{4 \times 0.25}{0.582} \right) + (1 - 0.45) \ln \left(\frac{1}{1 + 0.667 / 0.25} \right) + \ln \left[\frac{3 + 1}{2 \times 3} \right] \\
&\approx -0.877
\end{aligned} \tag{C.44}$$

For s_{wb} , the effective dimensionless perforation length is given by Eq. 5.22 as

$$\begin{aligned}
l_{pD,\text{eff}} &= l_{pD} \\
&= \frac{0.582}{0.335} \approx 1.737
\end{aligned} \tag{C.45}$$

Use Eq. 5.20 to give

$$\begin{aligned}
s_{wb} &= b_2 \ln \left[\frac{c_2}{l_{pD,\text{eff}}} + \exp \left(-\frac{c_2}{l_{pD,\text{eff}}} \right) \right] \\
&= 0.45 \ln \left[\frac{0.6}{1.737} + \exp \left(-\frac{0.6}{1.737} \right) \right] \\
&\approx 0.023
\end{aligned} \tag{C.46}$$

For s_{3D} , the dimensionless perforation spacing and the dimensionless perforation radius are first calculated by Eqs. 5.35 and 5.36 with the modification given by Eq. 5.85;

$$\begin{aligned}
h_{De} &= \frac{h_p}{l_{p,\text{mod}} \sqrt{k_H / k_V}} \\
&= \frac{0.5}{0.582 \times 3} \approx 0.286
\end{aligned} \tag{C.47}$$

$$\begin{aligned}
r_{De} &= \frac{r_p}{h_p} \\
&= \frac{0.25 / 12}{0.5} \approx 0.0417
\end{aligned} \tag{C.48}$$

Using Karakas & Tariq's correlation model,

$$\begin{aligned}
\beta_1 &= d_2 \log r_{De} + e_2 \\
&= -2.025 \log(0.0417) + 0.0943 \approx 2.889
\end{aligned} \tag{C.49}$$

$$\begin{aligned}
\beta_2 &= f_2 r_{De} + g_2 \\
&= 3.0373 \times 0.0417 + 1.8115 \approx 1.938
\end{aligned} \tag{C.50}$$

and

$$\begin{aligned}
s_{3D} &= 10^{\beta_1} h_{De}^{\beta_2-1} r_{De}^{\beta_2} \\
&= 10^{2.889} 0.286^{1.938-1} 0.0417^{1.938} \approx 0.507
\end{aligned} \tag{C.51}$$

The rate-independent skin factor is given by

$$\begin{aligned}
s_P^0 &= s_{2D} + s_{wb} + s_{3D} \\
&= -0.877 + 0.0203 + 0.507 \approx -0.350
\end{aligned} \tag{C.52}$$

The turbulence scale factor can be obtained by Eqs. 5.49;

$$\begin{aligned}
h_{De} &= \frac{h_p}{l_p \sqrt{k_H / k_V}} \\
&= \frac{0.5}{0.667 \times 3} \approx 0.250 \\
f_{t,P} &= 1 + \left[\frac{h_{De} (1 + \sqrt{k_H / k_V})}{2 l_{Dp} \sqrt{k_H / k_V}} \right] \left(\frac{1}{r_{De}} - 2 \right) \\
&= 1 + (0.25 \times 4 / 2 / 2.668 / 3) (1 / 0.0417 - 2) \\
&\approx 2.37
\end{aligned} \tag{C.53}$$

Table C.1 Data for the example problem.

Entry	Value	Unit
r_w	0.25	ft
k_s/k	0.1	
L	2000	ft
h	50	ft
I_{ani}	3	
k_H	10.0	md
k_V	1.11	md
ϕ	0.2	
a	1.1045	
b	2.73E+10	
c	0	

Nomenclature

<u>Symbol</u>	<u>Description</u>
A	surface area or flow area
A_D	dimensionless flow area
a	permeability exponent
a_m	correlation constant for s_{2D}
a_w	vertical semi-axis of the elliptical perforation
b	correlation constant (numerator value for β) or constant of conformal mapping
b_m	correlation constant for s_{wb}
b_w	horizontal semi-axis of the elliptical perforation
c	porosity exponent
c_m	correlation constant for s_{wb}
D	non-Darcy flow coefficient
ds	surface area
d_m	correlation constant for s_{3D}
e_m	correlation constant for s_{3D}
F_o	Forchheimer number
f_m	correlation constant for s_{3D}
f_t	turbulence scale factor
f^p	B.C. function for pressure
f^u	B.C. function for flux
g_m	correlation constant for s_{3D}
h	thickness of radial flow

h_{De}	dimensionless parameter for s_{3D}
h_p	perforation spacing
I	identity matrix
I_{ani}	index of anisotropy
J	Jacobian matrix
K	coefficient matrix
k	permeability
\bar{k}	geometric mean permeability
$\hat{\mathbf{k}}$	rate-dependent conductivity tensor
k_{cg}	permeability of gravel inside casing tunnel
k_{cz}	permeability of crushed zone
k_D	dimensionless permeability
k_g	permeability of gravel
k_s	permeability inside slot
k_{pg}	permeability of gravel filling the perforation
k_s	damage zone permeability
L	well length or production length
L_i	non-dimensional coordinates
l_{eH}	damage length in the horizontal direction
l_{eV}	damage length in the vertical direction
l_p	perforation length
$l_{p,mod}$	modified perforation length
l_{ps}	damage length covering over a perforation
l_s	slot length
l_u	slot unit length

m_s	num. of slot units around the circumference of the liner
m_p	num. of perforations around the circumference of the liner (casing)
\mathbf{n}	unit outward normal vector
n_s	num. of slots per slot unit
$n_x, n_y,$ and n_z	direction cosines of the unit normal vector
O	open area
P	arbitrary point
p	pressure
Δp	pressure drop
Q	internal source per unit volume
q	flow rate
\mathbf{R}	vector field
r_b	outer boundary radius
r_D	dimensionless radius
r_{Dc}	dimensionless perforation off-centered position
r_{De}	dimensionless parameter for s_{3D}
r_{gi}	inner screen (liner) radius
r_p	perforation radius
r_s	damage zone radius
r_{sH}	damage zone radius in the horizontal direction
r_w	wellbore radius
$r_{w,mod}$	modified wellbore radius
\bar{r}	mean radius
s	skin factor
s_{fo}	skin factor due to formation damage

s_{wb}	wellbore blockage skin factor
s_x	pseudoskin for boundary effects
s_{2D}	2D plane flow skin factor
s_{3D}	3D convergence skin factor
s^0	rate-independent skin factor
t	time
t_s	plugging depth
\mathbf{u}	flux vector
u	flux vector component
V	volume
w	weight function
w_s	slot width
w_u	slot unit width
$x, y, \text{ and } z$	original coordinates of the system
$x', y', \text{ and } z'$	transformed coordinates of the system

Greek

α	perforation orientation
α'	perforation orientation in the transformed coordinate system
α''	angle defined in Fig. 5.11.
β	turbulence factor (coefficient of inertial resistance)
β_D	dimensionless turbulence factor
β_1	empirical parameter for s_{3D}
β_2	empirical parameter for s_{3D}
Γ	boundary

γ	dimensionless parameter for the axial convergence flow
δ	Dirac-delta function or empirical constant for a cased and gravel packed well
ε	preassigned tolerance
ζ	variable of the natural coordinates
η	variable of the natural coordinates
θ	variable of conformal mapping
λ	slot (perforation) penetration ratio
μ	viscosity
ξ	flowpath coordinate or variable of the natural coordinates
ξ_d	dimensionless flowpath coordinate
ρ	density or variable of conformal mapping
v	dimensionless parameter for the slot-induced radial flow
Φ	fluid potential
ϕ	porosity
φ	approximation function of the master element (geometry)
χ	empirical parameter for s_{wb}
ψ	approximation (interpolation) function of the dependent variable
Ω	domain
Ω_h	domain approximated by finite element meshes
Ω^e	actual element
$\hat{\Omega}$	master element

Subscripts

CG	cased, perforated and gravel packed well
ct	casing tunnel
D	dimensionless
eff	effective
eq	equivalent
g	gravel
H	horizontal direction
ic	inside casing
\bullet	linear flow
O	openhole well
oc	outside casing
OG	open hole gravel packed well
P	cased and perforated well completions
PL	perforated liner
i, j	index
r	radial flow
s	skin or damage
SL	slotted liner
t	turbulence
V	vertical direction
w	wellbore
$x, y, \text{ or } z$	x-, y- or z- direction of the coordinate system

Superscripts

e	element
p	pressure
u	flux
0	rate-independent
$'$	ideal condition or virtual value

Bibliography

1. Ansah, J., Proett, A.M., and Soliman, M.Y.: "Advances in Well Completion Design: A New 3D Finite-Element Wellbore Inflow Model for Optimizing Performance of Perforated Completions" paper SPE 73760 presented at the SPE International Symposium and Exhibition on Formation Damage Control held in Lafayette, Louisiana, 20-21 February (2002).
2. Becker, E.B., Carey, G.F., and Oden, J.T.: *Finite Elements, an Introduction*, Vol. I, Prentice Hall, Englewood Cliffs, New Jersey (1981).
3. Beggs, H.D.: *Production Optimization Using Nodal Analysis*, OGCI Publications, Tulsa, 1991, 35, 47-55.
4. Behrmann, L.A.: "Underbalance Criteria for Minimum Perforation Damage," *SPEDC* (September 1996), 173-177.
5. Brown, K.E.: *The Technology of Artificial Lift Methods*, Penn Well Books, Tulsa (1984) **4**, 134-39.
6. Cooke, C.E. Jr.: "Conductivity of Fracture Proppants in Multiple Layers," *JPT* (Sept. 1973) 1101-07.
7. Cooper, J.W., Wang, X., and Mohanty, K.K.: "Non-Darcy-Flow Studies in Anisotropic Porous Media," *SPEJ* (December 1999) 334-341.
8. Diaz, N.D., and Amat, P.S.: *GiD User Manual*, CIMNE, Barcelona, 1999.
9. Dogulu, Y.S.: "Modeling of Well Productivity in Perforated Completions", paper SPE 51048 presented at the 1998 SPE Eastern Regional Meeting held in Pittsburgh, PA, 9-11 November (1998).
10. Economides, M.J., Hill, A.D., and Ehlig-Economides, C.: *Petroleum Production Systems*, Prentice Hall Inc., New Jersey (1994).
11. Firoozabadi, A. and Katz, D.L.: "An Analysis of High Velocity Gas Flow through Porous Media," *JPT* (Feb. 1979) 211-216.
12. Forchheimer, P.: "Wasserbewegung durch Boden," *Z. Vereines Deutcher Ingenieure* (1901) **45**, No. 50, 1781.

13. Frick, T.P. and Economides, M.J.: "Horizontal Well Damage Characterization and Removal," SPE Production Facilities, 15-22 (February 1993).
14. Furui, K., Zhu, D., and Hill, A.D.: "Rigorous Formation Damage Skin Factor and Reservoir Inflow Model for a Horizontal Well," SPE production & Facilities, 151-157 (August 2003).
15. Furui, K.: "Formation Damage Skin Model for a Horizontal Well," M.S. Thesis, The University of Texas at Austin, Austin, Texas, U.S.A., (2001).
16. Furui, K., Zhu, D., and Hill, A.D.: "A New Skin Factor Model for Perforated Horizontal Wells," paper SPE 77363 presented at the SPE ATCE in San Antonio, Texas, 29 September - 2 October, 2002.
17. Furui, K., Zhu, D., and Hill, A.D.: "A Comprehensive Model of Horizontal Well Completion Performance," paper 84401 presented at the SPE ATCE in Denver, Colorado, 5-8 October, 2003.
18. Gartling, D.K. and Hickox C.E.: "MARIAH – A Finite Element Computer Program for Incompressible Porous Flow Problems: Theoretical Background," SAND79-1622, Sandia National Laboratories, Albuquerque, NM, October 1982.
19. Gilman, J.R. and Jargon, J.R.: "Evaluating Horizontal vs. Vertical Well Performance," World Oil (April 1992) 67.
20. Golan, M. and Whitson, C. H.: *Well Performance*, 2nd ed., Prentice Hall, Englewood Cliffs, NJ, 1991.
21. Geertsma, J.: "Estimating the Coefficient of Inertial Resistance in Fluid Flow through Porous Media," *SPEJ*, (Oct. 1974) 415-450.
22. Harris, M. H.: "The Effect of Perforating on Well Productivity," *JPT* (April 1966) 518-28; Trans., AIME, 237.
23. Hawkins, M. F. Jr.: "A Note on the Skin Effect," *Trans. AIME*, **207**, 356-357, 1956.
24. Hong, K.C.: "Productivity of Perforated Completions in Formations With or Without Damage," *JPT* (Aug. 1975) 1027-38; *Trans.*, AIME **259**.
25. Hood, P.: "Frontal Solution Program for Unsymmetric Matrices," *International Journal for Numerical Methods in Engineering*, **10**, 379-399 (1976).

26. Irons, B.M.: "A Frontal Solution Program for Finite Element Analysis," *International Journal for Numerical Methods in Engineering*, **2**, 5-32 (1970).
27. Kaiser, T.M.V., Wilson, S., and Venning, L.A.: "Inflow Analysis and Optimization of Slotted Liners", *SPEDC*, 200-209, (December 2002).
28. Karakas, M. and Tariq, S.M.: "Semianalytical Productivity Models for Perforated Completions," *SPEPE* (February 1991), 73-82.
29. Klotz, J.A., Krueger, R.F., and Pye, D.S.: "Effect of Perforation Damage on Well Productivity," *JPT* (Nov. 1974) 1033-44; Trans., AIME, 257.
30. Kucuk, F. and Brigham, W.E.: "Transient Flow in Elliptical Systems," *SPEJ* (Dec. 1979) 19, 401; Trans., AIME, 267.
31. Locke, S.: "An Advanced Method for Predicting the Productivity Ratio of a Perforated Well," *JPT* (Dec. 1981) 2481-88.
32. McLeod, O.H. Jr. and Crawford, H.: "Gravel Packing for High-Rate Completions," paper 11008 presented at the 1982 SPE Annual Technical Conference and Exhibition, New Orleans, September 26-29.
33. McLeod, O.H. Jr.: "The Effect of Perforating Conditions on Well Performance," *JPT* (January 1983), 31-39.
34. Muskat, M.: *Flow of Homogeneous Fluids*, first edition, McGraw-Hill Book Co. Inc., New York City, 1949.
35. Nelson, C. and Wilson, B.: "Resin-Coated Sand Slurry Pack Gas Deliverabilities: Field and Laboratory Results," paper SPE 11984 presented at the 1983 SPE Annual Technical Conference and Exhibition, San Francisco, Oct. 5-8.
36. Noman, R., Shrimanker, N., and Archer, J.S.: "Estimation of the Inertial Resistance in High-Rate Gas Wells," paper SPE 14207 presented at the 1985 SPE Annual Technical Conference and Exhibition, Las Vegas, Sept. 22-25.
37. Peaceman, D.W.: "Interpretation of Well-Block Pressures in Numerical Reservoir Simulation With Nonsquare Grid Blocks and Anisotropic Permeability," *SPEJ*, 531-43 (June 1983).
38. Prats, M.: "Effect of Vertical Fractures on Reservoir Behavior- Incompressible Fluid Case," *SPEJ* (June 1961) 105-17; Trans., AIME, 222.

39. Pucknell J.K. and Clifford P. J.: "Calculation of Total Skin Factors," paper SPE 23100 presented at the 1991 Offshore Europe Conference held in Aberdeen, 3-6 September.
40. Reddy J.N. and Gartling, D.K.: *The Finite Element Method in Heat Transfer and Fluid Dynamics*, second edition, CRC Press, Boca Raton, 2001.
41. Spivey, J. P. and W. John Lee: "Estimating the Pressure-Transient Response for a Horizontal or a Hydraulically Fractured Well at an Arbitrary Orientation in an Anisotropic Reservoir," SPE Reservoir Eval. & Eng. (Oct. 1999) 462-469.
42. Suman, G.O. Jr., Ellis, R.C., and Snyder, R.E.: *Sand Control Handbook*, Second Edition, Gulf Publishing Company (1983).
43. Tang, Y.: Optimization of Horizontal Well Completion, Ph.D. dissertation, The University of Tulsa, Tulsa, Oklahoma, U.S.A., (2001).
44. Tek, M.R., Coats, K.H., and Katz D.L.: "The Effect of Turbulence on Flow of Natural Gas through Porous Reservoirs," *JPT* (Jul. 1962) 799-806, *Trans.*, AIME, 225.
45. Tessem, R.: "High-Velocity Coefficient's Dependence of Rock Properties: A Laboratory Study," MS Thesis, Norwegian University of Science and Technology, Trondheim, (Dec. 1980).
46. Unneland, T.: "An Improved Model for Predicting High-Rate Cased-Hole Gravel Pack Well," paper SPE 54759 presented the 1999 SPE European Formation Damage Conference held in The Hague, the Netherlands, 31 May- 1 June.
47. Van Everdingen, A.F. and Hurst, W. "The Application of the Laplace Transformation to Flow Problems in Reservoirs," *Trans. AIME*, **186**: 305-324, 1949.
48. Venkitaraman, A., Manrique, J.F., and Poe, B.D. Jr.: "A Comprehensive Approach to Completion Optimization," paper SPE 72386 presented at the 2001 SPE Eastern Regional Meeting held in Canton, Ohio, 17-19 October (2001).
49. Walvekar, S. and Ross, C.: "Production Enhancement Through Horizontal Gravel Pack," paper SPE 73777 presented at the SPE International Symposium and

Exhibition on Formation Damage Control held in Lafayette, Louisiana, 20-21 February 2002.

Vita

Kenji Furui was born in Tokyo, Japan on February 6, 1977, the son of Shingo Furui and Sayo Furui. After completing his work at Kenristu Chiba High School, Chiba, Japan in 1995, he entered Waseda University, Japan. He received the degree of Bachelor of Engineering from Waseda University in March, 1999. In April, He was admitted to the Graduate School at Waseda University. He had studied there for one and half years. In August 2000, he entered the Graduate School at University of Texas at Austin. He earned the degree of Master of Science in Petroleum Engineering in August 2001.

Permanent Address: 3-6-7 Isobe Mihama-Ku,
Chiba, Chiba,
261-0012, Japan

This dissertation was typed by the author.